University of Alberta

Library Release Form

Name of Author: Mert Ozdemirtas

Title of Thesis: Numerical and Experimental Investigations of Borehole Ballooning in Smooth and Rough Fractures

Degree: Master of Science

Year this Degree Granted: 2008

_____

Signature

University of Alberta

Numerical and Experimental Investigations of Borehole Ballooning in Smooth and Rough Fractures

By
Mert Ozdemirtas

A thesis submitted to the Faculty of Graduate Studies and Research
in partial fulfillment of the requirements for the degree of

Master of Science
in
Petroleum Engineering

Department of Civil and Environmental Engineering

Edmonton, Alberta
Spring 2009

University of Alberta

Faculty of Graduate Studies and Research

The undersigned certify that they have read, and recommend to the Faculty of Graduate Studies and Research for acceptance, a thesis entitled **Numerical and Experimental Investigations of Borehole Ballooning in Smooth and Rough Fractures** submitted by **Mert Ozdemirtas** in partial fulfillment of the requirements for the degree of **Master of Science**.

Dr. Ergun Kuru

Dr. Tayfun Babadagli

Dr. Hooman Askari-Nasab

Dr. Ahmed Bouferguene

This work is dedicated to drilling crews working somewhere in the world right now and their families.

ABSTRACT

A two dimensional transient mathematical model of borehole ballooning process was developed and solved numerically. Factors controlling the magnitude of borehole ballooning were analyzed by using the numerical model solution. The model considers the effects of both Newtonian and Non-Newtonian fluid rheology on the fracture volume change due to the transient wellbore pressure fluctuations inherent in typical drilling operations. Effects of fracture roughness (characterized by the fractal dimension of the fracture surface) and deformation approximations were also investigated. The conditions where the roughness significantly influences the magnitude of the ballooning process were identified.

Experiments were performed to study the drilling fluid loss and gain events in artificially fractured rock samples. Smooth and rough fractures were used to analyze the effect of fracture surface roughness on the flow of drilling fluid in and out of the fracture. Effect of fluid rheology has also been investigated by using Newtonian and Non-Newtonian type drilling fluids.

ACKNOWLEDGEMENTS

I want to express my sincere appreciation to my supervising professors, Dr. Ergun Kuru and Dr. Tayfun Babadagli. I thank them for their valuable advice, guidance, and encouragement throughout the course of this study.

To my most wonderful parents, for supporting me in every step of this way, I will be forever grateful for your love and guidance.

I would like to give my thanks to fellow students, Vahap Can Er and Dmitry Bogatkov for always being there to lend a helping hand when called upon. I thank all the members of EOGRRC research group of Dr. Babadagli for their review and helpful suggestions. Thanks are also sincerely expressed to Nathan Buzik for his valuable assistance in the experimental part of this thesis.

Sincere gratitude is extended to the Natural Sciences Engineering Research Council of Canada for their financial support to this research work.

Finally, I would like to extend my deepest thank to my loving fiancée, Ceren Saygilar for her patience and unconditional support during my studies.

TABLE OF CONTENTS

LIST OF TABLES

LIST OF FIGURES

LIST OF NOMENCLATURE

$B_H(x)$ =stationary stochastic process

d =fracture depth [m]

D =fractal dimension

g =acceleration of gravity [m^2/s]

H =Hurst exponent

K_N =fracture stiffness [Pa/m]

L_X =fracture length in x direction [m]

L_Y =fracture length in y direction [m]

p =pressure [Pa]

q =flow rate [m^3/s]

t =time [s]

t_s =duration of pressure variation [s]

w =fracture aperture [m]

w_0 =initial fracture aperture [m]

x =one of Cartesian coordinates [m]

y =one of Cartesian coordinates [m]

α =fracture inclination [radian]

β =fracture's normal compressibility [Pa^{-1}]

μ =dynamic fluid viscosity [Pa s]

ρ_r =rock density [kg/m^3]

σ^2 =variance

σ_n =normal stress [Pa]

σ_h =horizontal stress [Pa]

σ_v =vertical stress [Pa]

CHAPTER 1 :INTRODUCTION

1.1 OVERVIEW

Many conventional drilling operations have been carried out through naturally fractured formations where preventing and controlling mud losses and gains becomes a serious challenge. Identification and treatment of drilling fluid losses and gains is important due to the high cost of the drilling operations. The oil industry spends a lot of money every year to avoid lost circulation incidents and their detrimental consequences. Several practical solutions have been recommended to avoid drilling fluid losses and gains. However, regardless of the type of treatment, significant rig time can be lost and these solutions can make the control of other drilling parameters required for a precise well design even more complicated.

Borehole ballooning is recognized as a combined mud loss and mud gain phenomenon. It refers to the small, partial and continuous mud losses and significant rapid mud gains due to annular pressure fluctuations resulting from mud circulation and non-circulation. The term ballooning originally is used to describe wellbore expansion due to additional pressure losses during circulation and contraction when mud circulation stops (Ward and Clark, 1998). This explanation describes the monitored mud losses and gains and corresponds to blowing up and deflating a balloon. Some operators entitle this phenomenon borehole breathing i.e., the well inhales and exhales in response to the wellbore hydraulics.

Maintaining wellbore stability is an important task during drilling through fractured zones because of safety and economic reasons. Wellbore stability problems associated with drilling in these zones are linked with the nature of pre-existing (natural) and drilling induced fractures. The fundamental mechanism behind the borehole ballooning is the opening and closing of these in-situ and/or induced fractures, when the bottomhole

pressure exceeds the fracture propagation pressure. If the bottomhole pressure exceeds fracture initiation pressure during circulation, drilling fluid starts to escape into the fractured formation and more mud is required to maintain the hydrostatic head. The losses happen due to mainly the flow into fractures within a limited fractured network with little leak off into the matrix. As soon as the dynamic wellbore conditions disappear and the bottomhole pressure falls below the Fracture Initiation Pressure (FIP) during a pump-off period (connection or flow check operation), sizeable amount of mud is gained back into the wellbore. The return of the drilling fluid is more noticeable since it occurs more rapidly during a period when no flow is expected. Once the pumps are started, the annular pressure is expected to reach to the level where it was before the pumps are off. However, it might take a while to reach the former bottomhole circulating pressure level, as the fracture network is being recharged.

This research presents a numerical and experimental study on the effects of operational parameters, formation lithology, fracture surface roughness and drilling fluid rheology on borehole ballooning and its magnitude.

1.2 STATEMENT OF THE PROBLEM

Mud losses/gains have been a major problem in the drilling industry and the detection of this problem is still a crucial issue because of the cost of the nonproductive time. During ballooning, minor but continuous losses occur while circulating and fluid lost to the isolated fracture network is regained when the pumps are off. During the pumps off period, any mud return of this magnitude can be misdiagnosed as a kick caused by an influx of the formation fluids (gas, liquid hydrocarbon or water). This misjudgment and its likely treatments can lead to costly well control procedures such as increasing the mud weight. However, in case of a ballooning incident, immediate increase of the mud weight is often enough to propagate the existing fractures, which might lead to a total loss, a situation that is much more difficult to manage. On the other hand, if the mud flow is due to mud return and related to borehole ballooning, well control is not the primary issue.

Although the reasons of this phenomenon are known, the industry still has some problems with detecting and combating it. Failure to prevent borehole ballooning can greatly increase the drilling time and the already high cost of drilling, since this drilling problem recursively occurs in the lack of a treatment. Generally speaking, the drilling industry handles borehole ballooning much as it did 20 years ago. Much effort is needed to better understand the mechanics behind borehole ballooning. Factors controlling this phenomenon must be clarified to correctly interpret its symptoms observed during drilling and to avoid mixing ballooning with other formation flow incidents, which might lead to unwarranted well control procedures.

In concordance with this situation, the effect of operational parameters (borehole pressure, drilling fluid rheology) and formation's geologic properties (well location, fracture length, rate of change of fracture aperture, fracture surface roughness) on the severity of borehole ballooning should be investigated in detail. Lavrov and Tronvoll (2005) modeled borehole ballooning caused by opening and closing of natural fractures. They assumed that the fractures have smooth surfaces. This is a reasonable assumption as long as the fracture aperture is significantly larger than the dimensions of the roughness on the fracture surfaces. However, majority of original and pressure induced fractures encountered during drilling operations are not big enough in order for the smooth surface assumption to be valid. In these cases, the roughness effects should be considered and incorporated into numerical borehole ballooning models in order to make a more realistic prediction of this phenomenon.

To the author's best knowledge, there is no published experimental study about this phenomenon yet. Therefore, we investigated the question whether or not the numerical results obtained could be verified experimentally. It was both fracture roughness and the fracture mechanics play a significant role on the flow in a single fracture. Next, the effect of fluid type on the magnitude of borehole ballooning was investigated by using Newtonian and non-Newtonian fluids.

The results of this study may help the industry to better understand the nature of the borehole ballooning problem and thereby improve the well control procedures while drilling in naturally-fractured reservoirs.

1.3 OBJECTIVES AND SCOPE OF THE RESEARCH

The first objective of this study is to develop a two dimensional transient model of borehole ballooning or breathing. The numerical model considers the effects of formation pressure, borehole pressure, fracture size, fluid rheology and fracture roughness on the fracture volume change as a function of transient wellbore pressure fluctuations inherent in typical drilling operations.

The second objective of this research is to conduct laboratory scale experiments to study the drilling fluid loss and gain events in artificially fractured rock samples. Effects of rock surface roughness, fluid rheology, borehole pressure and fracture pressure on the magnitude of borehole ballooning (i.e., volume of fluid loss/gain) are investigated.

The final objective is to compare the experimental observations with the numerical model results.

To achieve these research objectives the following tasks have been accomplished:

(1) Literature review and discussion of the past research.
(2) Develop a 2-D transient model of ballooning phenomenon in cartesian coordinates.
(3) Generate 2-D surface roughness data applicable to the model and incorporate roughness into the model.
(4) Solve the numerical model for several cases and provide numerical solutions of mud loss/gain flow rates between the fracture and the borehole.

(5) Design and build a laboratory setup to investigate borehole ballooning phenomenon experimentally.
(6) Perform laboratory experiments to investigate the effects of fracture surface roughness, fluid rheology, borehole pressure and fracture pressure on the magnitude of borehole ballooning.
(7) Compare the numerical model results with the experimental results.

1.4 METHODOLOGY OF THE RESEARCH

In this study, lubrication theory was used to determine the loss/gain flow rate of the drilling fluid as a function of time and analyze the severity of borehole ballooning. The lubrication theory was originally developed from Navier-Stokes equations (NS) by Osborne Reynolds in 1886. Reynolds used the NS equations together with the continuity equation and applied simplifications consistent with hydrodynamic lubrication theory to derive the most commonly encountered form of the Reynolds Equation. In this study Reynolds equation was used to determine the pressure distribution within the fracture. The simplifications mentioned above involve certain geometric and kinematic conditions which are described in detail by Pinkus (1961).

The Reynolds equation was used to build a two dimensional transient model of ballooning phenomenon in Cartesian coordinates. An explicit finite difference method is used in order to solve this equation and achieve the final form of the equation governing the fluid flow in a single horizontal fracture. The pressure profile within the fracture was calculated and then fluid loss and gain rate between the borehole and the fractured formation was analyzed.

Limestone, sandstone and granite core samples were used in the experiments. Effects of rock lithology, type of fracture surface roughness, drilling fluid rheology and initial pressure values within the fracture and borehole on the magnitude of borehole ballooning phenomenon were investigated.

1.5 STRUCTURE OF THE THESIS

Chapter 1 provides a general outline of the borehole ballooning problem. It includes the overview of the research study, the statement of the problem, the objectives and the scope of the research and the methodology of the research.

Chapter 2 gives a comprehensive literature review of the borehole ballooning facts and related research areas, which include numerical and experimental analysis of fluid flow in a single fracture. It reviews the fracture surface roughness measurement methods and numerical roughness generation techniques as well.

Chapter 3 presents the development of the numerical borehole ballooning model in a single horizontal fracture. It describes the governing equations, model geometry, boundary conditions and the numerical solution of the model. This part finishes with an illustrative borehole ballooning scenario.

Chapter 4 presents the results of the numerical analysis of borehole ballooning phenomenon. Effects of various operational parameters on the fluid flow dynamics during a ballooning event in a single horizontal fracture with smooth and rough surfaces are presented.

Chapter 5 explains the experimental program including the details of materials used for the experiments, experimental setup and procedure.

Chapter 6 demonstrates the effects of several experimental parameters including the drilling fluid rheology on the magnitude of borehole ballooning and presents the discussion of the experimental results and observations.

Chapter 7 contains the conclusions of this research.

CHAPTER 2 :LITERATURE REVIEW

2.1 FACTS ABOUT BOREHOLE BALLOONING

The borehole ballooning or breathing results from drilling with a borehole pressure close to the fracture initiation pressure. Partial, small, but continuous mud losses can accumulate to a significant volume after a long drilling period if not detected while drilling ahead. Losses contained in the limited fracture network flow back into the wellbore, when the annular pressure goes down due to a stoppage of the fluid circulation at any time during a drilling operation.

2.1.1 When and where does Ballooning occur?

Limited number of studies have been published about the mechanisms behind this phenomenon. According to Gill (1989), elastic deformation of the borehole wall due to the bottomhole pressure can explain this incident. Ram Babu (1998) proposed that expansion and contraction of the drilling fluid due to the temperature variations in the wellbore can be diagnosed as borehole ballooning. Lavrov and Tronvoll (2005) suggested that opening/closing of natural fractures intersected during drilling with a bottomhole pressure higher than fracture initiation pressure is the main mechanism behind ballooning.

As stated by Tare et al. (2001), borehole ballooning can be attributed to local geologic settings, inherent natural fractures, well trajectory, operational drilling parameters including equivalent mud weight and mud rheology. It is commonly observed during: (1) drilling through fractured zones within a limited fracture network with partial leak off into the surrounding non-permeable formation (i.e., primarily shale), (2) deepwater drilling operations with narrow operating window between pore pressure and fracture gradient and (3) drilling extended reach wells with high inclination angles (Tare et al., 2001).

2.1.2 Why is Ballooning a concern?

One of the most severe consequences of wellbore breathing is the misinterpretation of the observed rapid sizeable mud flow into the wellbore as a kick (Ward and Clark, 1998). The first question asked when dealing with a flow into the wellbore is “How can the operator know if it is a formation fluid influx or regained mud from the formation lost while drilling ahead?” This issue increases the need for research about the mechanics of this phenomenon, since mixing this phenomenon with well kicks might lead to unwarranted well control procedures like increasing the mud weight. However, if the influx is just the returning mud, increasing the mud weight as a treatment can extend the existing fractures and make the situation even more difficult to control.

2.1.3 How can Ballooning be practically avoided?

Several products and techniques have been employed in attempts to prevent borehole ballooning while drilling natural and induced fractures. Even though these treatments sometimes help to avoid this phenomenon, more often than not they are temporary solutions as losses/gains reoccur as drilling proceeds.

The major problem with borehole ballooning is to identify this problem correctly and not to mix it with any other loss circulation events and drilling troubles. If borehole ballooning is correctly identified, the most practical steps followed on the oil field can be summarized as (Power et al., 2003):

(1) To reduce the mud weight,
(2) To decrease the equivalent circulating density (ECD),
(3) To lower the flow rates,
(4) To reduce the rate of penetration (ROP),
(5) To provide a thinner drilling fluid

Since loss and gain problems result from the initiation of fractures, mitigation steps will be the same as those for lost circulation issues in general.

Debate on the type of the material, amount and when to add it to the active system to prevent ballooning is on-going and unending (Tare et al, 2001). However, a recent study has reported that synthetic graphite in conjunction with properly sized calcium carbonate can bridge fractures and supply some healing characteristics to fractures by increasing their initiation pressure when drilling with synthetic based muds (Cameron, 2001). Observed field data has also confirmed that the re-opening pressure increases significantly if this combination of lost circulation material is spotted in the fractures.

Current developments in measurement while drilling technology have considerably improved the industry's ability to detect fractured zones that may be linked with borehole ballooning. These new generation down hole assembly drilling tools bring also some benefits for improving well stability and navigating narrow mud weight windows and generally avoiding high borehole pressure induced loss circulation incidents. Downhole measurements combined with surface observations allow the operators to make conclusive determination of the presence of the borehole ballooning (Power et al., 2003).

2.2 NUMERICAL ANALYSIS OF DRILLING FLUID LOSS/GAIN IN A SINGLE FRACTURE

The industry's need to understand the mechanisms behind mud losses/gains in fractures has led to the publication of several studies modeling these phenomena with different approaches. San Fillippo et al. (1997) provided an approximate analytical relationship between time and volume of fluid escaped to the fractures by applying the diffusivity equation with a constant pressure difference boundary condition and by interpolating a tabulated solution of the problem. This relationship was used to understand the mud loss data and to estimate the fracture hydraulic aperture. They considered Newtonian mud rheology and a non-deformable fracture of constant aperture having impermeable walls.

Lietard et al. (2004) developed a model of radial drilling fluid flow into a non-deformable fracture of constant aperture and infinite length. Their model was based on Darcy's law and took non-Newtonian incompressible fluid rheology into account. They did not consider the fracture wall permeability in their model. They assumed that the difference between circulating botttomhole pressure and the static reservoir pressure was not changing in time. They derived mud propagation versus time curves for different hydraulic apertures based on the numerical solutions of governing equations.

Verga et al. (2000) developed their model using the diffusivity equation and made constant aperture approximation. Their model considered non Newtonian fluid rheology. They emphasized the importance of introducing a realistic rheology on their mud loss results. The fracture aperture values calculated with their model were in good agreement with those achieved by electric imaging logs.

Lavrov and Tronvoll (2003) developed a one dimensional linear model of mud loss into a single fracture and studied effects of different parameters on mud loss dynamics. Their model considered Newtonian fluid rheology and analyzed only mud loss events. As a next step, they modeled the mud loss events in radial coordinates (2004). Non-Newtonian fluid assumption was considered in this model. The horizontal circular fracture was assumed to be obeying the linear deformation law. Lavrov and Tronvoll (2005) also looked into the mechanics of borehole ballooning (combined mud loss/gain event). They modified their earlier model by introducing radial coordinates and incorporating the exponential deformation law. In a recent study, Lavrov and Tronvoll (2006) modeled the mud loss events in cartesian coordinates and discussed effects of fracture dimensions on the magnitude of mud loss events.

Lavrov and Tronvoll (2003, 2004, 2005 and 2006) incorporated fracture opening/closing into their models using a simplified linear or empirical exponential law. However, they did not compare the magnitude of mud loss/gain considering these two deformation laws in the same study. To the author's best knowledge, Lavrov and Tronvoll (2005) were the only researches analyzing mechanics of borehole ballooning. Lavrov and Tronvoll's

research made significant contributions to the literature and has also inspired the research presented in this thesis. Table 2-1 shows the comparison of Lavrov and Tronvoll's studies and pointing out the parameters they considered individually in each study.

Table 2-1: Comparison of Lavrov and Tronvoll's studies and the parameters they considered in each study

	Mud Loss into a Single Fracture During Drilling, *Lavrov A. and Tronvoll J., 2003*	**Modeling Mud Loss in Fractured Formations, *Lavrov A. and Tronvoll J., 2004***	**Mechanics of Borehole Ballooning in Naturally Fractured Reservoirs, *Lavrov A. and Tronvoll J., 2005***	**Numerical Analysis of Radial Flow in a Natural Fracture, *Lavrov A. and Tronvoll J., 2006***
Dimension	1D	Radial	Radial	Radial
Fracture Deformation	Linear	Linear	Linear	Exponential
Leak off Rule	•			
Model of Mud Rheology	Newtonian	Power Law	Power Law	Newtonian
Effect of Mud Rheology		•	•	
Effect of Mud Viscosity	•	•		
Effect of Mud Weight	•	•		
Effect of Formation Pressure	•	•		
Effect of Fracture Aperture	•	•		
Effect of Fracture Length	•	•		
Effect of Fracture Diameter		•	•	
Effect of Fracture Radius		•		
Effect of Wall Permeability	•			
Effect of in plane aspect ratio				•
Effect of Sink Location				•
Effect of Compressibility				•

2.3 EXPERIMENTAL ANALYSIS OF FLUID FLOW IN A SINGLE FRACTURE

Most of the literature about the fundamentals of fluid flow in a single fracture theory was found in the areas of geophysics and water resources. The direct relationship between fracture aperture and fluid flow has been established from theoretical and experimental investigations of fluid flow through a single fracture. Laminar flow of a viscous incompressible fluid in a fracture has been studied by many researchers starting with Lomize (1951). He found that laminar flow between two glass plates depends on the cube of the aperture between the plates.

Iwai (1976) performed a comprehensive study of fluid flow in a single fracture and investigated the validity of cubic law. He considered in his model that fracture had contact area as well as roughness. Neuzil and Tracy (1981) modeled fracture flow by representing fractures as a set of parallel openings with different apertures. They generated an aperture distribution through a lognormal distribution and analyzed the flow through a numerical study. They pointed out that the flow is governed by the cubic law and also that maximum flow occurs through large apertures, however, their results did not match with the results from actual core experiments.

Witherspoon et al. (1980) showed that the cubic law was found valid whether the fracture surface was held open or was being closed under stress and the results were independent from rock type. Brown (1987b) investigated the effect of surface roughness on fluid flow through rock joints. He observed that the deviations of fluid flow from cubic law might be caused by the fracture roughness and fracture surface contact points.

The applicability of the cubic law to flow in fractures has been explored by many other investigators experimentally (Snow (1969), Tsang (1989), Hakami and Larsson (1996)). Deviations from cubic law behaviour have been attributed to several reasons each time. However, none of these researchers provided a definite picture or reason of the deviation.

2.4 FRACTURE ROUGHNESS

2.4.1 Roughness Measurement

In order to obtain reliable results from the quantitative analysis, it is essential to use the most accurate data acquired from fracture surface roughness measurements. Therefore, the decision on the most efficient roughness measurement method is necessary (Develi et al., 2001).

There are many different measurement methods developed for roughness measurement, such as mechanical, photographic, neutron and X-ray scattering, laser profilometry and optical measurement methods. However, each of them has their own limitations.

One of the first developed mechanical methods for measurements is stereodepth measurement microscope which was recording the roughness profiles multidirectionally on a x-y recorder (Rengers, 1970). The field measurements of surface roughness was conducted with a device called profilograph developed by Fecker and Rengers (1971) which was able to simplify to scan and map the surface roughness of large-sized samples in the field. They also introduced the application of normal geological compass and base plates for the same purpose.

Brown and Scholz (1985) were the first to present the stylus profilometer, another mechanical device to measure the roughness. The ancestors of the device were capable to measure small scale roughness profiles for laboratory studies. Kulatilake et al. (1995) used stylus profilometer to scan the surface roughness of silicone rubber casts representing natural rock joints of 0.1m in diameter. The same device was also used by Power et al. (1987) for larger scale measurements and by Schmittbuhl et al., (1995) for laboratory scale surface roughness measurements and mapping the surface by scanning the parallel profiles. The field scale applications of the device were performed by Schmittbuhl et al. (1993) to scan the surface of 600 mm long fault.

Ferraro and Giani (1990) used a mechanical comparator which reads manually the elevations on a fracture surface divided into grids. This is a simpler and more convenient method in terms of the size of the sample as it works manually. However, increasing the size of the sample does also increase the time and the effort spent for the measurements.

Other methods were also developed such as photographic and image processing tools (Krohn and Thompson, 1986) to obtain the surface roughness data provided by the scanning electron microscope (SEM). They scanned the sandstone samples in microstructure scale. Pande et al. (1987) used the photographs of SEM images of titanium fracture surface for the fractal analysis. Ord and Cheung (1991) presented the 3D surface topography using the optical measurement methods. Jessell et al. (1995) used the digital photogrammetry methods for the same purpose

There are other methods developed for scanning the surface of fractures such as optical and visual methods which are especially suitable for smaller-scale measurements of metal surfaces. Lin and Peng (1998) used scanning probe microscopy for nano-scale measurements. Grigoriev et al. (1998), Jakobs et al. (1998) and Brinksmeier and Riemer (1998) used atomic force microscopy for 3D mapping of the surface microtopography whereas Wyant and Schmit (1998) and Gleyzes et al. (1998) used interferometry methods for the same application. Nowicki and Jarkiewicz (1998) performed measurements with fringe-field capacitive method for dynamic conditions. A method using standard vision is applied by Kiran et al. (1998) for scanning the surface in micron-scale.

Larger scale surface roughness detection methods are applied by Mark and Aronson (1984) and Yokoya et al., (1989). They reviewed the topography of surfaces using the maps obtained by photographic methods. Ultrasound and pneumatic devices are also used for surface roughness detection (Blessing and Eitzen, 1988 and Wooley, 1991 respectively).

Develi et al. (2001) developed a method for scanning especially small-size samples with computer-controlled system. They conducted experiments on naturally and artificially fractured surfaces and obtained 3D images and contour maps of them. The system includes as scanning 54 mm x 54 mm surface with maximum 1mm resolution in x-y direction and 0.1mm in z direction. The data provided by the device was found to be suitable for both qualitative and quantitative analysis.

2.4.2 Numerical Techniques

Fracture surface characterization can be investigated with fractal analysis because fracture surfaces have been observed to represent fractal characteristic (Babadagli and Develi, 2000). Many methods have been developed for measuring the fractal dimensions of fracture surfaces. Brown and Scholz (1985) suggested that the fractal dimension provided by power spectral density method might be influenced by different frequency bands.

Shirono and Kulatilake (1997) have studied extensively the spectral method for the measurement of the self-affine roughness profiles to improve its accuracy. They focused mainly on smoothing/windowing the data and the input parameters for the generation of synthetic self-affine profiles such as generation level, seed value and variance. Using the same power spectral density method, Develi and Babadagli (1998) showed that the removal of the log cycle of low frequency band increases the fractal dimension. Their study demonstrated few important points not to be omitted during the fractal analysis such as sample size, removal of non-stationary parts and graphical analysis of the spectral data.

Roughness length and line scaling methods are performed by Develi and Babadagli (1998) and Kulatilake and Um (1999). They noticed that a suitable length exists for the roughness length method to obtain accurate fractal dimension values. This window length is determined by the size of the sample.

Babadagli and Develi (2000) made use of variogram and power spectral density methods to determine fractal dimension of fracture surfaces. They used synthetic 2D data sets generated from fractional Brownian motion (fBm). They noticed that the size of the 2D data set is critical issue for determining the fractal dimension. They also applied these methods for natural fracture surfaces and observed consistent fractal dimensions.

CHAPTER 3 : NUMERICAL MODELING OF BALLOONING IN A SINGLE FRACTURE

3.1 MODEL DEVELOPMENT

The objective of this chapter is to review the governing equations and develop a hydrodynamic lubrication model to analyze borehole ballooning problems. The complexity of fluid flow in a natural fracture is mainly due to the rock surface roughness and the rheology of the fluid flowing through the rough surface. Viscous fluid flow in fractures is commonly analyzed by using the Navier-Stokes (NS) equations of fluid mechanics. In this study, the lubrication theory is used to investigate the mechanics of borehole ballooning. Lubrication theory begins with the continuity and momentum equations. Utilizing simplifications consistent with hydrodynamic lubrication theory will yield to the most commonly encountered form of the Reynolds Equation, which is employed to determine the pressure and velocity profile distribution within the fracture.

3.1.1 Continuity and Momentum Equations

The continuity and momentum equations represent the laws that govern conservation of mass and momentum respectively. These equations indicate how mass and momentum of the fluid change with position and time. It is necessary to outline the derivation of these equations, in view of the fact that these equations form the base of the analytical model developed in this thesis.

The equation of continuity is developed by establishing a mass balance over a stationary volume. The fluid is assumed to flow through an arbitrary and stationary region in space of volume element $\Delta x \Delta y \Delta z$ shown in Figure 3-1.

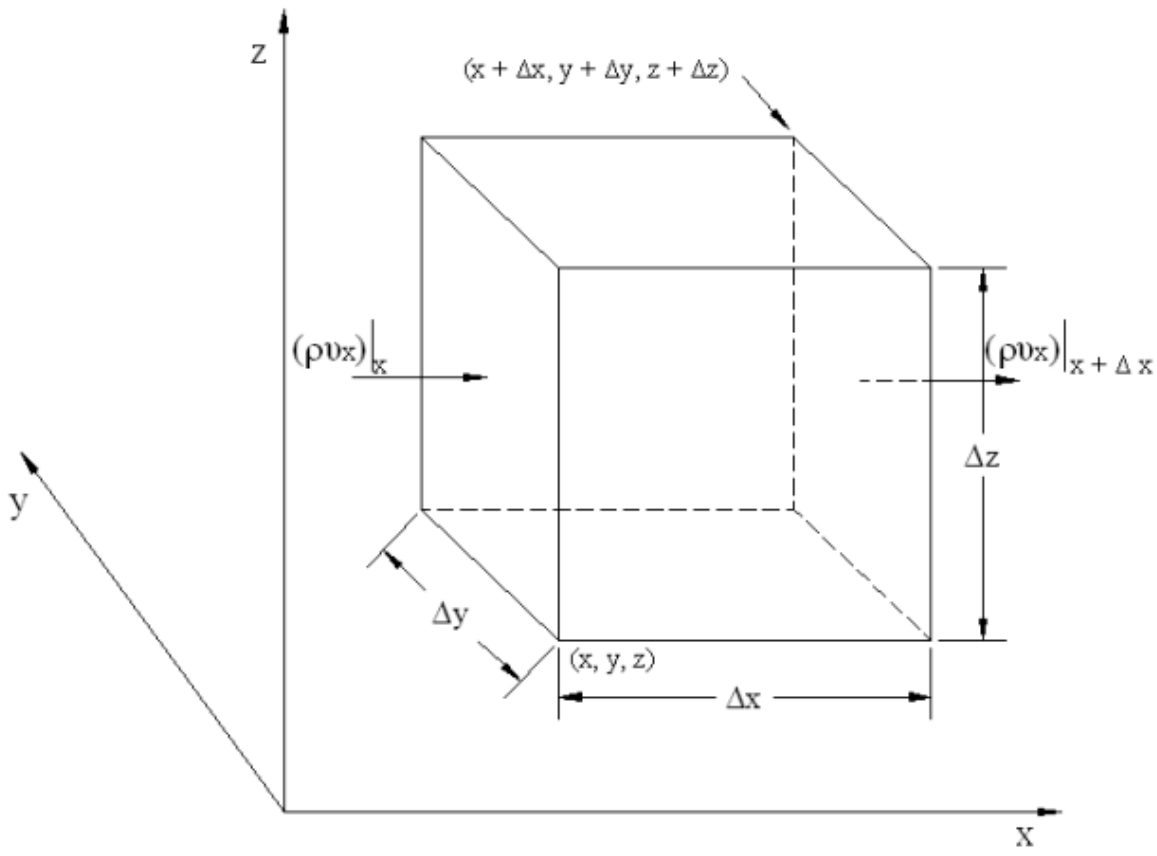

Figure 3-1: An arbitrary and stationary region in space of volume element ΔxΔyΔz

$$\frac{\partial \rho}{\partial t} = -\left[\frac{\partial}{\partial x}\rho \upsilon_x + \frac{\partial}{\partial y}\rho \upsilon_y + \frac{\partial}{\partial z}\rho \upsilon_z\right] \quad \text{.....(1)}$$

The derivation of the continuity equation (Eqn. 1) is given in Appendix A.

The momentum equation is a statement of Newton's Second Law and relates the sum of the forces acting on an element of fluid to its acceleration or rate of change of momentum. The momentum balance for a volume element of ΔxΔyΔz shown in Figure 3-2 can be summarized as follows:

Rate of Momentum Accumulation	=	Rate of Momentum in	-	Rate of Momentum out	+	Sum of forces acting on the system

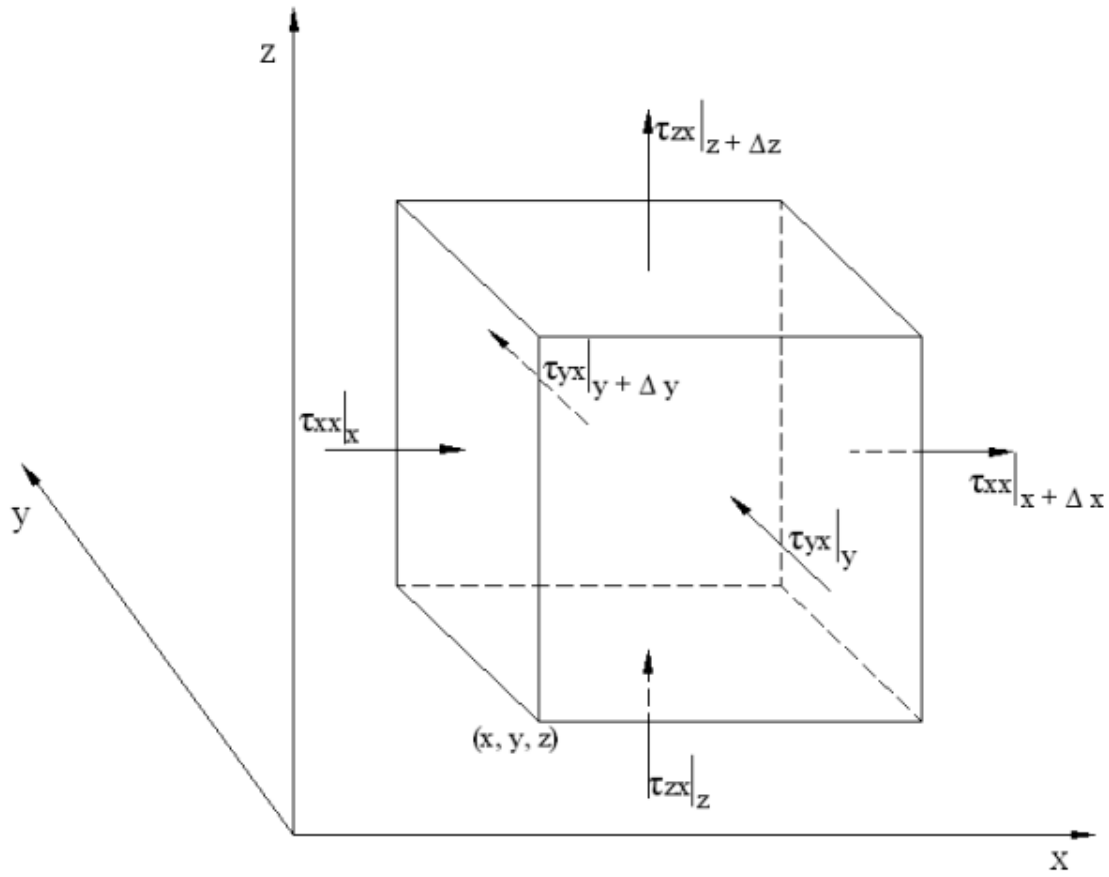

Figure 3-2: Volume element $\Delta x \Delta y \Delta z$ with arrows specifying the direction in which the x-component of momentum is transported

Derivation of the momentum equation (Eqn. 2) is given in Appendix B.

$$\rho \frac{Dv}{Dt} = -\nabla p - \left[\nabla \cdot \tau\right] + \rho g \quad \text{.....(2)}$$

In order to use the continuity and momentum equations to determine the velocity distributions, explicit expressions for the stresses in terms of velocity gradients and fluid properties must be introduced into the momentum equation (Eqn. 2). For the Newtonian fluids, explicit expressions of stresses acting on the various surfaces of control volume are given in the Appendix B throughout the equations B-13 to B-18.

For constant density and constant viscosity, the velocity and pressure gradient incorporated form of the momentum equation may be simplified by using the fact that continuity equation becomes nil.

$$\rho \frac{Dv}{Dt} = -\nabla P + \mu \nabla^2 v + \rho g \quad \text{.....(3)}$$

Equation 3 is the Navier-Stokes equation, first developed by Claude Louis Navier (1822) by molecular arrangements.

3.1.2 Reynolds Lubrication Theory

The study of hydrodynamic lubrication is, from a mathematical point of view, the study of a particular form of Navier-Stokes equations. The classical theory of the hydrodynamic lubrication for a Newtonian fluid was first presented by Osborne Reynolds (1886). The Reynolds equation is derived from Navier-Stokes equations by making the following assumptions:

(1) The thickness of the fluid, z, is very small compared to the width and length, x, y.
(2) The pressure across the fluid film does not vary.

$$\frac{\partial p}{\partial z} = 0 \quad \text{.....(4)}$$

(3) The flow is laminar and no turbulence occurs anywhere in the film.

(4) No external forces act on the film.

$$g_x = g_y = g_z = 0 \quad \text{.....(5)}$$

(5) Fluid inertia is very small compared to the viscous shear. These inertia forces consist of acceleration of the fluid and can be neglected.

$$\frac{Dv_x}{Dt} = \frac{Dv_y}{Dt} = \frac{Dv_z}{Dt} = 0 \quad \text{.....(6)}$$

(6) No slip at the surfaces.

(7) All other velocity gradients can be neglected compared to $\partial v_x / \partial z$ and $\partial v_y / \partial z$. Since v_x and v_y are predominant velocities and z is a dimension much smaller than x and y, the above assumption is valid. The velocity gradients can be considered shears, while all others are acceleration terms.

Details of the derivation of the Reynolds equation (Eqn. 7) from Navier Stokes equations are shown in Appendix C. Derivation is carried out by considering the restrictions and assumptions inherent in the equations used in the solution of lubrication problems. Assumptions 1 to 7 will lead the Navier Stokes equations to the Reynolds equation for an incompressible flow in two dimensional Cartesian coordinates (Eqn. 7)

$$\frac{\partial}{\partial x}\left(\frac{w^3}{\mu}\frac{\partial P}{\partial x}\right) + \frac{\partial}{\partial y}\left(\frac{w^3}{\mu}\frac{\partial P}{\partial y}\right) = 12\frac{\partial w}{\partial t} \quad \text{.....(7)}$$

3.1.3 Model Geometry and Boundary Conditions

Flow in a single fracture can be analyzed if the flow factors controlling the flow such as fluid rheological properties, fracture geometry, and boundary conditions of the fracture are known. A 2D planar, horizontal, square shaped fracture in a non-permeable formation is considered in this study. Figure 3-3 illustrates the shape of the fracture hit by the wellbore from one side.

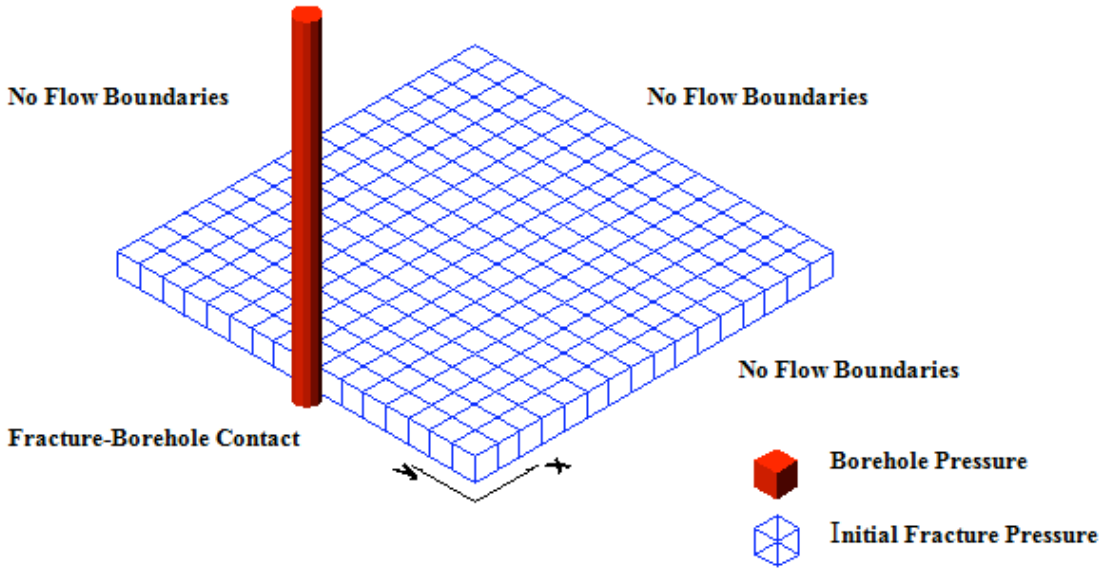

Figure 3-3: Schematic representation of fracture-borehole contact model

The following form of the Reynolds equation was used to build a two dimensional transient model of ballooning phenomenon in Cartesian coordinates.

$$\frac{\partial}{\partial x}\left(\frac{w^3}{12\mu}\frac{\partial P}{\partial x}\right)+\frac{\partial}{\partial y}\left(\frac{w^3}{12\mu}\frac{\partial P}{\partial y}\right)=\frac{\partial w}{\partial t} \quad \text{.....(8)}$$

The Equation 8 was solved by using finite difference approximation explicitly. The velocity and pressure profiles within the fracture as well as the fluid loss and gain rate between borehole and fractured formation were evaluated.

Initial Condition

Initial pressure within the fracture, P_0 is assumed to be constant.

Boundary Conditions

$$\frac{\partial p}{\partial x} = 0 : (x, y) \in \left(0 \le y \le L_y \cap x = L_x\right)$$
$$\frac{\partial p}{\partial y} = 0 : (x, y) \in \left(0 \le x \le L_x \cap y = 0\right)$$
$$\frac{\partial p}{\partial y} = 0 : (x, y) \in \left(0 \le x \le L_x \cap y = L_y\right) \quad \text{.....(9)}$$

3.2 FRACTURE DEFORMATION LAW

The main mechanism behind borehole ballooning is the opening and closing of the natural rough fractures intersected by the wellbore due to the alterations in bottom hole pressure. The single fracture in our model is assumed to obey a specific deformation law while investigating the borehole ballooning phenomenon. Two types of deformation laws commonly used in the literature to describe the fracture deformation as a function of wellbore pressure: linear and exponential laws. Both deformation laws were incorporated into the Reynolds equation in this study.

3.2.1 Linear Deformation Law

Lavrov and Tronvoll (2005) proposed to use the linear deformation law describing how fracture aperture changes as a function of the fluid pressure:

$$w = w_0 + \frac{p}{K_n} \quad \text{.....(10)}$$

where w_0 is the initial distance between fracture surfaces and K_n represents normal stiffness of the fracture. Here, fracture aperture in a given point is assumed to be a linear function of the fluid pressure inside the fracture in that point.

3.2.2 Exponential Deformation Law

Bruel et al. (1994) proposed an empirical exponential law describing how fracture aperture changes as a function of fluid pressure:

$$\begin{aligned} w &= w_0 \exp\left[-\beta\left(\sigma_n - p\right)/3\right] \\ \sigma_n &= \sigma_v \cos^2\alpha + \sigma_h \sin^2\alpha \\ \sigma_v &= \rho_r g d \end{aligned} \quad \text{.....(11)}$$

Here w is the fracture aperture in a particular grid, p is the fluid pressure and σ_n is the normal stress. w_0 is the initial distance between fracture surfaces and β is an empirical coefficient.

Equations 10 and 11 were substituted into the Reynolds equation (Eqn. 7) independently and the resulting partial differential equations were solved by finite difference approximation.

3.3 NUMERICAL SOLUTION TECHNIQUE

The Reynolds equation for an incompressible flow in two dimensional Cartesian coordinates was given in Equation 7. Since the main mechanism behind borehole ballooning is deformation of the fracture due to the changes in borehole pressure, fracture aperture term in Reynolds equation, "w", is substituted with linear and exponential fracture deformation law equations (Eqns. 10 and 11) independently.

The resulting equation for a Newtonian fluid under linear deformation law assumption is:

$$\frac{\partial}{\partial x}\left(\left(w_0+\frac{P}{K_n}\right)^3\left(\frac{\partial P}{\partial x}\right)\right)+\frac{\partial}{\partial y}\left(\left(w_0+\frac{P}{K_n}\right)^3\left(\frac{\partial P}{\partial y}\right)\right)=12(\mu)\frac{\partial\left(w_0+\frac{P}{K_n}\right)}{\partial t} \quad \text{.....(12)}$$

The resulting equation for a Power Law fluid under linear deformation law assumption is:

$$\frac{\partial}{\partial x}\left(\left(w_0+\frac{P}{K_n}\right)^{\frac{2n+1}{n}}\left(\left(\frac{\partial P}{\partial x}\right)\left|\frac{\partial P}{\partial x}\right|^{\frac{1-n}{n}}\right)\right)+\frac{\partial}{\partial y}\left(\left(w_0+\frac{P}{K_n}\right)^{\frac{2n+1}{n}}\left(\left(\frac{\partial P}{\partial y}\right)\left|\frac{\partial P}{\partial y}\right|^{\frac{1-n}{n}}\right)\right)= \quad \text{.....(13)}$$

$$\left(\frac{2n+1}{n}\right)(2)^{\frac{n+1}{n}}(K)^{\frac{1}{n}}\frac{\partial\left(w_0+\frac{P}{K_n}\right)}{\partial t}$$

The resulting equation for a Newtonian fluid under exponential deformation law assumption is:

$$\frac{\partial}{\partial x}\left(\left(\left(w_0(k,l)\exp\left(-\beta(\sigma_n-P)/3\right)\right)\right)^3\left(\frac{\partial P}{\partial x}\right)\right)+\frac{\partial}{\partial y}\left(\left(\left(w_0(k,l)\exp\left(-\beta(\sigma_n-P)/3\right)\right)\right)^3\left(\frac{\partial P}{\partial y}\right)\right)=$$

$$12(\mu)\frac{\partial\left(\left(w_0(k,l)\exp\left(-\beta(\sigma_n-P)/3\right)\right)\right)}{\partial t}$$

.....(14)

The resulting equation for a Power Law fluid under exponential deformation law assumption is:

$$\frac{\partial}{\partial x}\left(\left(w_0(k,l)\exp\left(-\beta(\sigma_n-P)/3\right)\right)^{\frac{2n+1}{n}}\left(\left(\frac{\partial P}{\partial x}\right)\left|\frac{\partial P}{\partial x}\right|^{\frac{1-n}{n}}\right)\right)+$$

$$\frac{\partial}{\partial y}\left(\left(w_0(k,l)\exp\left(-\beta(\sigma_n-P)/3\right)\right)^{\frac{2n+1}{n}}\left(\left(\frac{\partial P}{\partial y}\right)\left|\frac{\partial P}{\partial y}\right|^{\frac{1-n}{n}}\right)\right)= \text{.....(15)}$$

$$\left(\frac{2n+1}{n}\right)(2)^{\frac{n+1}{n}}(K)^{\frac{1}{n}}\frac{\partial\left(w_0(k,l)\exp\left(-\beta(\sigma_n-P)/3\right)\right)}{\partial t}$$

These non-linear partial differential equations (Forms of Reynolds equation) shown in Equations 12, 13,14 and 15 were solved by using finite difference approximation explicitly. Computational stability is verified by looking at the output at various time steps.

The explicit finite difference scheme for Newtonian fluids under linear deformation law assumption is constructed as follows:

$$P_{k,l}^{j+1}=P_{k,l}^{j}+\left(\begin{array}{l}\left(\left((\Delta t)\left(1/(12\cdot\mu)\right)\right)(K_n)\right)\cdot \\ \left(\frac{\partial}{\partial x}\left(\left(w_0+\frac{P}{K_n}\right)^3\cdot\left(\frac{\partial P}{\partial x}\right)\right)\right)+\left(\frac{\partial}{\partial y}\left(\left(w_0+\frac{P}{K_n}\right)^3\left(\frac{\partial P}{\partial y}\right)\right)\right)\end{array}\right)\text{.....(16)}$$

$$P_{k,l}^{j+1} = P_{k,l}^{j} + \left(\left((\Delta t) \cdot \left({}^{1}\!/\!_{(12 \cdot \mu)} \right) \cdot (K_n) \right) \cdot \left(\left(\left(\left(\left(\left(\left(w_0(k,l) \right) + \left(\left(P_{k+1,l}^{j} + P_{k,l}^{j} \right) / (2 \cdot K_n) \right) \right)^{(3)} \right) \cdot \left(\left(\left(\left(P_{k+1,l}^{j} - P_{k,l}^{j} \right) / \Delta x \right) \right) \right) \right) / (\Delta x) \right) - \left(\left(\left(\left(w_0(k,l) \right) + \left(\left(P_{k,l}^{j} + P_{k-1,l}^{j} \right) / (2 \cdot K_n) \right) \right)^{(3)} \right) \cdot \left(\left(\left(\left(P_{k,l}^{j} - P_{k-1,l}^{j} \right) / \Delta x \right) \right) \right) \right) / (\Delta x) \right) + \left(\left(\left(\left(\left(\left(w_0(k,l) \right) + \left(\left(P_{k,l+1}^{j} + P_{k,l}^{j} \right) / (2 \cdot K_n) \right) \right)^{(3)} \right) \cdot \left(\left(\left(\left(P_{k,l+1}^{j} - P_{k,l}^{j} \right) / \Delta y \right) \right) \right) \right) / (\Delta y) \right) - \left(\left(\left(\left(w_0(k,l) \right) + \left(\left(P_{k,l}^{j} + P_{k,l-1}^{j} \right) / (2 \cdot K_n) \right) \right)^{(3)} \right) \cdot \left(\left(\left(\left(P_{k,l}^{j} - P_{k,l-1}^{j} \right) / \Delta y \right) \right) \right) \right) / (\Delta y) \right) \right) \right) \right) \quad \text{.....(17)}$$

The explicit finite difference scheme for Newtonian fluids under exponential deformation law assumption and the scheme for Power Law fluids under exponential deformation law assumption are constructed and shown in Appendix F.

3.4 PARALLEL PLATE MODEL AND CUBIC LAW

The simplest model of fluid flow through a fracture is the parallel plate model whose implementation yields to the wellknown “cubic law”.

One of the main assumptions made in the derivation of the cubic law is that the fracture has smooth and parallel surfaces separated by an aperture height, w (Fig. 3-4).

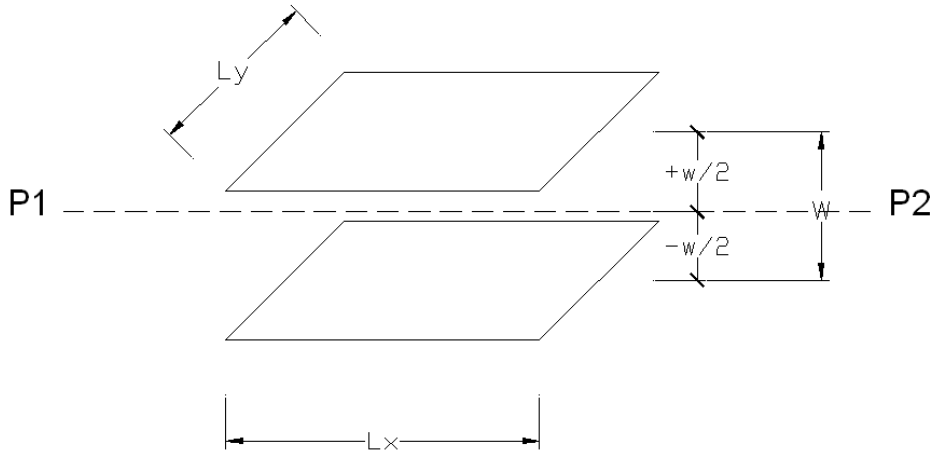

Figure 3-4: Parallel plate model assumptions illustration

A flow is called parallel if only one velocity component is different from zero and all fluid particles move in one direction, i.e. the fluid velocities in y and z directions (v_y and v_z) are equal to zero. Consequently, it can be shown from continuity equation that $\partial v_x/\partial x$ is also equal to zero.

In summary:

$v_y=v_z=0 \rightarrow v_x=v(y,z,t)$

$\partial v_x/\partial x=0$

From Navier Stokes equations for x and y directions can be figured out that ∂P/∂y and ∂P/∂z are equal to zero. The pressure depends only on x. In the Navier Stokes equation for x direction all convective terms disappear.

$$\frac{\left(\partial \rho v_x\right)}{\partial t} = -\left(\cancel{\frac{\partial}{\partial x}\rho v_x v_x} + \cancel{\frac{\partial}{\partial y}\rho v_y v_x} + \cancel{\frac{\partial}{\partial z}\rho v_z v_x}\right) - \left(\frac{\partial}{\partial x}\tau_{xx} + \frac{\partial}{\partial y}\tau_{yx} + \frac{\partial}{\partial z}\tau_{zx}\right) - \frac{\partial P}{\partial x} + \cancel{\rho g} \quad (18)$$

When the fluid flows in the x direction between two parallel plates perpendicular to z direction, then the stress equations give:

$$\tau_{xx} = \tau_{yy} = \tau_{zz} = \tau_{yz} = \tau_{xy} = 0 \quad (19)$$

$$\frac{\left(\partial \rho v_x\right)}{\partial t} = -\frac{\partial P}{\partial x} - \left(\frac{\partial}{\partial z}\tau_{zx}\right) \quad (20)$$

$$\rho \frac{\partial v_x}{\partial t} = -\frac{dP}{dx} + \left(\frac{\partial}{\partial z}\tau_{zx}\right) \quad (21)$$

The transport rate of momentum is determined by multiplying the momentum flux due to shear stress by the area over which the shear stress acts. The fluid is flowing in the horizontal direction and the only force acting on the fluid is ΔP due to the pressure differential ($\Delta P = P_1 - P_2$) across the x-direction of the control volume (L). The net pressure force is obtained by multiplying the pressure difference with surface area over which ΔP acts. General equation for Newtonian and non-Newtonian fluids is as follows:

$$\frac{\Delta P}{L_x} = \left(\frac{\partial}{\partial z}\tau_{zx}\right) \quad (22)$$

Fluids are classified as Newtonian and Non-Newtonian fluids according to their rheological properties. For a Newtonian fluid, shear stress is directly proportional to the shear rate and the constant of the proportionality is known as fluid viscosity. Equation 13 shows the velocity distribution of a Newtonian fluid in laminar flow conditions between two parallel plates. The same procedure is followed for Power-Law, Bingham Plastic and Yield Power Law fluids and their velocity profiles between two parallel plates are derived and shown in Appendix E, respectively.

$$v_x = \frac{\Delta P}{L_x}\frac{1}{2\mu}\left(\left(\frac{w}{2}\right)^2 - z^2\right) \quad \text{.....(23)}$$

The velocity profile shown in Equation 23 can be integrated across the fracture to find the overall flow rate as shown in Appendix D.

$$Q_x = L_y \frac{\Delta P}{L_x}\frac{1}{2\mu}\left(\frac{w^3}{4} - \frac{w^3}{12}\right) = L_y \frac{\Delta P}{L_x}\frac{w^3}{12\mu} \quad \text{.....(24)}$$

Equation 24 is the so called cubic law, where the flow rate varies as a function of the cube of the separation between two plates w (Figure 3-4). Here L_y is the depth of the parallel plate, perpendicular to the flow direction, μ is the dynamic viscosity of the fluid and $\Delta P / L_x$ is the magnitude of the pressure gradient along the fracture. The same method is applied for non-Newtonian type fluids and the flow rate profiles of Power Law, Bingham Plastic and Yield Power Law fluids are derived by integrating their velocity profiles across the fracture with flow between two parallel plates assumption. The complete derivation of flow rate distribution equations for different rheological models is shown in Appendix E.

3.5 GENERATION OF FRACTAL SURFACES

The fractal nature of fracture surfaces was first observed in the 1980s (Mandelbrot et al., 1984; Brown and Scholz, 1985; Brown, 1987a). Later, different fractal approaches were reported for characterization and mapping of fracture surfaces (Turk et al., 1987; Huang et al. 1992; Den Outer et al., 1995; Develi and Babadagli, 1998) as well as generating 2-D fractal fracture surfaces (Fournier et al., 1982; Voss, 1985; Wong et al., 1986; Brown, 1987b; Wang et al., 1987; Saupe, 1988). Fluid flow applications were also performed on the computer generated fractal fracture surfaces for single-phase flow mainly focusing on the deviations from the cubic law (Oron and Berkowitz, 1998; Brush and Thomson, 2002).

The mechanical and transport characteristics of any fracture system are influenced by the roughness of fracture surfaces (Babadagli and Develi, 2001). Hence, the fracture surface roughness is expected to play a major role on the magnitude of borehole ballooning. This study has been motivated by the need of a more realistic approach for modeling borehole ballooning/breathing applicable to horizontal fractures with rough surfaces. The main objective is to quantify the effect of fracture surface roughness on borehole ballooning by using computer generated fractal fracture surfaces coupled with a numerical model that simulates the process. A single horizontal fracture with rough surfaces intersected by the wellbore was considered to show the effect of roughness on the ballooning process. 2D fractal distributions with different Hurst exponents (or fractal dimensions) that represent rough fracture surfaces (and apertures) were generated using fractional Brownian motion (fBm) for 16x16, 32x32 and 64x64 grid sizes. These 2D data sets acquired from synthetically generated fracture surfaces were incorporated into the equation governing fluid flow in a single horizontal fracture. Fluid loss and gain rate between the borehole and the imaginary rough fracture were computationally studied and analyses on the importance of fracture roughness were provided by identifying the situations where the roughness starts becoming an effective parameter on the process.

Mandelbrot (1982) introduced the fractional Brownian motion (fBm) concept as a generalization of the random function. Consider $B_H(x)$ as a stationary stochastic process with the following mean:

$$\left\langle B_H(x) - B_H(x_0) \right\rangle = 0 \quad \text{.....(25)}$$

and a variance of increments $\sigma^2 (x\text{-}x_0)$ is given by

$$\left\langle \left[B_H(x) - B_H(x_0) \right]^2 \right\rangle = |x|^{2H} \sigma_0^2 \quad \text{.....(26)}$$

where x and x_0 values are arbitrary points in space and H is called as the Hurst exponent. This stochastic process is called fractional Brownian motion (fBm).

Several techniques have been proposed to generate 2D fBm surfaces synthetically. In this study, the methodology known as successive random addition and mid-point displacement proposed by Voss (1985) was followed to generate the self affine fractal (fBm) surfaces. The first generation step is initiated by assigning an independent Gaussian variable with zero mean and unit variance at the central point of the lattice. Next the elevations at the four corner points are interpolated and at each step, σ is reduced as

$$\sigma_n^2 = \sigma_{n-1}^2 \left(\frac{1}{2} \right)^{2H} = \left(\frac{1}{2} \right)^{2Hn} \sigma_0^2 \quad \text{.....(27)}$$

A schematic representation of the derivation process is presented in Figure 3-5 for a 1-D case. The interpolation starts with an overall characteristic variance (σ_0^2). Then a random number drawn from a Gaussian distribution with zero mean and variance (σ_1^2) is added as illustrated in Figure 3-5 (Hewett, 1986; Emanuel et al., 1989).

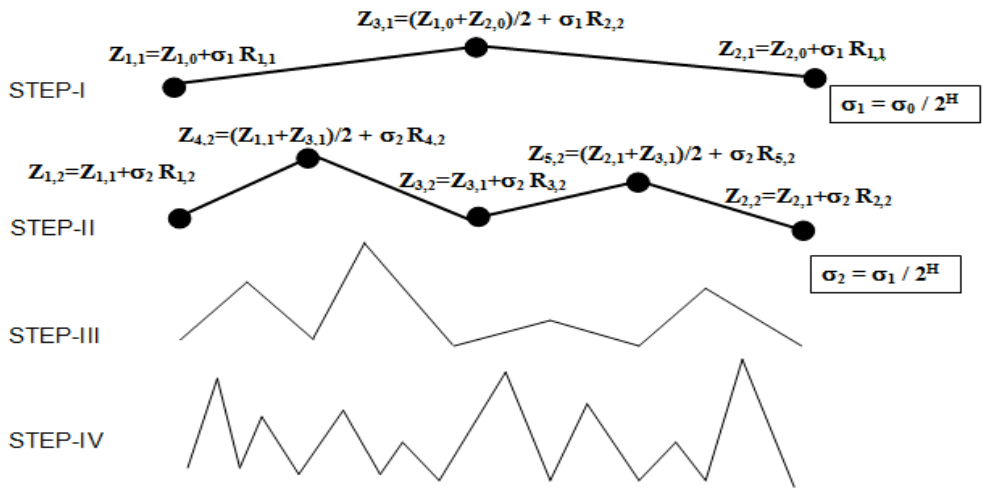

Figure 3-5: Schematic representation (1-D) of mid-point displacement and successive random addition process to generate fBm surfaces. Z is the variable, height (elevation) of the point in our case (Voss, 1985 and Emanuel et al., 1989)

Using this technique, two different sets (named as set "a" and set "d") of 2D synthetic surfaces with known Hurst exponent utilizing two different random number seeds were generated. Here the Hurst exponent is related to the fractal dimension as D = 3 – H. The apertures generated by the difference between two surfaces and surface roughnesses through this methodology are representative of natural fracture surfaces of sedimentary rocks (Develi and Babadagli, 1998 and Babadagli and Develi, 2002). Note that the difference between two rough fracture surfaces will yield a fracture aperture with the same fractal dimension as the surfaces (Babadagli, 2005).

The Hurst exponent, H describes the degree of roughness of the fBm traces and decreasing H leads to more rough distributions. Bigger H, e.g., 0.9, yields a smoother distribution, which is almost equal to perfectly smooth fracture surfaces that is defined by H=1. Hence, each set was generated for three different H varying from 0.4 to 0.9 in order to identify the importance of the degree of roughness on borehole ballooning. Note that this range of Hurst exponent represents typical surface roughness and aperture values for sedimentary rocks (Develi and Babadagli, 1998 and Babadagli and Develi, 2002). Figure 3-6 demonstrates two sets "a" and "d" of surfaces with the same grid size but different Hurst exponents.

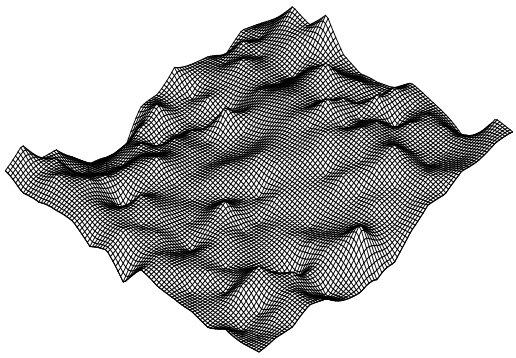

H = 0.4, D = 2.6, 16x16
SEED “a”

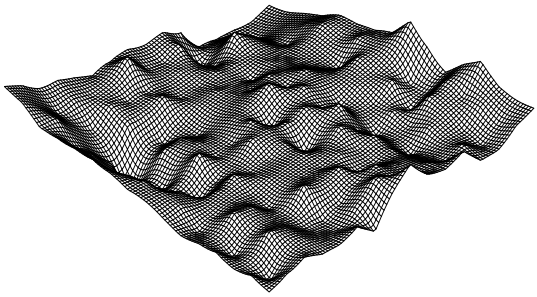

H = 0.4, D = 2.6, 16x16
SEED “d”

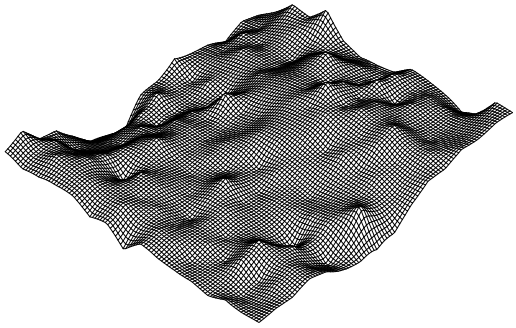

H = 0.6, D = 2.4, 16x16
SEED “a”

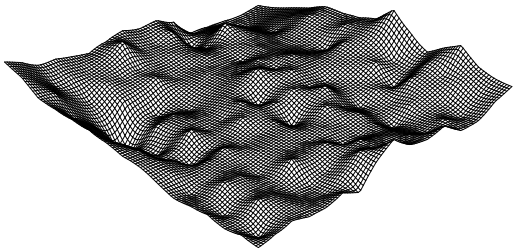

H = 0.6, D = 2.4, 16x16
SEED “d”

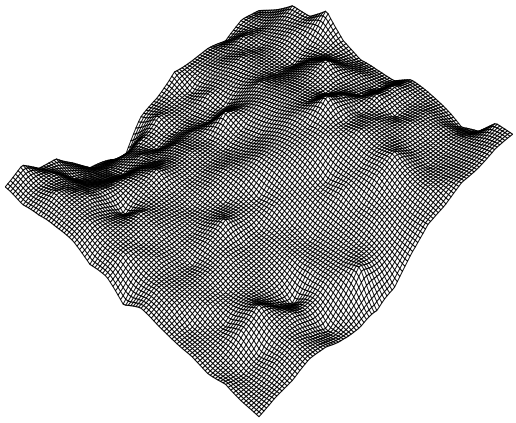

H = 0.9, D = 2.1, 16x16
SEED “a”

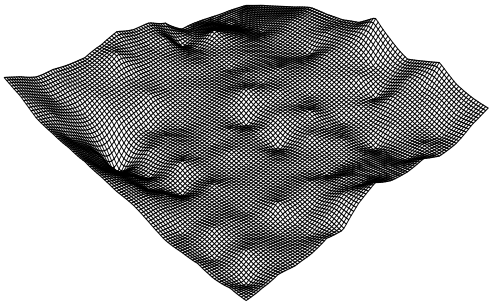

H = 0.9, D = 2.1, 16x16
SEED “d”

Figure 3-6: Examples of uneven aperture distributions, with the same size (16x16) but different fractal dimensions and different random number seeds, generated through midpoint displacement method

As Babadagli and Develi (2001) proposed, these fBm lattices can be used in simulating transport processes but they strongly recommended that one should be careful in selecting number of grids when applying the computer experiments. Therefore, different sizes of each set from 16x16 to 64x64 with different H values 0.4, 0.6 and 0.9 were generated to increase the accuracy of the model and to clarify effect of grid size on the results. Figure 3-7 shows the typical surfaces generated using the same random number seed and the same Hurst exponent but different grid sizes. As shown in Figure 3-7, all cases characterize the same roughness trend but with an increasing resolution as the number of data points increase. Note that the data generated through the methodology described above were converted to fracture aperture distribution with the same average aperture for the two different data sets. However, the range in aperture sizes was different in each case based on the value of the selected Hurst exponent. The fracture apertures were assigned to each numerical grid in the model to create a non-uniform aperture due to rough fracture surfaces. Table 3-1 summarizes the statistics of the aperture distributions for all of the rough surfaces investigated.

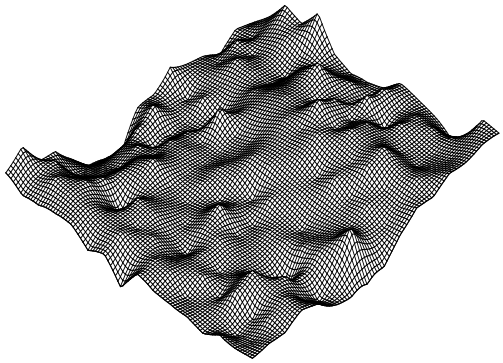

H = 0.4, D = 2.6, 16x16
SEED “a”

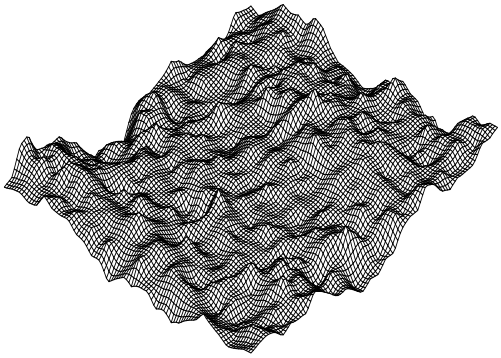

H = 0.4, D = 2.6, 32x32
SEED “a”

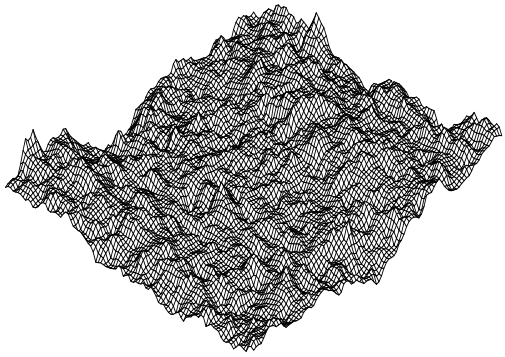

H = 0.4, D = 2.6, 64x64
SEED “a”

Figure 3-7: Aperture distributions generated with the same fractal dimension and random number seed but different grid sizes through midpoint displacement method

Table 3-1: Statistical Parameters of Fracture Aperture Data Sets

	Fracture Aperture Mean Value, mm	Fracture Aperture Standard Deviation	Fracture Aperture Minimum Value, mm	Fracture Aperture Maximum Value, mm	Fracture Initial Volume, m^3
Smooth Fracture	1	0	1	1	0.256
a04 Data Set	0.9919	0.000320	0.0000267	1.5918	0.2539
a06 Data Set	1.0057	0.000365	0.0000420	1.7685	0.2575
a09 Data Set	1.0005	0.000406	0.0000610	1.9165	0.2561
d04 Data Set	0.9958	0.000220	0.0000215	1.4821	0.2549
d06 Data Set	0.9994	0.000252	0.0003270	1.6648	0.2559
d09 Data Set	1.0007	0.000279	0.0000370	1.7787	0.2562

3.6 REFERENCE CASE

A 2D planar, horizontal, square shaped fracture in a non-permeable formation is considered in this study (Figure 3-8). To establish the base case, the fracture aperture is assumed to be the same over the entire fracture at the beginning. The fracture contains a fluid with a static formation pressure P_0. The drilling fluid and the fluid in the fracture are incompressible and assumed to have the same rheology. As drilling continues, the borehole intersects the fracture from one side at t=0. Right after the borehole hits the fracture, the uniform pressure at the contact side of the fracture with the borehole increases rapidly from P_0 and equalizes to wellbore pressure P_w in a very short time period, t_s, to mimic the mud loss event of borehole ballooning phenomenon. After a while, when the borehole pressure P_w is decreased to the uniform pressure level existing in the fracture before intersection again in t_s, the mud return event takes place from the fracture into the borehole. In other words, as soon as the dynamic wellbore conditions disappear and the bottomhole circulation pressure falls below the reservoir pressure during a pump-off period because of a connection or flow check operation, sizeable amount of mud is gained back into the wellbore. Figure 3-9 displays the pressure fluctuation leading to borehole ballooning at fracture side contacting the borehole for smooth and rough fractures. Table 3-2 shows the set of operational and geologic parameters utilized in computational simulations in this study.

Initially, the average smooth fracture aperture was assumed to be the same for all simulated cases. In order to investigate the effect of fractal fracture surface roughness on amount of mud loss/mud gains leading to borehole ballooning, all rough fracture apertures are generated with an average aperture of 1 mm and incorporated into the reference model which is giving the readers the opportunity to see the difference between mud losses/gains in rough and smooth fractures and particularly in rough fractures with different fractal dimensions.

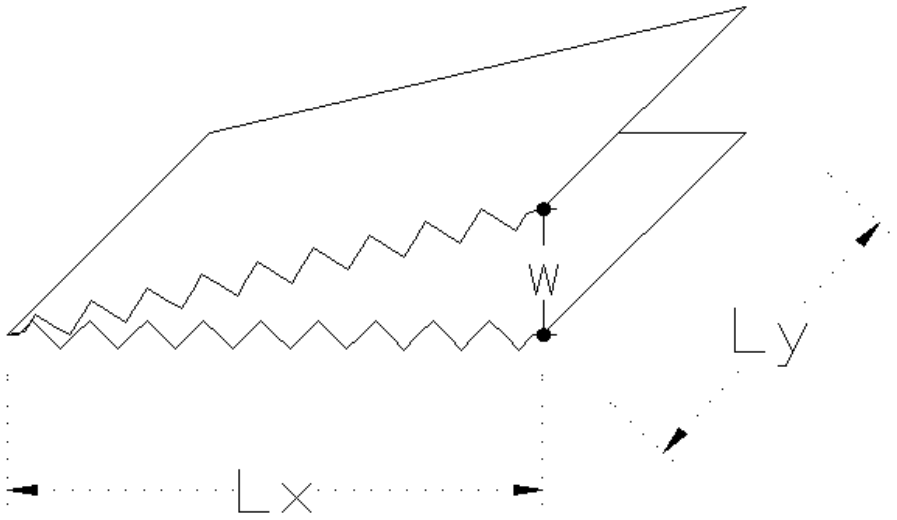

Figure 3-8: Two dimensional horizontal fracture model

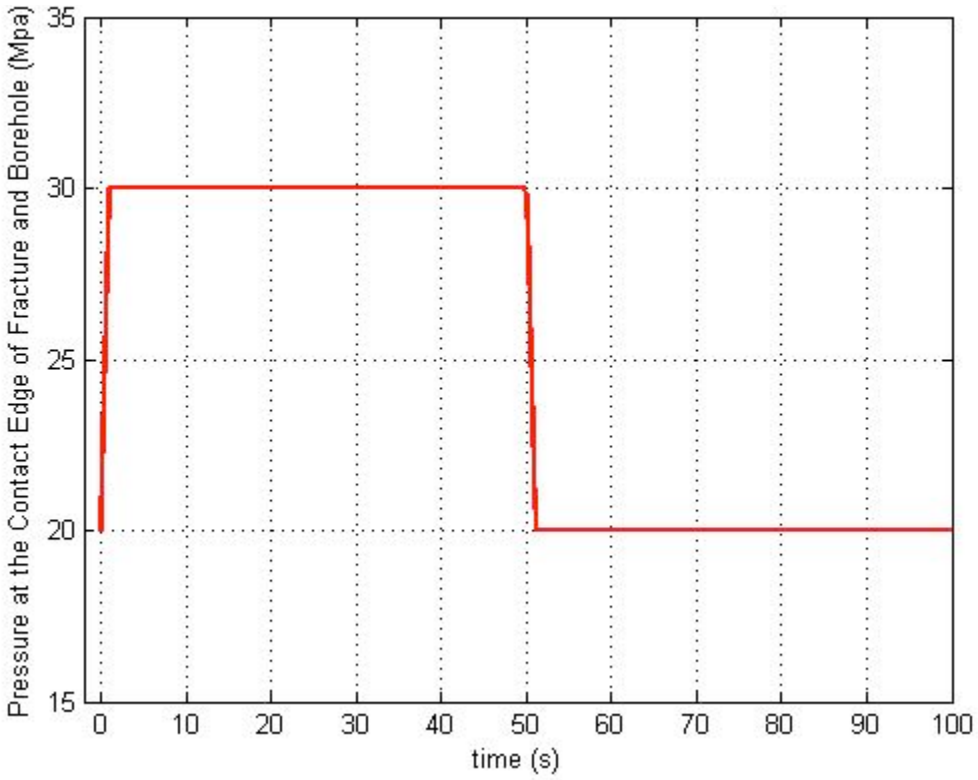

Figure 3-9: Pressure fluctuation vs. time at borehole-fracture contact

Table 3-2: Base data used for numerical simulation study.

Parameter	Value
x-discretization step	1 m
y-discretization step	1 m
Time discretization step	0.01 s
Dynamic mud viscosity, μ	0.001 Pa s
Fracture length, L_x *and* L_y	16 m
Fracture's normal stiffness, K_n	50000 MPa/m
Fracture's inclination, $\acute{\alpha}$	0
Fracture's initial smooth aperture	1 mm
Initial fluid pressure in the fracture, P_0	20 MPa
Well Pressure, P_W	30 MPa
Duration of pressure increase and decrease, t_s	1 s
Depth of the fracture, d	1000 m
Total duration of the simulations, t	100 s
Fracture's normal compressibility, β	10^{-7} Pa^{-1}
Rock density, ρ_r	2500 kg/m^3

Parametric studies of factors controlling borehole ballooning has been conducted by using the solution of the numerical model. Results of numerical modeling study are represented in Chapter 4.

CHAPTER 4 :PARAMETRIC STUDY OF THE FACTORS INFLUENCING THE MAGNITUDE OF BOREHOLE BALOONING

Equations governing borehole ballooning and the derivations of these equations are shown in Chapter 3 in detail. In this chapter the effects of various parameters on the magnitude of the fluid loss/gain during a ballooning event are analyzed numerically.

4.1 EFFECT OF DEFORMATION LAW ASSUMPTION

The linear and exponential deformation laws were compared to see their effects on the magnitude of the ballooning. Linear deformation law (Eqn. 17) suggested by Lavrov and Tronvoll (2005) is a simplified method, which is easy to incorporate into any mathematical model and saves computational time. Its origin is the exponential deformation law, which is described by Equation 18. The borehole ballooning phenomenon has been simulated by varying the borehole pressure between 20 and 30 MPa at the point where the borehole intersects the fracture.

Figure 4-1 illustrates the results of simulations carried out with the exponential and linear deformation law. The reference case data given in Table 3-1 are used in the simulations. Using the exponential deformation law instead of the linear deformation law showed a noticeable effect on fluid flow dynamics. It resulted lower mud loss and gain, lower flow rate peaks and a little slower decrease in fluid loss and gain rates. Overall, exponential deformation law assumption results less cumulative mud loss and gain than the linear deformation law simulations. However, it should be noted that the simulation results obtained by using the exponential deformation law are strongly dependent to the depth of the fracture beneath surface.

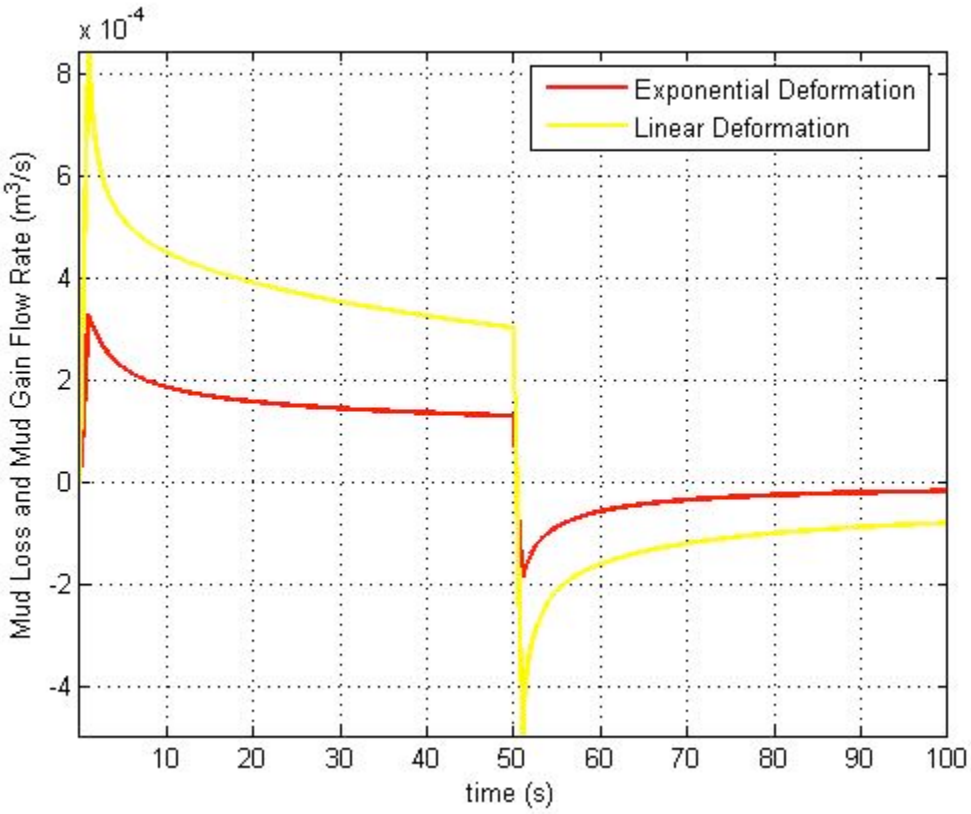

Figure 4-1: Reference case simulation results

4.2 EFFECT OF BOREHOLE PRESSURE

Borehole pressure is a critical parameter in drilling operations. Continuous losses occur while circulating the drilling fluid with a bottomhole pressure higher than the formation pressure, which generally causes the well to suffer from borehole ballooning.

Effect of the borehole pressure on mud loss/gain flow rate is investigated by running the simulator for three different borehole pressure values: 25 MPa, 30 MPa (reference case) and 35 MPa. All three cases correspond to an overbalanced drilling operation. The results of these three cases are shown in Figure 4-2.

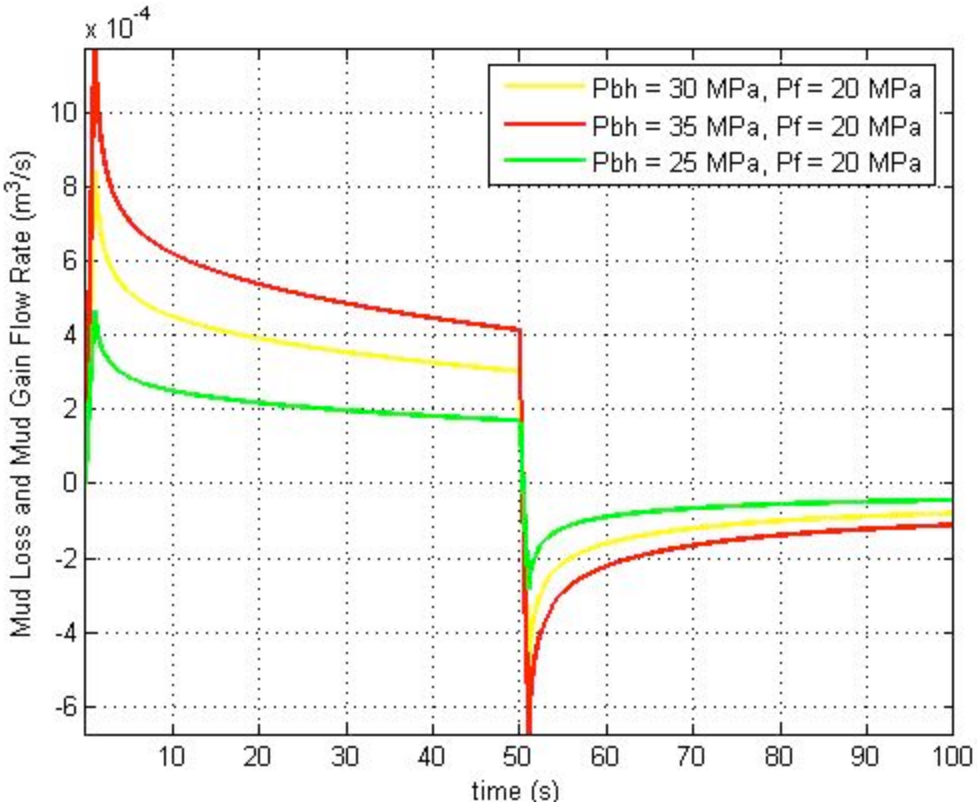

Figure 4-2: Effect of Borehole Pressure on the magnitude of borehole ballooning

Borehole pressure is expected to have a significant effect on the magnitude of fluid flow between the fracture and the wellbore. Increasing the bottomhole pressure considerably increases the mud loss/gain flow rate. It increases both initial and mid simulation peaks and the accompanying tails. This might be explained with the fact that the value of borehole pressure determines the pressure profile inside the fracture, when the new pressure equilibrium is eventually established. Mud loss/gain dynamics are found to be very sensitive towards well pressure variations.

4.3 EFFECT OF INITIAL FORMATION FLUID PRESSURE

Results indicating that flow dynamics are very sensitive towards borehole pressure alterations suggest that there might be high sensitivity towards initial fluid pressure inside the fracture. To investigate this effect, three simulations are run for horizontal fractures, using formation pressures of 15 MPa, 20 MPa (reference case) and 25 MPa. Other model parameters are kept the same as in the reference case. The borehole pressure was kept at 30 MPa in all cases.

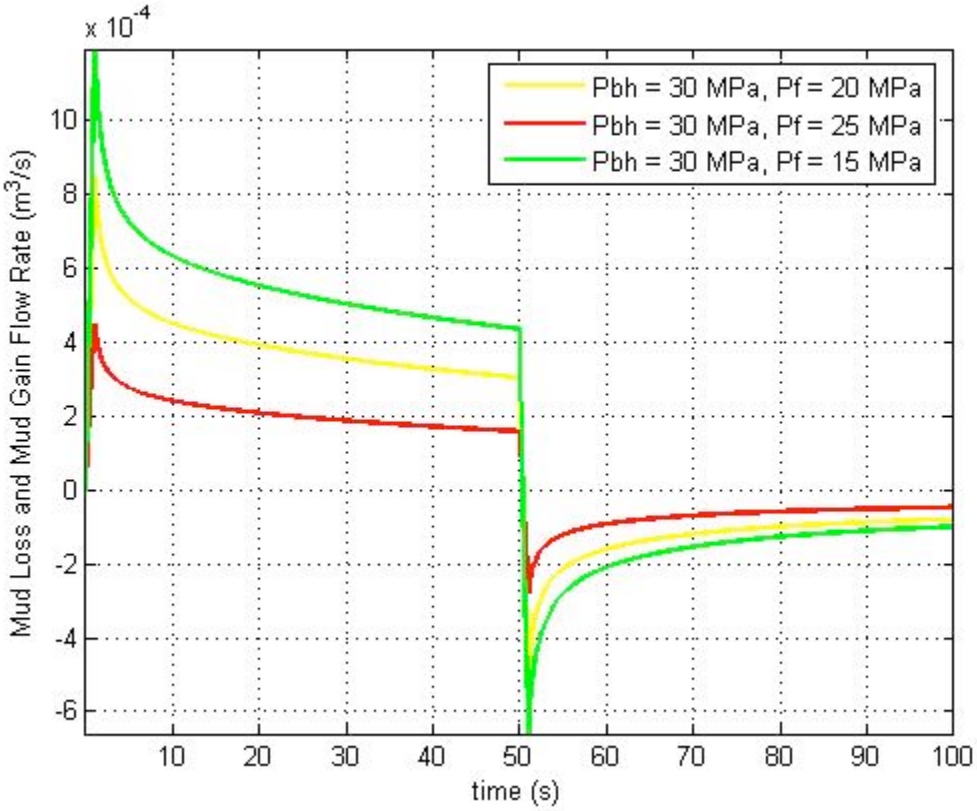

Figure 4-3: Effect of Initial Formation Pressure on the magnitude of borehole ballooning

As figure 4-3 shows, mud loss/gain quantity is quite sensitive to the initial fluid pressure within the fracture. Figure 4-3 indicates a remarkable difference between three cases. Increasing the initial formation fluid pressure noticeably decreases the flux. For a fracture with a lower initial formation pressure, the initial and mid simulation peaks are lower.

4.4 EFFECT OF OVERBALANCE PRESSURE

Increasing the initial formation fluid pressure has a similar effect to that of decreasing the borehole pressure: the mud loss/gain decreases. This points out that it is principally the magnitude of the overbalance (i.e., difference between the initial formation fluid pressure and the borehole pressure) which governs the fluid flow dynamics between the borehole and the fracture. This assumption is validated as shown in Figure 4-4, where results are presented for simulations with the same value of pressure difference between the initial fluid pressure and the borehole pressure. Results of mud loss/gain vs. time analyses at different overbalance pressure values are shown in Figure 4-4. Since the simulation results with the same differential pressure virtually coincide in Figure 4-4, the controlling factor on fluid flow dynamics is the magnitude of overbalance pressure rather than the absolute values of the pressures.

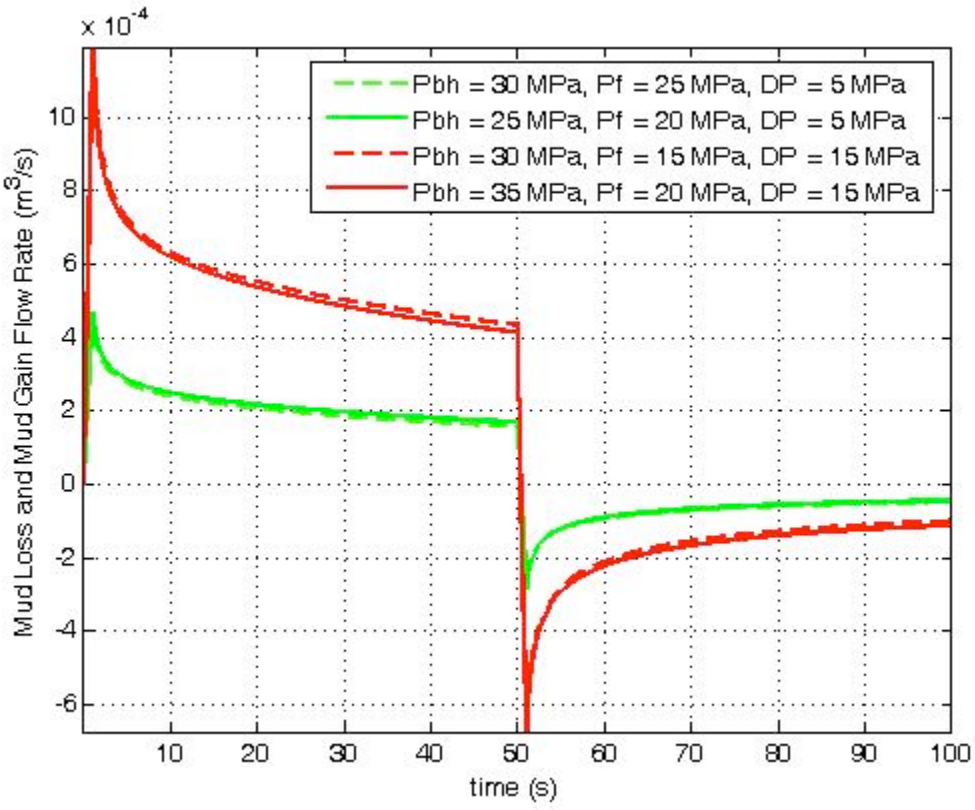

Figure 4-4: Effect of the pressure difference between the initial formation pressure and the borehole pressure on the magnitude of borehole ballooning

4.5 EFFECT OF WELL LOCATION

The effect of wellbore location with respect to the fracture boundaries on the magnitude of borehole ballooning has been investigated. Three simulations were run for a vertical borehole in the center, in the corner and in the edge of the horizontal fracture as shown in Figure 4-5. In these simulations, all parameters including fractures dimensions and the borehole cross-sectional area are kept constant. The results are illustrated in Figure 4-6.

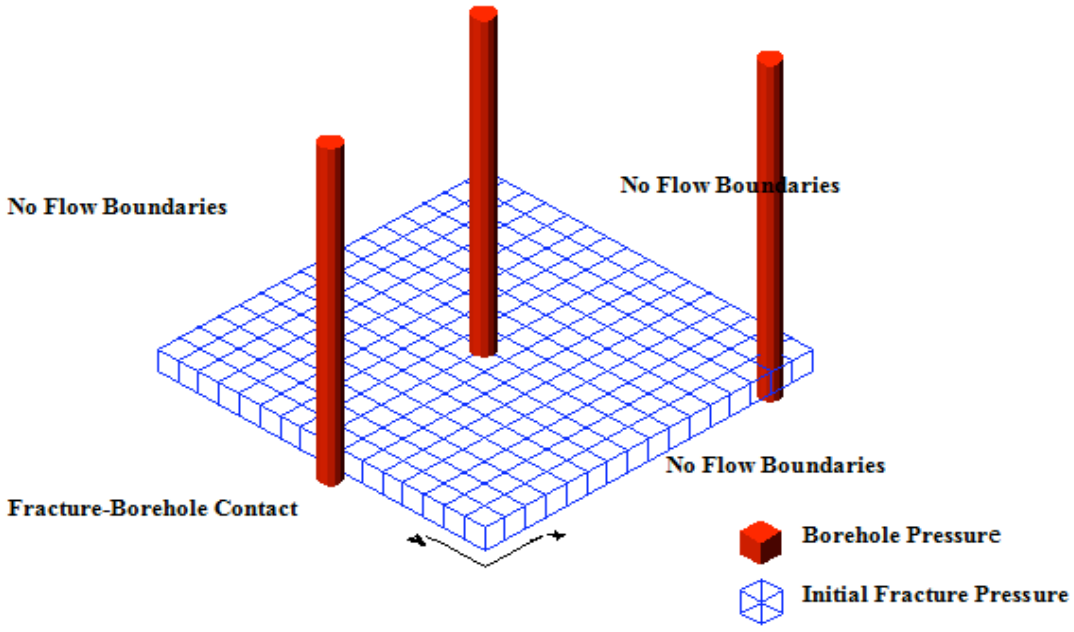

Figure 4-5: Schematic representation of different vertical wellbore locations

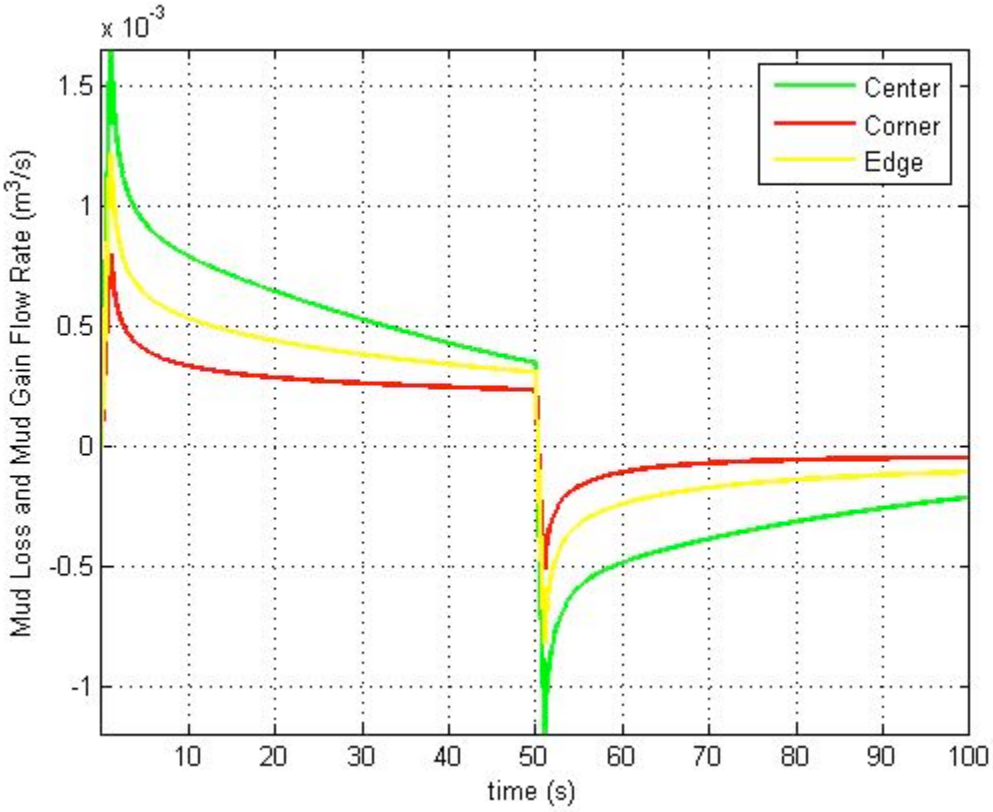

Figure 4-6: Effect of Wellbore Location on the magnitude of borehole ballooning

As shown in Figure 4-6, moving the well to the edge and to the corner consecutively reduces the initial and mid simulation peaks and increases the duration of the peak tails. The flow rate decreases at the faster rate when the borehole is located in the center of the fracture and decreases at the slower rate when the borehole is located at the periphery. This result implies that the borehole ballooning phenomenon might have more sever consequences when the borehole hits the fracture in the middle of the fracture than if the intersection point is located close to the fractures boundaries.

4.6 EFFECT OF FRACTURE LENGTH

All the simulations up to this part of this study were carried out for a 2D horizontal square shaped fracture with dimensions of 16mx16m. The effect of fracture length on the severity of mud loss/gain rate is examined by running three simulations for horizontal

fractures with different lengths. All the input data, except the length in the x direction, were kept constant for these simulations. Variable lengths were as follows:

(1) Lx = 16 m with 16 x-discretization steps of 1 m, Ly = 16 m

(2) Lx = 8 m with 8 x-discretization steps of 1 m, Ly = 16 m

(3) Lx = 4 m with 4 x-discretization steps of 1 m, Ly = 16 m

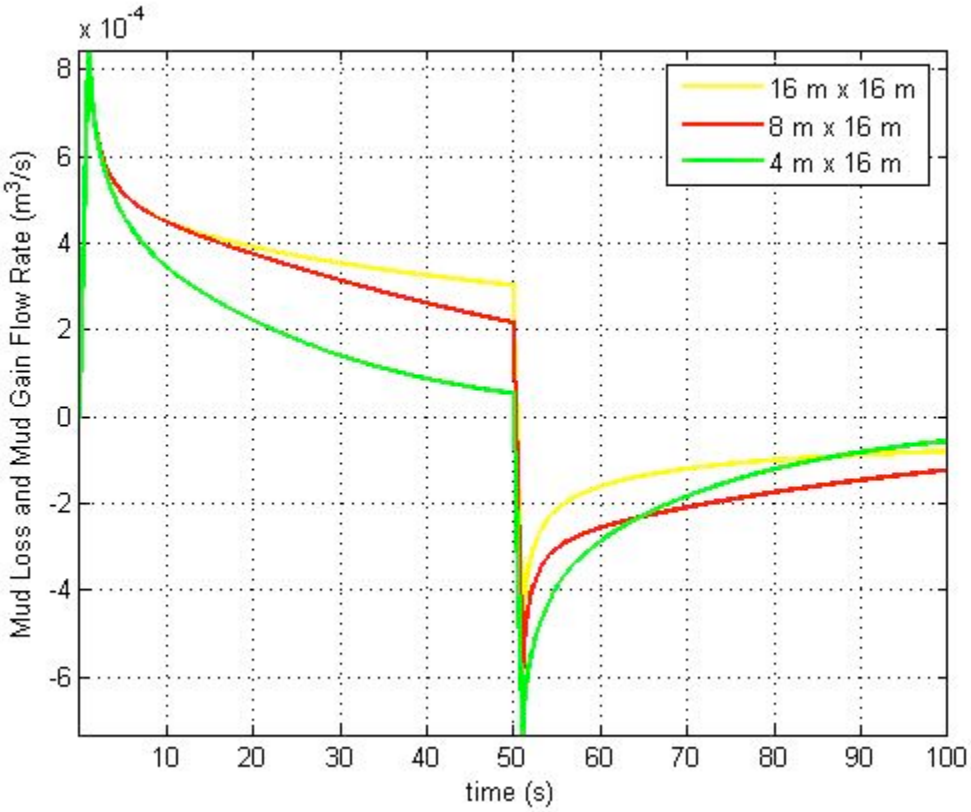

Figure 4-7: Effect of Fracture Length on the magnitude of borehole ballooning

As shown in Figure 4-7, the mud loss and gain rates peak at t=1s and at t =51s. It can be suggested that as the fracture length increases mud loss/gain rates slightly increase. It can be said that the fluid flow is not affected by the far end of the fracture at the initial stage. The fluid flow starts to be affected by the length of the fracture obviously after 5 seconds. However, in the case of a short fracture, the fluid loss/gain rate decays more rapidly and approaches eventually to zero. For a longer fracture, the charge and discharge of the drilling fluid last longer since it takes greater time for the pressure to come equilibrium along the fracture and the rate of fluid loss and gain is expected to be higher in a longer fracture.

4.7 EFFECT OF INITIAL FRACTURE APERTURE

The value of initial aperture was 1 mm in the reference case. Two simulations were run for fractures with initial aperture values of 1.1 mm and 0.9 mm and the results are compared in Figure 4-8.

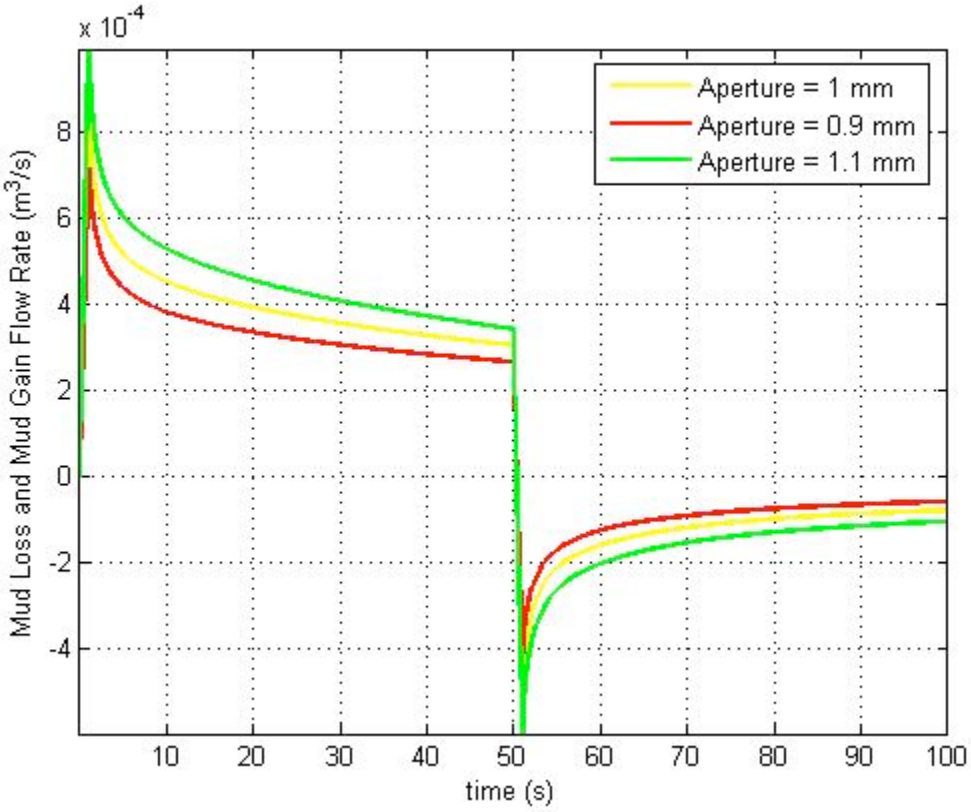

Figure 4-8: Effect of fracture aperture on the magnitude of borehole ballooning

As Figure 4-8 demonstrates, varying initial aperture changes the initial and mid simulation mud gain/loss peaks, but does not affect the decay rate. Mud flow dynamics are very sensitive to the aperture of the fractures encountered during drilling.

4.8 EFFECT OF SURFACE ROUGHNESS

Figure 4-9 demonstrates borehole ballooning phenomenon simulated in a square shaped fracture with the dimensions of 16m x 16m. Dashed lines represent the set “a” fracture aperture data with Hurst exponents varying from 0.4 to 0.9 and the solid lines correspond to the set “d” fracture aperture data. The only difference between these two fracture aperture sets is the different random number seeds used in the generation process. The simulation result for the ballooning event in a smooth fracture with 1 mm aperture is presented by solid reference line in the same plot. All simulations shown in Figure 4-9 were carried out by assuming fracture obeys the linear deformation law and all parameters except fracture roughness are constant. The average fracture asperity was taken as 1 mm in all simulations. Fracture surface roughness has a significant effect on the magnitude of mud gain/loss events. Fracture surface roughness and narrowing of the fracture surfaces caused by the smallest aperture sizes decrease the mud gain and loss flow rates.

Figure 4-10 is the close-up of Figure 4-9 and illustrates the mud loss and mud gain events in detail to show the effect of surface roughness more clearly. Solid yellow line (Ref) represents the borehole ballooning event in a 16m x16m fracture with smooth surfaces. Other solid lines represent the same event in “d” set fractures with rough surfaces having H exponent of 0.4 (red), 0.6 (green), and 0.9 (blue). Dashed lines illustrate mud gain/loss event in “a” set fractures which differentiate from “d” set fractures by their random number generation seed [H=0.4 (red), H=0.6 (green), and H=0.9 (blue)]. Rough fractures yielded lower values of fluid loss rate than smooth fractures even though they have the same average aperture. This figure also indicates that the rate differences between the two sets of data generated with different random number seeds is significant. This difference between the two sets can be explained by the random character of the width distribution, which might create a local heterogeneity within the fracture (Babadagli, 2005), and the different values of the width at the intersection point of the borehole. Note also that the set “a” possesses higher standard deviations than the ones of set “d”. Here, the solid lines correspond to the set “a” random number seed and fracture aperture data with Hurst

exponents varying from 0.4 to 0.9 having a mean value of 1 mm. The dashed lines represent the other random number set (set “d”) fracture aperture data.

Since the magnitude of borehole ballooning decreases as the aperture in rough fractures decreases, it can be proposed that higher standard deviation of random local width values leads to a diminishing effect on borehole ballooning. The effect of the degree of the roughness represented by the Hurst exponent (or fractal dimension) on borehole ballooning is shown in Figure 4-10. The difference follows the same trend and magnitude for the two data sets generated by two different random number seeds and cannot be assumed negligible.

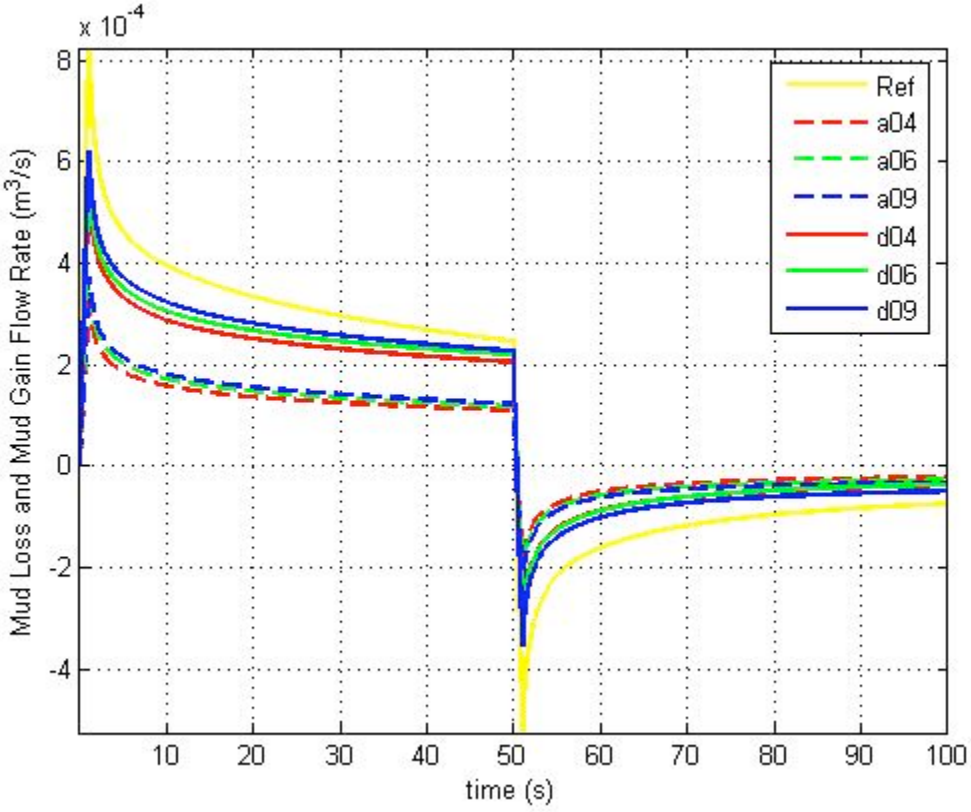

Figure 4-9: Effect of fracture surface roughness on the magnitude of borehole ballooning in case of the Linear Deformation Law

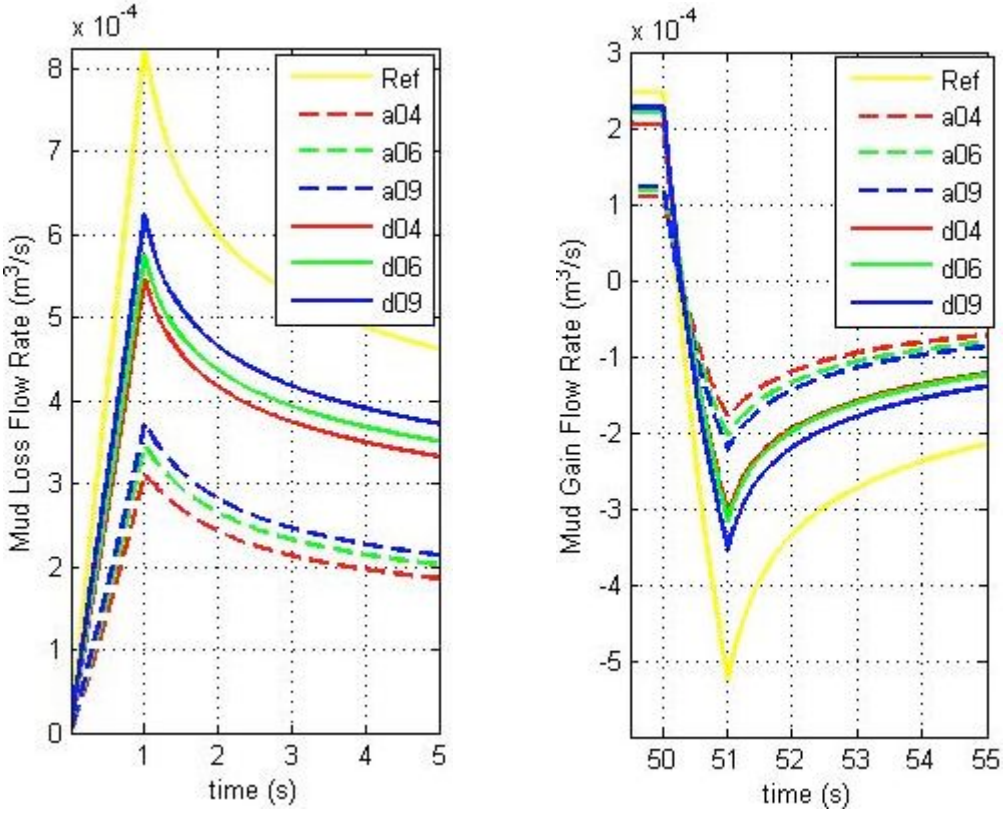

Figure 4-10: Effect of fracture surface roughness on the magnitude of borehole ballooning in case of the Linear Deformation Law

4.9 EFFECT OF FRACTURE GRID SIZE

It was mentioned before that the grid size selection for fracture aperture is a critical step. All the synthetic fractal data sets generated for this study were made available in 16x16, 32x32 and 64x64 grid sizes. Generally, it can be said that increasing the number of grids in any simulation will lead to more precise solutions. One should be extremely careful while working particularly with finite difference methods which have less computational stability.

Utilizing the data set with Hurst number, H=0.4, and random number seed “a” in the simulations, made it possible to observe a significant roughness effect on borehole ballooning. During the simulations, the fracture size was kept constant as 16m x 16m and only the grid sizes were changed. Set “a” random number generation seed with the Hurst

exponent of 0.4 is chosen to generate the data for the simulations, whereas for each simulation a different surface grid size is used [64x64 (green), 32x32 (yellow), and 16x16 (red)].The three curves shown in Figure 4-11 virtually coincide in the initial part, so the mud loss and gain flow rate peaks are not affected. However, there is a considerable difference between the orientations of the accompanying mud loss/gain rate tails. Results of the simulation carried out with 64x64 data have remarkably lower mud loss decay rate, which can be interpreted with the increasing accuracy of the input surface roughness data. A decrease in the fracture grid size number does not affect the initial and mid-simulation peaks but has a dramatic effect on the tail of the mud loss and mud gain flow rate versus time. These observations suggest that the scale used in data collection and/or generating fracture surfaces/apertures is a critical point.

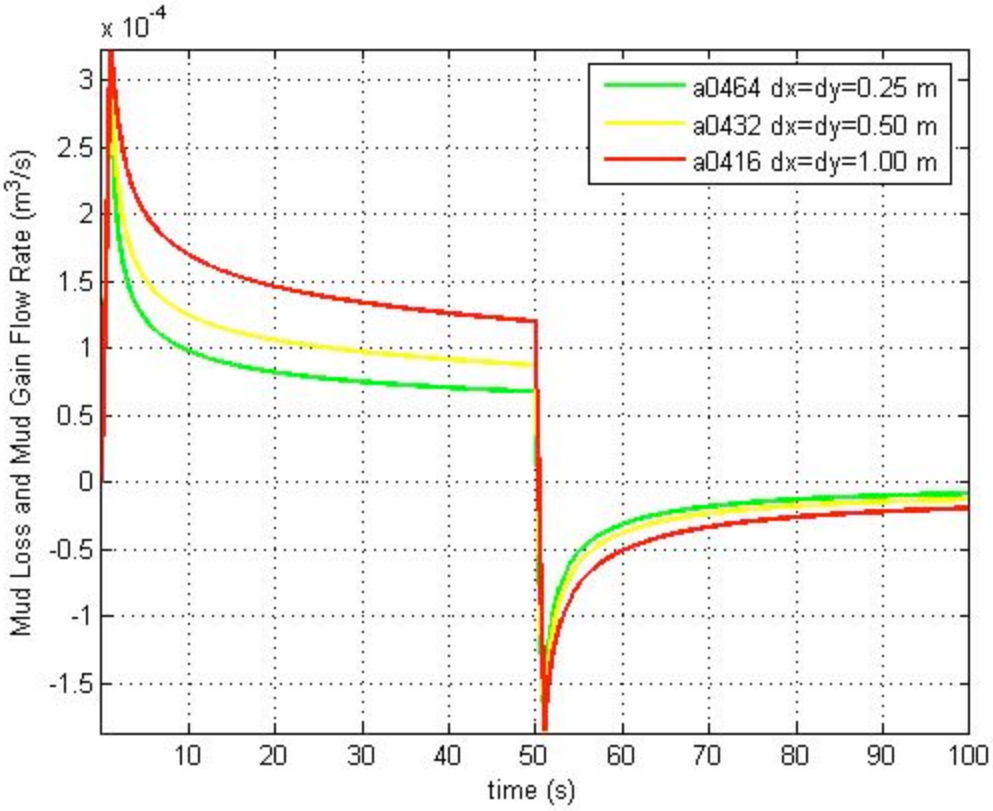

Figure 4-11: Effect of fracture grid size on the magnitude of borehole ballooning

.

4.10 EFFECT OF FRACTURE WIDTH

Most of the studies in the literature assumed that natural fractures have smooth surfaces. This could be a reasonable assumption as long as the fracture aperture is significantly larger than the dimensions of the roughness on the fracture surfaces. In order to clarify this issue, four different simulations were run and results shown in Figure 4-12. Mud loss/gain rates for rough and smooth walled fractures having 1 mm and 2 mm mean aperture values are shown in Figure 4-12. The dashed lines represent the fractures with rough surfaces and blue color is used to identify the fractures with 2 mm mean aperture. Smooth walled fractures are presented by solid curves. A 16x16 data set with H=0.4 and random number seed "a" was chosen in the simulation runs. Figure 4-12 demonstrates that increasing fracture aperture to twice of its original value diminishes the effects of fracture surface roughness on borehole ballooning. Within the aperture range we used (1-2 mm), the effect of roughness on ballooning process is still significant.

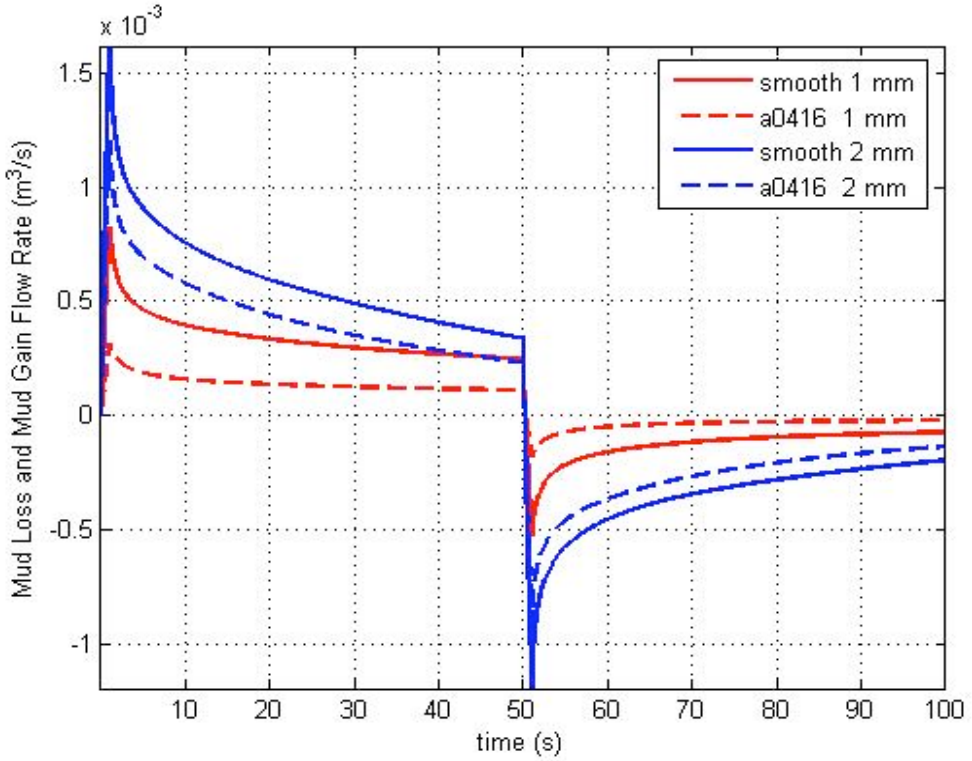

Figure 4-12: Effect of fracture width on the magnitude of borehole ballooning

4.11 EFFECT OF FLUID RHEOLOGY

In order to investigate the effect of mud rheology on the magnitude of borehole ballooning, four different simulations were run and comparison of mud loss/gain dynamics between Newtonian and Non-Newtonian mud rheologies is provided in Figure 4-13. Rheological properties of fluids are shown in Table 4.1. The yellow line represents Newtonian fluids loss/gain rates and it can be seen from Figure 4-13 that Newtonian fluid rheology causes highest mud loss/gain rates. All other fluid samples have Power Law rheology; however they have different mud loss/gain dynamics according to their rheological characterization. It can be seen from Figure 4-13 that the thickest fluid, represented with red line, has the lowest mud loss/gain rates. The thinner the fluid becomes, the higher mud loss/gain rates are observed. The Power Law fluid with thinnest rheology has almost the same mud loss/gain rates as the Newtonian fluid. It can be concluded from Figure 4-13 that fluid rheology has a remarkable effect on the magnitude of borehole ballooning; therefore choice of drilling fluid in areas with borehole ballooning problem should be made carefully.

Table 4-1: Rheological properties of fluids used for simulations in Section 4.11.

Fluid	n	K (cp)
Water	1	1
Very Thin Fluid	0.8	28
Thin Fluid	0.53	435
Thick Fluid	0.36	5326

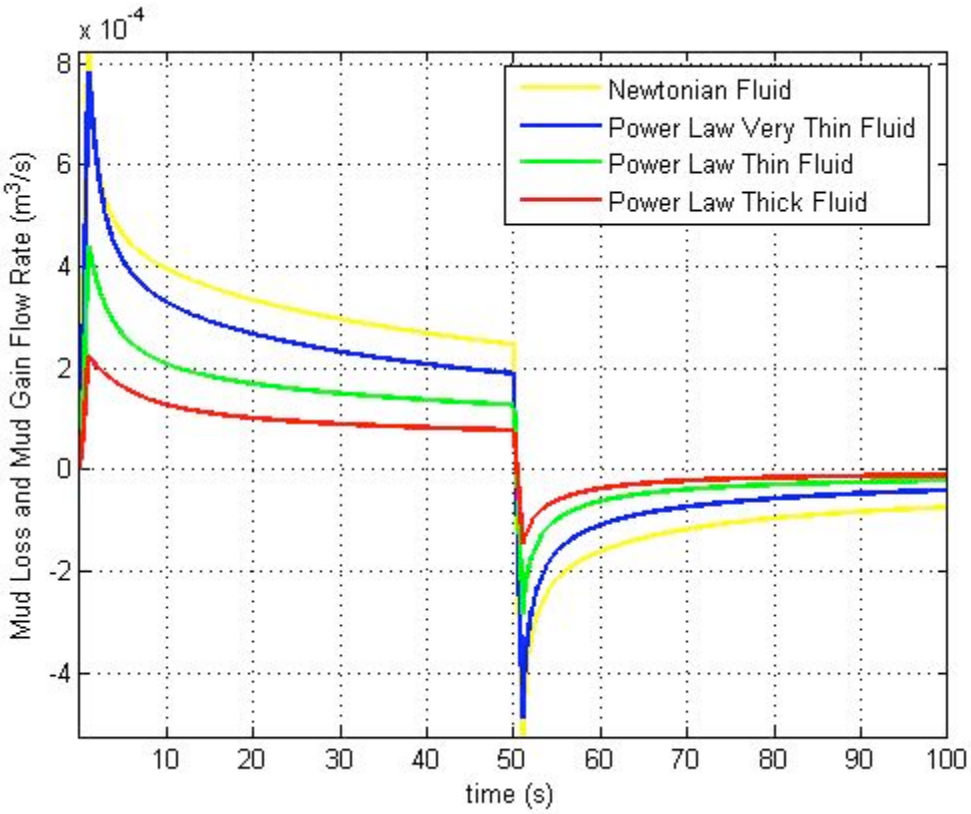

Figure 4-13: Effect of fluid rheology on the magnitude of borehole ballooning

CHAPTER 5 :EXPERIMENTAL PROGRAM

Flow in fractures, whether naturally occurring or drilling induced, is critical in the occurrence of borehole ballooning. In modeling of the fracture flow, it is important to know the surface characteristics of the fractures, the rheology of the flowing fluid, and the pressure values causing the fluid flow within the fracture. This part of the research was devoted to an experimental study of borehole ballooning and effects of operational parameters, lithology and surface roughness of the fractures on the magnitude of borehole ballooning.

5.1 MATERIALS USED FOR EXPERIMENTS

5.1.1 Description of Rock Samples

Limestone, sandstone and granite core samples were used in the experiments. The cylindrical cores were 3 inches in length and 1 inch in diameter. To analyze the effect of fracture surface roughness on ballooning, two different fracture types were generated. Core samples were cut half by a steel blade to generate smooth fracture surface. The space between the two halves of the core samples formed the fracture (Figure 5-1). For rough surface fractures, one complete core sample from each lithology was placed longitudinally on a wedge and then the wedge is placed under a testing machine. Axial load was applied on each sample until a fast propagating fracture divided the core in two (Figure 5-2).

Figure 5-1: Core samples with smooth fracture surfaces. From left to right: sandstone, granite and limestone

Figure 5-2: Core samples with rough fracture surfaces. From left to right: sandstone, granite and limestone

5.1.2 Description and Characterization of Fluid Samples

Water (Newtonian fluid) was first used as a test fluid. Most of drilling fluids have Non-Newtonian fluid rheology. Therefore, to investigate the effect of fluid rheology on the magnitude of borehole ballooning experimentally, aqueous polymer solutions (Power Law fluid) with two different Xanthan Gum concentrations were used for further experiments. Aqueous polymer solutions with 1 lb/bbl and 3 lb/bbl concentrations were prepared to use as thin and thick fluids for these experiments.

Xanthan gum, an exocellular heteropolysaccharide produced in fermentation by bacteria (Xanthomonas campestris), is a cream-colored powder that dissolves in water to produce solutions with high viscosity at low concentration (Fischer, et al. 2001). Xanthan gum has relatively stable viscosity properties as a function of salt concentration, pH, temperature and shear degradation (Salamone et al., 1982).

Xanthan gum's high viscosifying ability, coupled with excellent stability under high salinity, high temperature, and mechanical shear conditions makes the use of xanthan gum favorable for various drilling, drill-in, completion, fracturing and even in enhanced oil recovery (EOR) operations in the oil field (Salamone et al., 1982; Beck et al., 1993; Li et al., 1999; Fischer, et al. 2001)

Performing rheological characterization of aqueous polymer solutions was essential since flow consistency index (K) and flow behaviour index (n) are needed as input parameters for numerical modeling of borehole ballooning phenomenon. Bohlin C-VOR cone and plate type rheometer is used to obtain shear stress vs. shear rate values of polymer solutions. Figures 5.3 and 5.4 show the rheological behavior of the samples. Power law model was found to be applicable for describing the flow behaviour of polymer solutions used in this study. Power law model constants (K, n) of sample solutions were calculated by curve fitting the experimental data. Table 5-1 summarizes rheological properties of polymer solutions.

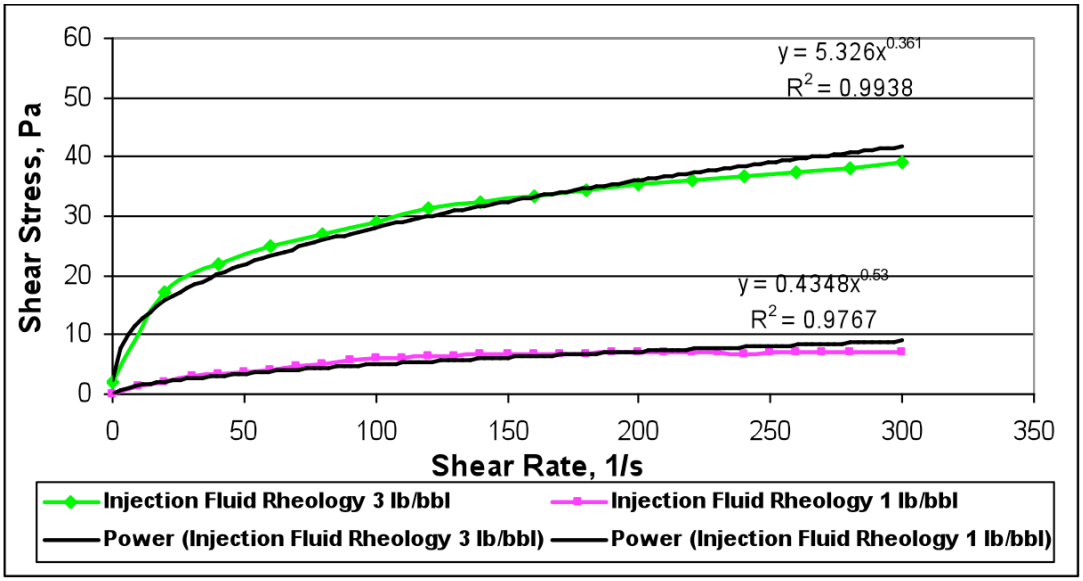

Figure 5-3: Rheological characterization of Aqueous – polymer solutions

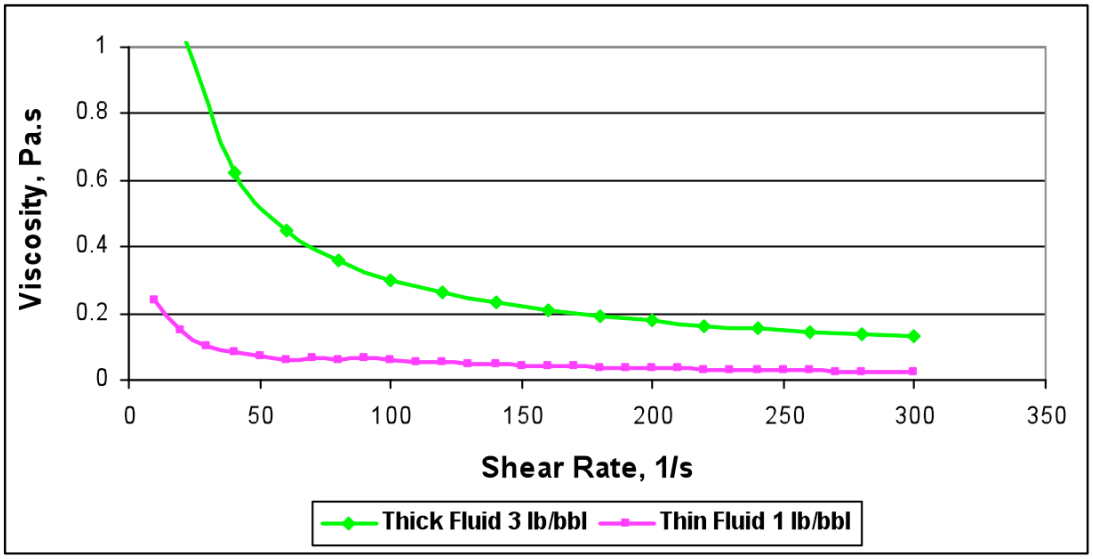

Figure 5-4: Viscosity vs. shear rate values of Aqueous – polymer solutions

Table 5-1: Rheological properties of Aqueous – polymer solutions

Fluid	n	K (cp)
Water	1	1
Thin Fluid	0.53	435
Thick Fluid	0.36	5326

5.2 EXPERIMENTAL SETUP

The laboratory setup used for borehole ballooning experiments is shown in Figure 5.5. It consists of two ISCO 500D Syringe Pumps, one Hassler type steel coreholder with a rubber sleeve, a control panel to operate the pumps manually and a PC for data acquisition.

ISCO pumps, connected to the coreholder to transfer fluids at desired flow rate and pressure The pump can deliver flow rates up to 200 ml/min at pressures up to 3,750 psi. One of the pumps is used to develop a confining pressure through the annulus between the rubber sleeve and the coreholder, while the other is utilized to simulate the changing borehole pressure.

As shown in Figure 5.5, the centerpiece of the apparatus is a Hassler-type stainless steel coreholder with rubber sleeve inside. The confining pressure is provided by pressurizing the annulus between the sleeve and steel body. A pressure gauge is mounted on the annulus pressure line to monitor the applied confining pressure. The pumps are connected to the computer by a main controller. The Labview software of National Instruments is used to record all the data obtained from the experiments.

Figure 5-5: The laboratory setup for borehole ballooning experiments

5.3 EXPERIMENTAL PROCEDURE

To analyze the effect of fracture surface roughness on ballooning, two different fracture types were generated; rough and smooth. The fractured core samples were first kept in an oven at 100º C for a period of 3 hours and then vacuum-saturated with the test fluid for a period of 6 hours. Saturating the cores with test fluids was essential in order to minimize the matrix fracture transfer and increase the dominating effect of the fracture on the fluid flow. Following the vacuum saturation of the cores, each sample was placed in a rubber sleeve and inserted into the Hassler coreholder maintained in a horizontal position.

The confining pressure was kept at 100 psi in all of the experiments, except the ones where the effect of confining pressure is investigated. The confining pressure was used to simulate the initial pressure within the fracture. By pressurizing the core sample along the outer diameter, two core halves were kept together, i.e., the fracture was closed. The second pump was connected to the inlet of the coreholder. The outlet of the Hassler core holder was kept closed to build an experimental condition simulating the borehole ballooning phenomenon.

Initially both confining pressure and injection pressure were set at 100 psi, simulating the bottomhole pressure under no circulation condition. To mimic the intersection of a single horizontal fracture while drilling with bottomhole pressure higher than the formation pressure, fluid injection pressure was increased up to 200 psi. At the final stage of the experiment, fluid injection pressure was reduced again to its initial value of 100 psi to simulate the no circulation condition.

By increasing or decreasing the injection pressure while keeping the confining pressure constant, a combined flow from the pump into the coreholder (mud loss) and reverse flow from the coreholder into the pump (mud gain) were observed. The test fluid was pumped into the fracture by increasing the injection pressure to 200 psi and gained back by lowering the pressure back to the level of 100 psi equal to the confining pressure.

Water (Newtonian fluid) was used as the first test fluid. To investigate the effect of fluid rheology on the magnitude of borehole ballooning, aqueous polymer solutions (Power Law fluid) with 1 lb/bbl and 3 lb/bbl polymer concentrations (representing thin and thick fluids) were injected following the water experiments.

CHAPTER 6 : EXPERIMENTAL RESULTS AND DISCUSSIONS

6.1 BOREHOLE BALLOONING EXPERIMENTS PERFORMED WITH WATER

Results of borehole ballooning experiments conducted by using water (Newtonian fluid) are presented in this section.

6.1.1 Effect of Fracture Surface Roughness

Figures 6-1, 6-3 and 6-5 demonstrate effect of rock surface roughness on the rate of mud loss/gain in fractured sandstone, limestone and granite samples, respectively. The results of these experiments suggest that fracture surface roughness has a noticeable effect on the magnitude of mud loss/gain rate. Generally, rough fractures yield lower values of fluid loss loss/gain rate than smooth fractures.

Figures 6-2, 6-4, and 6-6 show cumulative volume of mud loss/gain into fractured sandstone, limestone, and granite, respectively. Cumulative mud loss is higher in core samples with smooth fracture surfaces.

One of the main assumptions of this study is that the roughness size (height) is not negligible in comparison to fracture width. Therefore, any consideration of the roughness will reduce the area open for flow. Fluid loss/gain values observed in the experiments are controlled by the effective area open to flow, which is directly related to the degree of roughness.

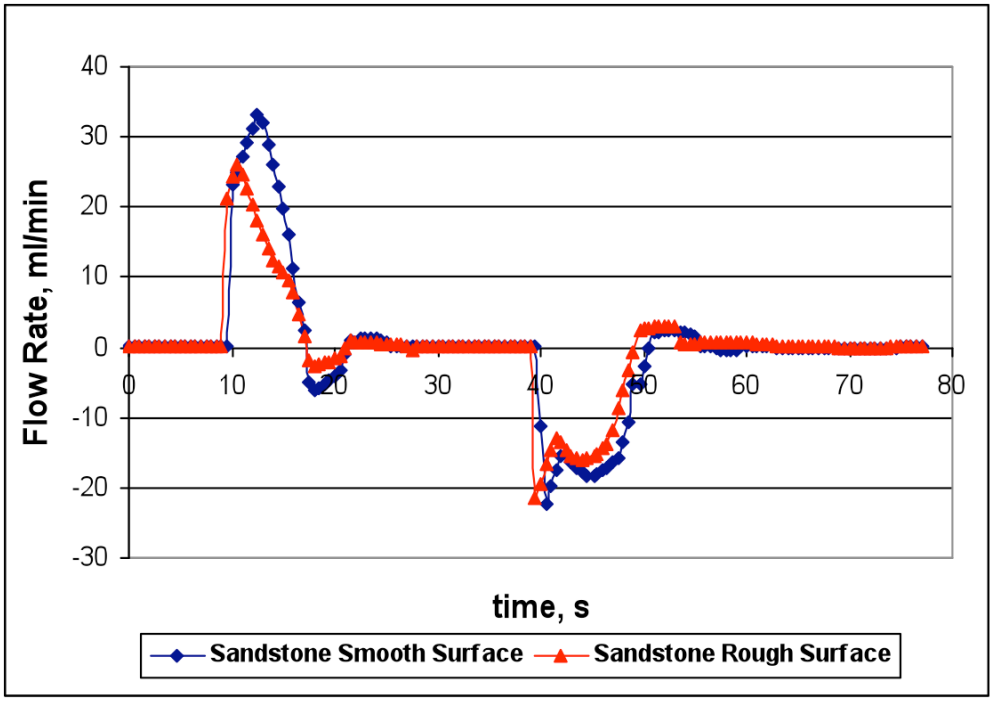

Figure 6-1: Effect of fracture surface roughness on the mud loss/gain rate in fractured sandstone cores

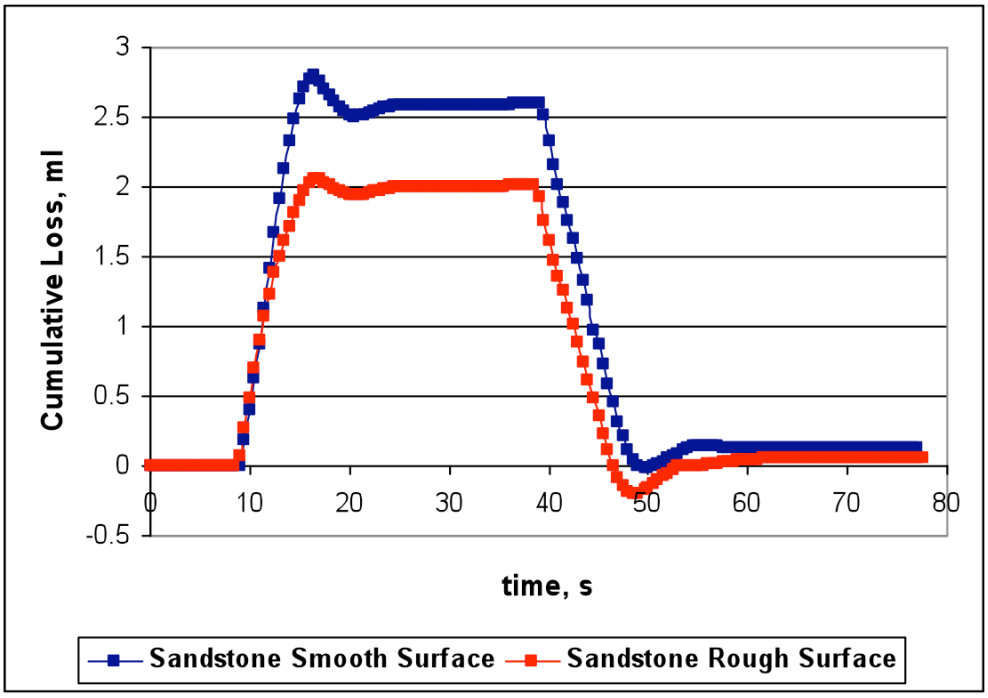

Figure 6-2: Effect of fracture surface roughness on the cumulative mud loss in fractured sandstone cores

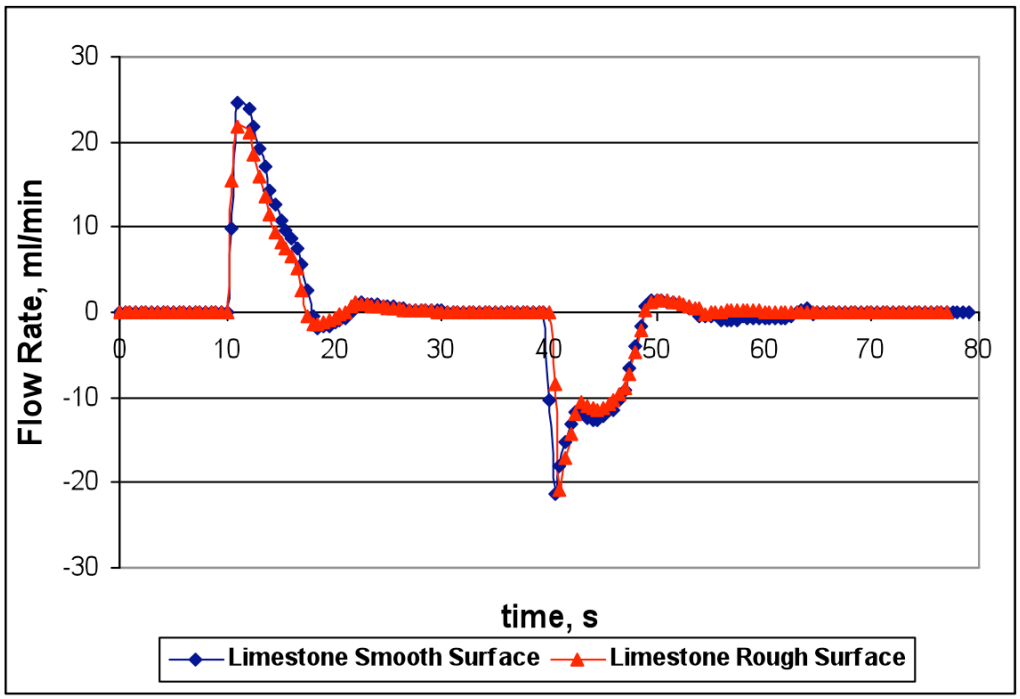

Figure 6-3: Effect of fracture surface roughness on the mud loss/gain rate in fractured limestone cores

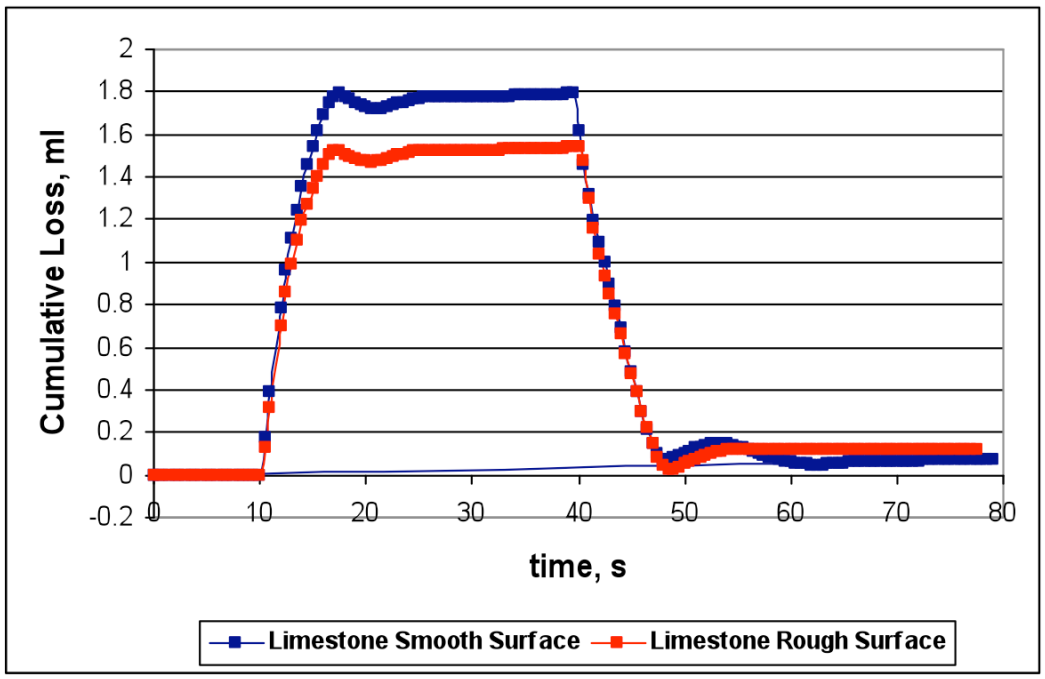

Figure 6-4: Effect of fracture surface roughness on the cumulative mud loss in fractured limestone cores

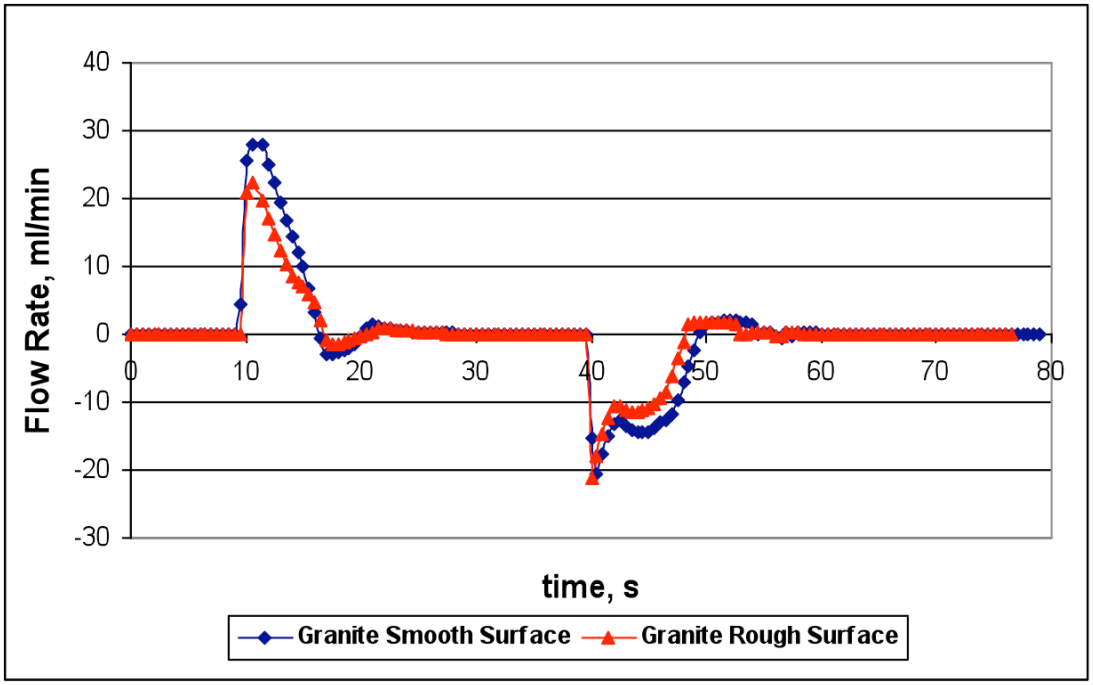

Figure 6-5: Effect of fracture surface roughness on the mud loss/gain rate in fractured granite cores

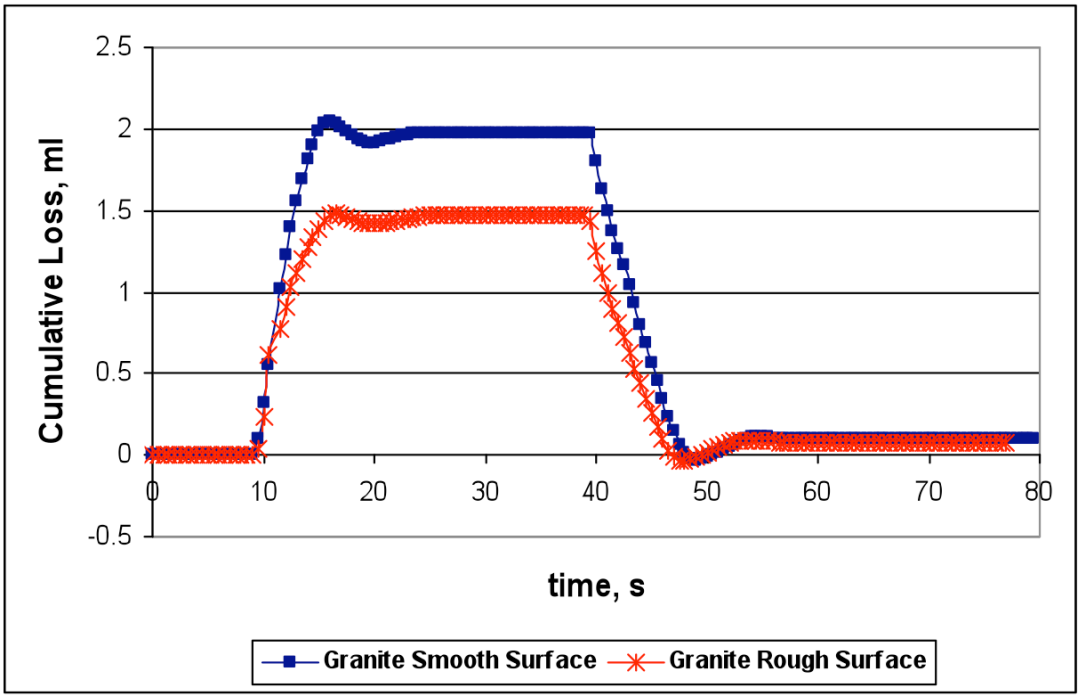

Figure 6-6: Effect of fracture surface roughness on the cumulative mud loss in fractured granite cores

6.1.2 Effect of Rock Type

Figure 6-7 provides comparisons of mud loss and gain rates in smooth surface fractures of sandstone, limestone and granite core samples. Core samples were 100% saturated with the test fluid before the experiment to make sure that there is no fluid invasion into the rock matrix. Therefore, any difference in fluid volume loss/gain can be attributed to the relative surface roughness of the rock under investigation. The peak mud loss and gain rate is observed in the sandstone sample. Figure 6-8 shows the cumulative mud loss/gain values observed in sandstone, limestone and granite core samples with smooth surface. Higher cumulative mud loss/gain was recorded in the sandstone sample.

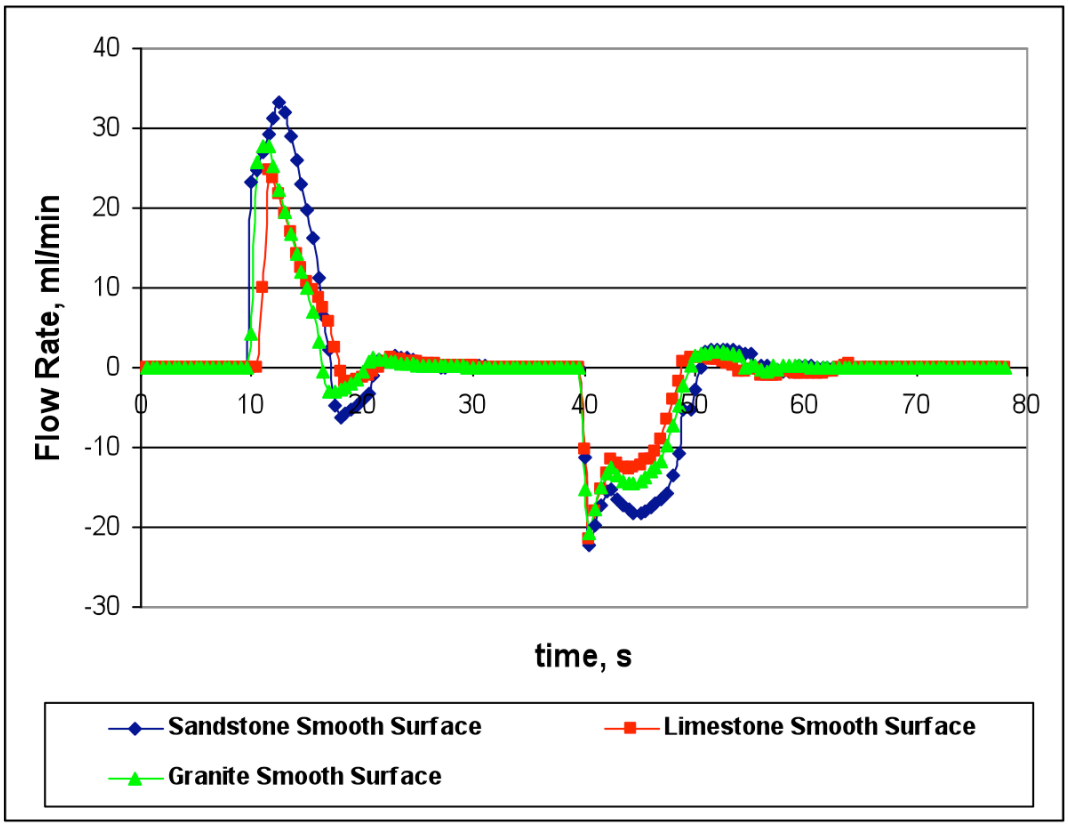

Figure 6-7: Effect of rock type on the mud loss/gain rates in samples with smooth fracture surfaces

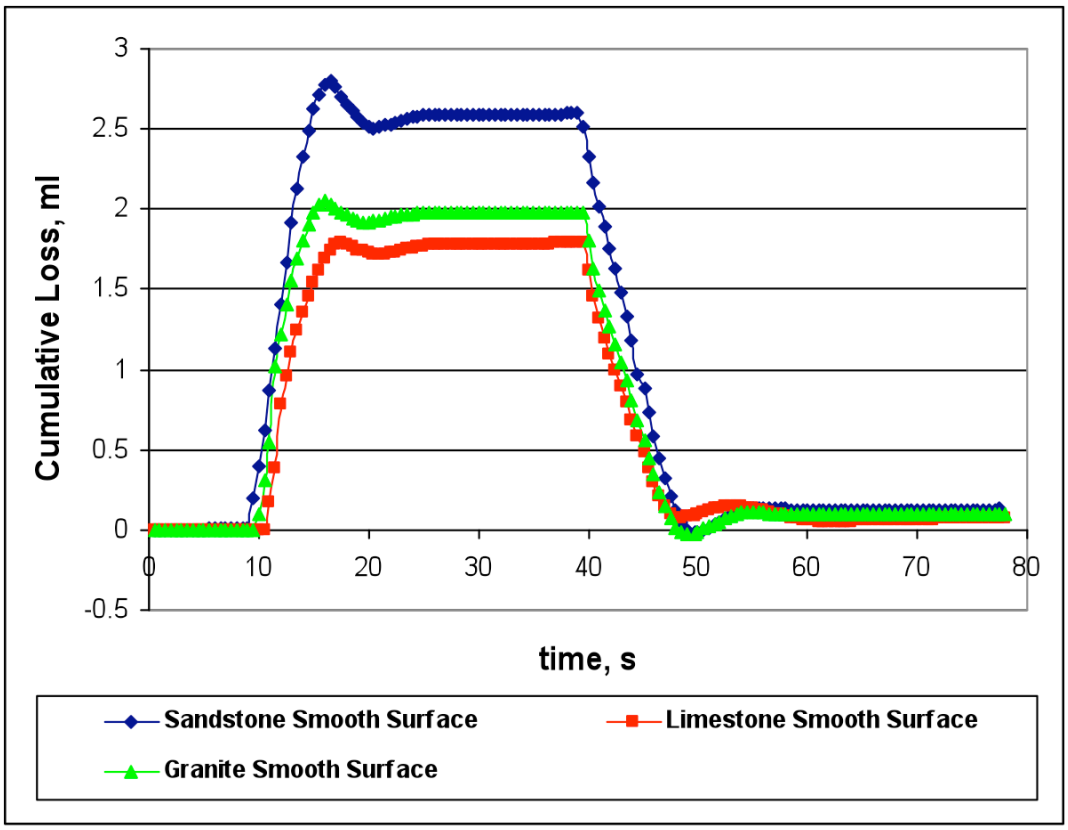

Figure 6-8: Effect of rock type on the cumulative mud loss in samples with smooth fracture surfaces

The rate of mud loss/gain and cumulative mud loss/gain amounts observed in the core samples with rough surfaces are presented in Figures 6-9 and 6-10, respectively. The highest cumulative mud loss/gain value was again obtained in the sandstone sample. Limestone and granite core samples showed very similar flow rate and cumulative loss results. The higher mud loss/gain values obtained in sandstone sample can be attributed to the fact that sandstone sample might have lower surface roughness.

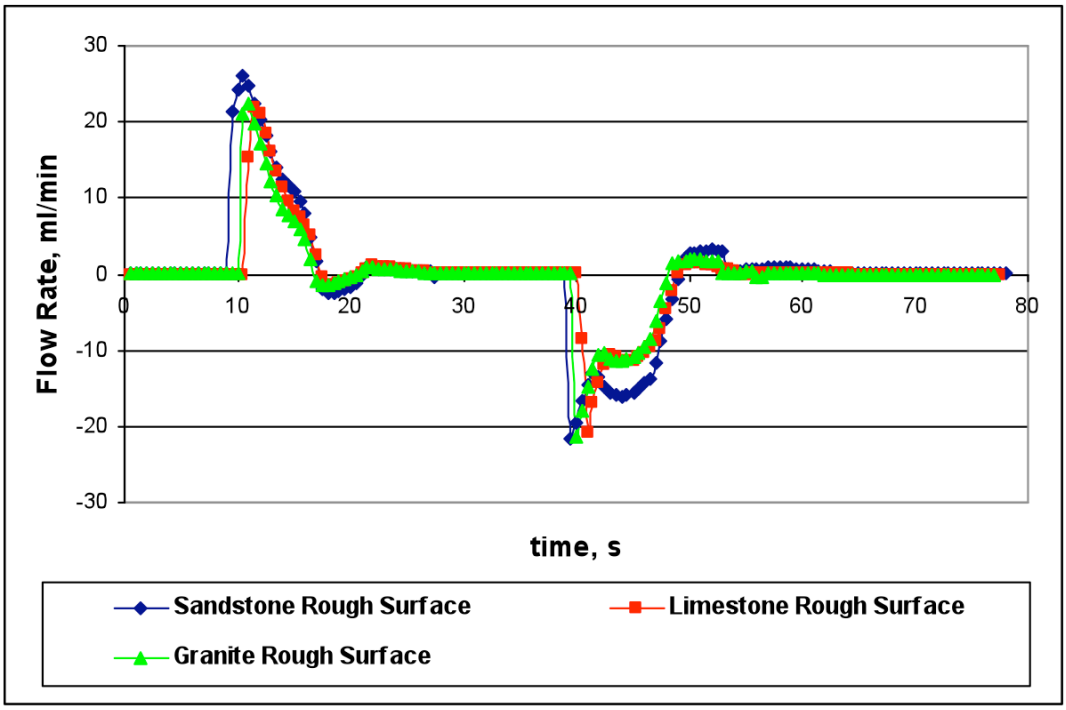

Figure 6-9: Effect of rock type on the mud loss/gain rates in samples with rough fracture surfaces

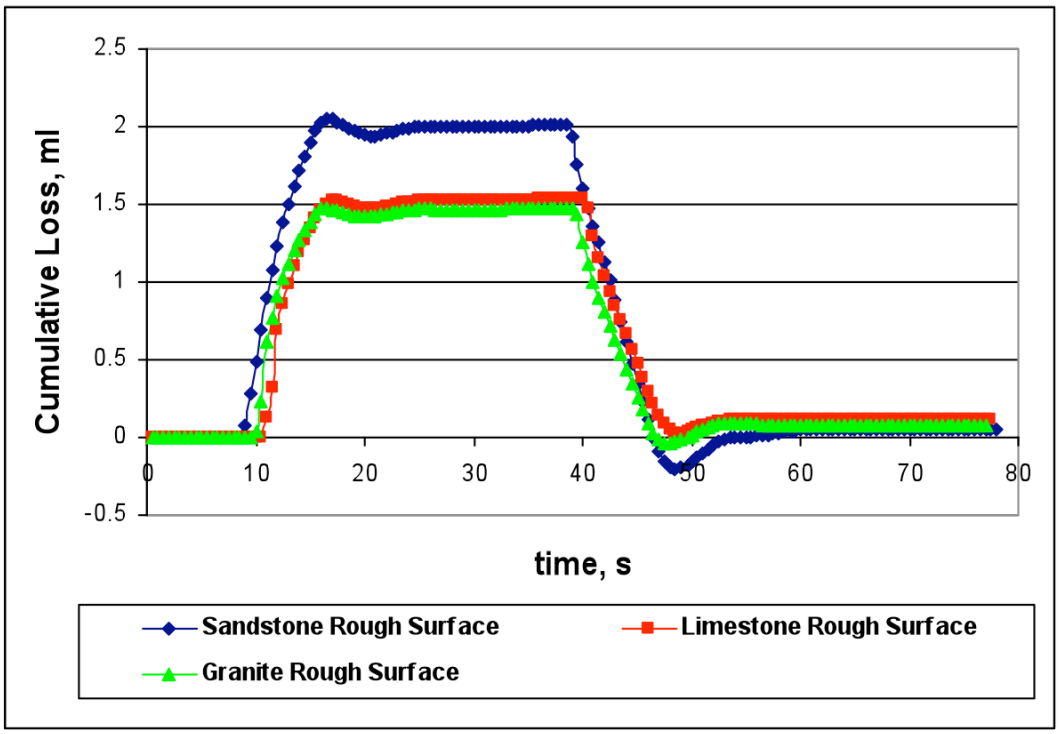

Figure 6-10: Effect of rock type on the cumulative mud loss in samples with rough fracture surfaces

6.1.3 Effect of Injection (Borehole) Pressure

Experiments have been carried out with smooth and rough fracture sandstone samples, where the injection pressure is increased from 100 psi to 150 psi, 200 psi and 250 psi at the tenth second of each experiment and decreased back to 100 psi after 40 seconds of mud injection. Figures 6-11 and 6-13 demonstrate the effects of injection pressure (borehole pressure) on the rate of mud loss/gain into fractured sandstone samples with smooth and rough surfaces, respectively.

Figures 6-12 and 6-14 show the effects of injection pressure (borehole pressure) on the cumulative mud loss/gain in the fractured sandstone samples with smooth and rough surfaces, respectively.

The results showed that increasing the borehole (injection) pressure increased the mud loss/gain rates and the cumulative loss considerably. In other words, the mud loss/gain dynamics are very sensitive to well pressure variations.

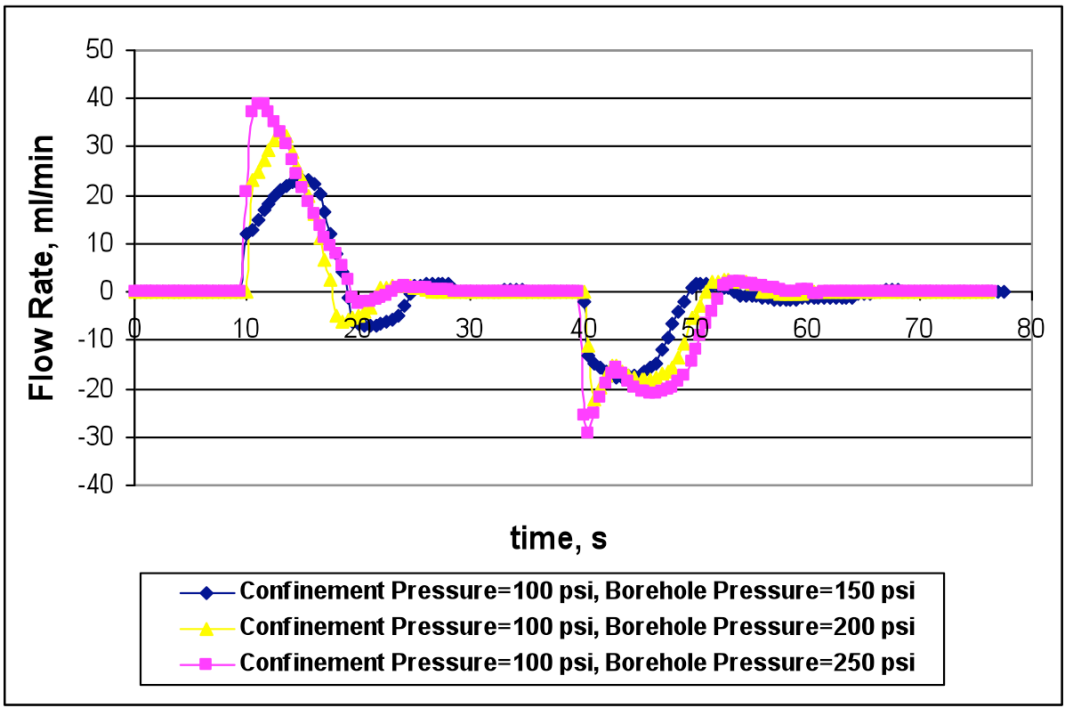

Figure 6-11: Effect of borehole pressure (injection pressure) on the mud loss/gain rate in sandstone cores with smooth fracture surface

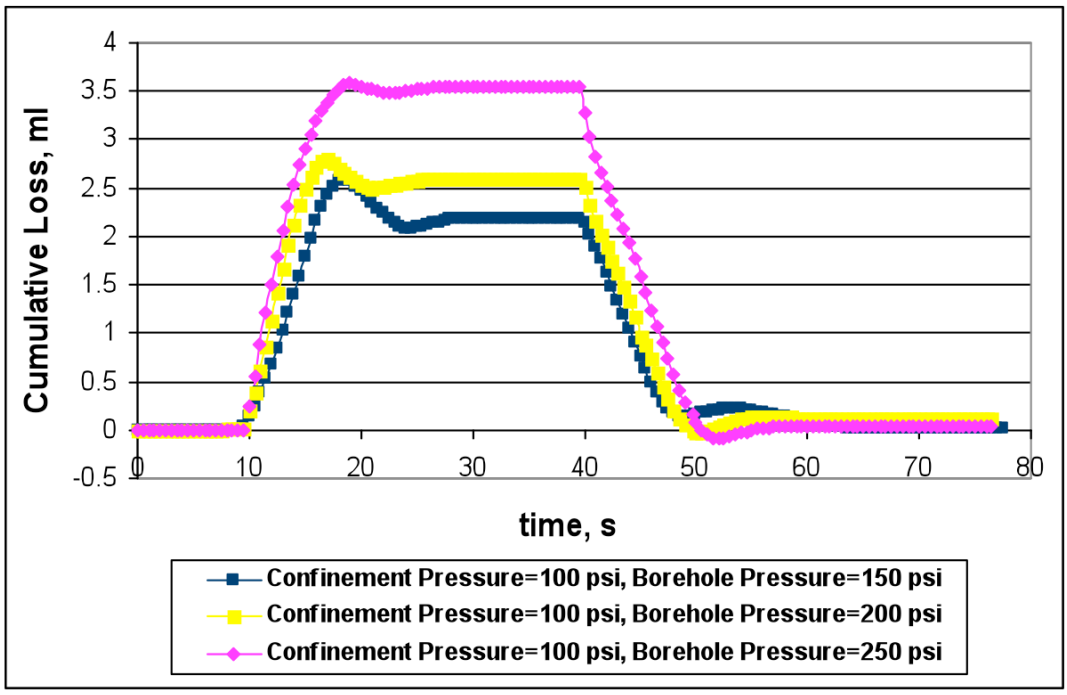

Figure 6-12: Effect of borehole pressure (injection pressure) on the cumulative mud loss in sandstone cores with smooth fracture surfaces

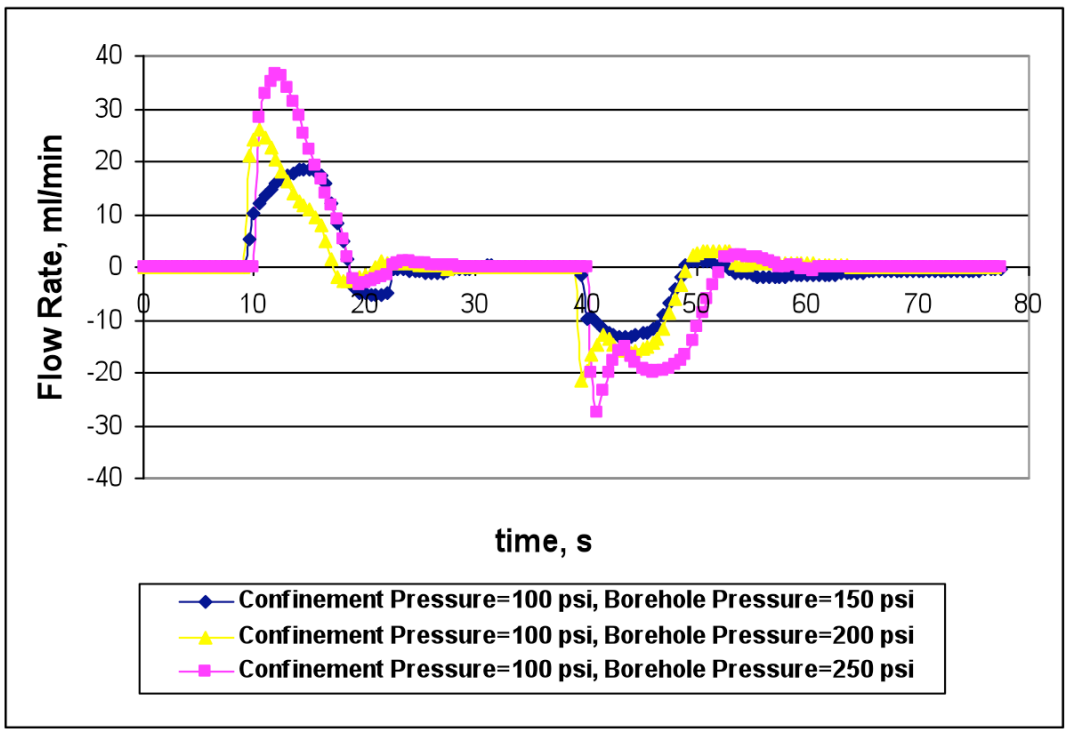

Figure 6-13: Effect of borehole pressure (injection pressure) on the mud loss/gain rate in sandstone cores with rough fracture surfaces

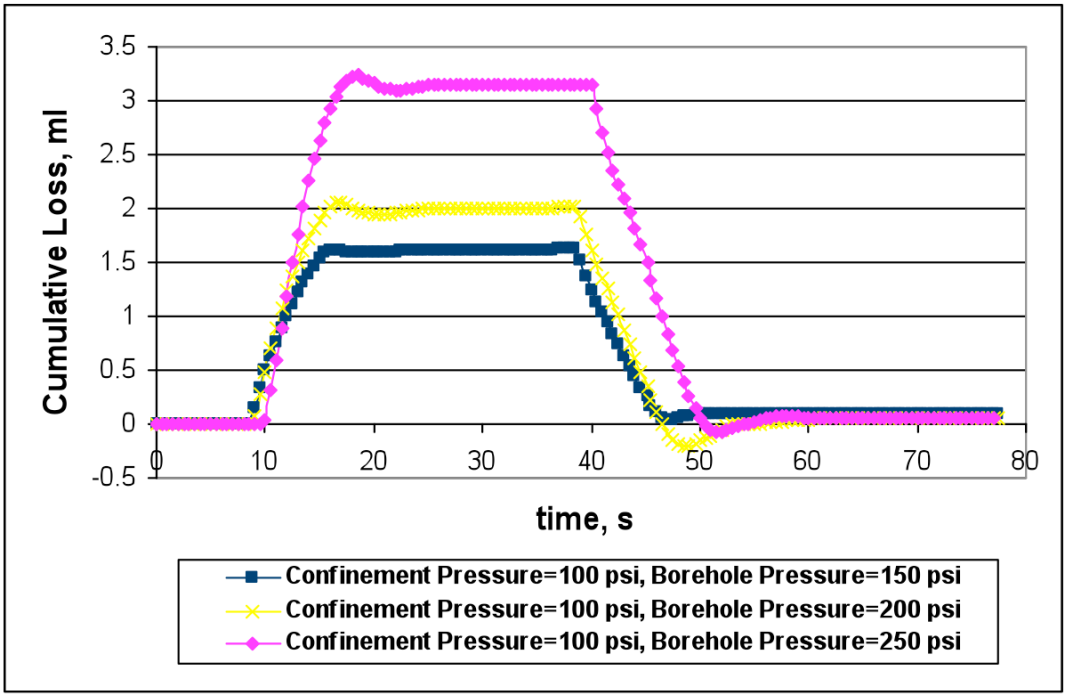

Figure 6-14: Effect of borehole pressure (injection pressure) on the cumulative mud loss in sandstone cores with rough fracture surfaces

6.1.4 Effect of Initial Pressure within the Fracture

Generally, confining pressure is applied to the samples in order to simulate the effect of initial pressure within the fracture. Experiments were performed in smooth and rough fracture sandstone samples, where the confining pressure is kept constant at 50 psi, 100 psi and 150 psi. In each experiment, the injection pressure is increased from the confining pressure level to 200 psi shortly after the beginning of the experiment and decreased back to the confining pressure at the end of the experiment.

As shown in Figures 6-15 to 6-18, mud loss/gain rates (Figs. 6-15 and 6-17) and cumulative mud loss/gain volumes (Figs. 6-16 and 6-18) are very sensitive to the initial pressure within the fracture. Overall, increasing the confinement pressure has an effect of that of decreasing the injection pressure: the mud loss/gain decreases. The effect of fracture surface roughness on borehole ballooning, however, still shows its significance as seen from the comparisons of the Figures 6-15 and 6-17 and 6-16 and 6-18.

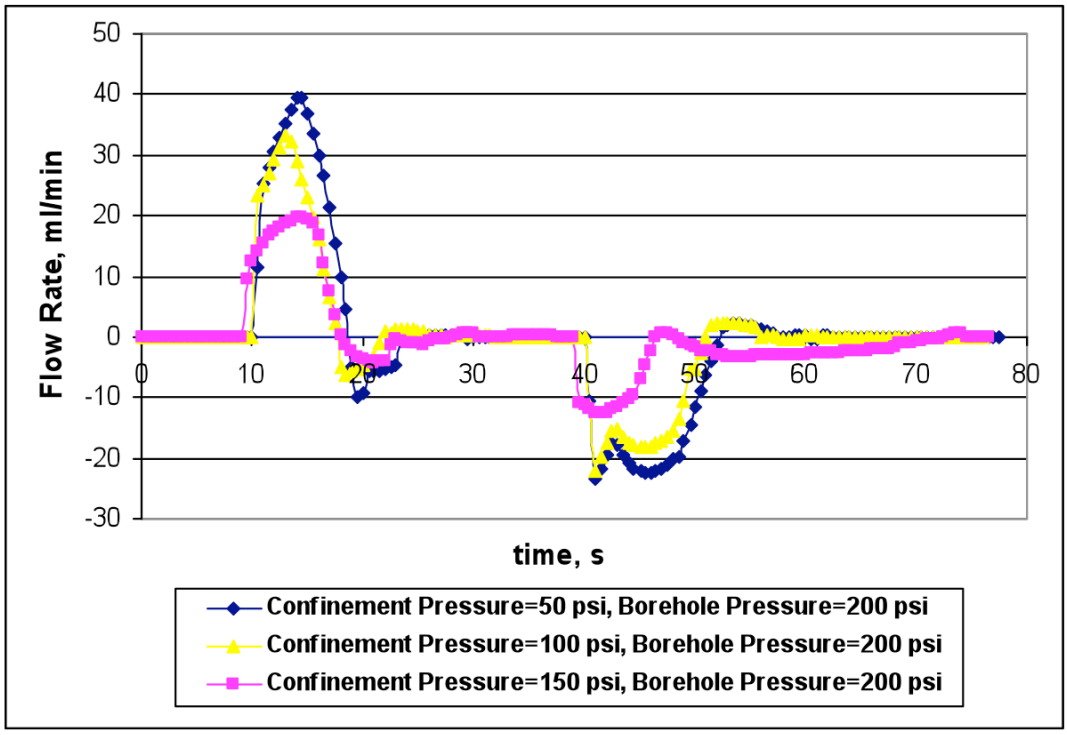

Figure 6-15: Effect of initial pressure in the fracture (confining pressure) on the mud loss/gain rate in sandstone cores with smooth fracture surfaces

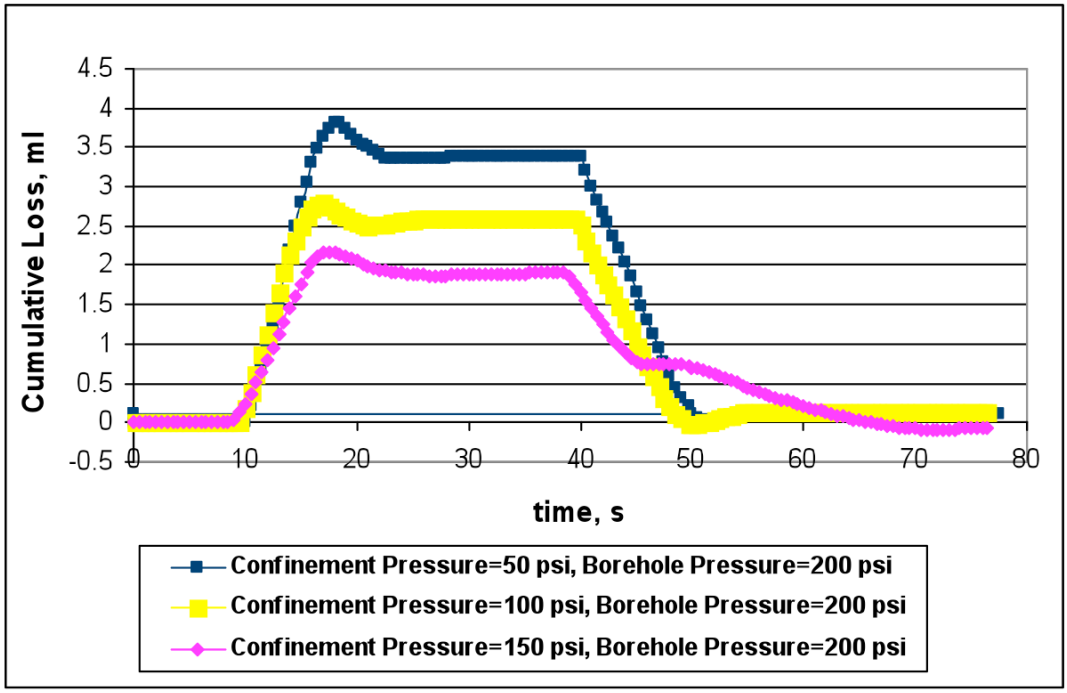

Figure 6-16: Effect of initial pressure in the fracture (confining pressure) on the cumulative mud loss in sandstone cores with smooth fracture surfaces

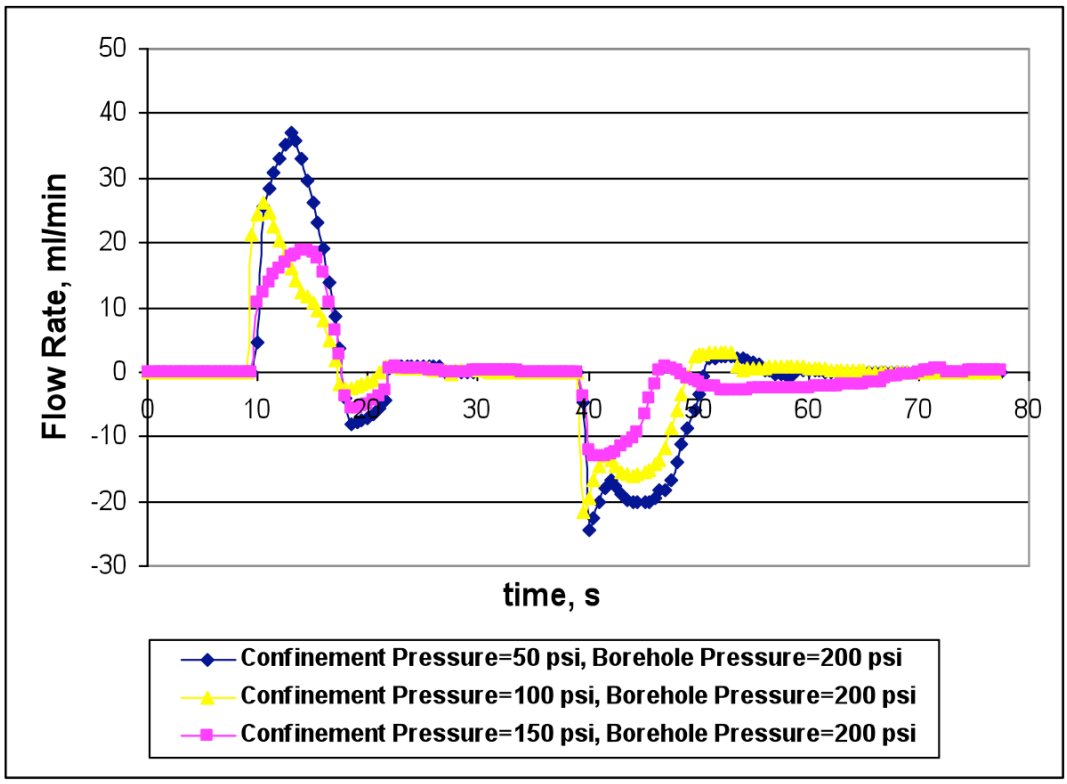

Figure 6-17: Effect of initial pressure in the fracture (confining pressure) on the mud loss/gain rate in sandstone cores with rough fracture surfaces

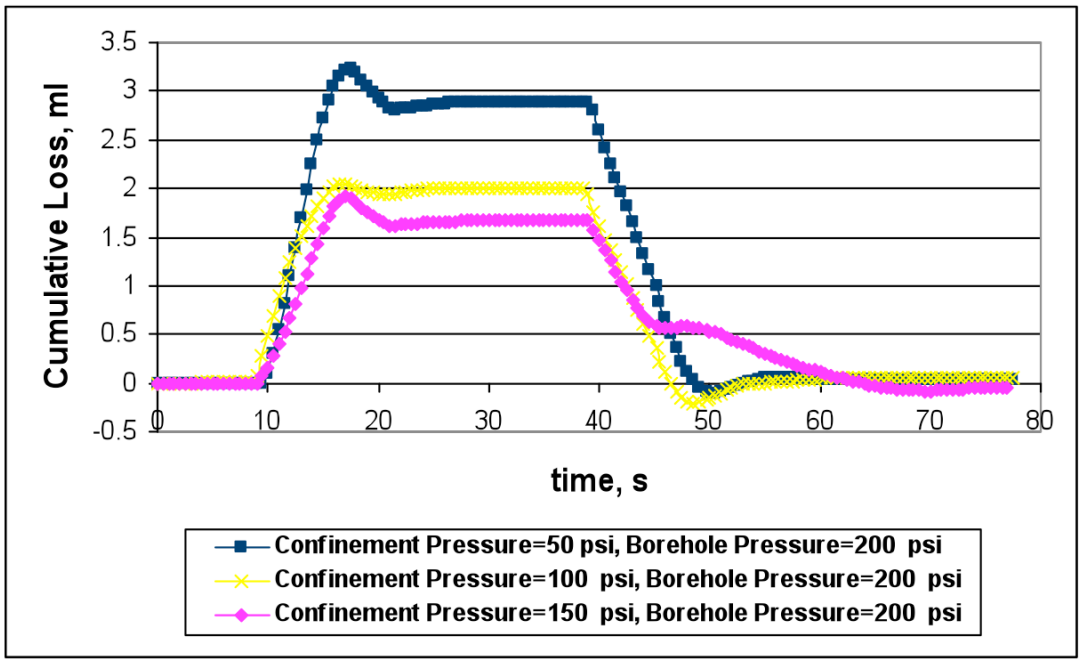

Figure 6-18: Effect of initial pressure in the fracture (confining pressure) on the cumulative mud loss in sandstone cores with rough fracture surfaces

6.1.5 Effect of Overbalance Pressure

Comparisons of the loss/gain rates from Figures 6-11 and 6-15, Figures 6-12 and 6-16, Figures 6-13 and 6-17, and Figures 6-14 and 6-18 shows that the same loss/gain values have been obtained for the same differential pressure (i.e., Borehole pressure – Confining pressure). Results shown in Table 6-1 indicate that mud loss/gain is effectively controlled by the differential pressure. This result has a match with the numerical result shown in Figure 4-4 as well.

Table 6-1: Experimentally observed maximum fluid loss/gain flow rates and cumulative losses under same overbalance pressure

Experiment performed with	Injection Pressure, psi	Confinement Pressure, psi	Differential Pressure, psi	Max. Loss Flow Rate, ml/min	Max. Gain Flow Rate, ml/min	Max. Cumulative Loss, ml
Sandstone core with smooth fracture surfaces	200	50	150	39.4	-22.551	3.45
Sandstone core with smooth fracture surfaces	250	100	150	38.91	-20.97	3.55
Sandstone core with smooth fracture surfaces	150	100	50	23.14	-17.74	2.15
Sandstone core with smooth fracture surfaces	200	150	50	19.7	-12.58	1.95
Sandstone core with rough fracture surfaces	150	100	50	18.48	-13.23	1.61
Sandstone core with rough fracture surfaces	200	150	50	18.73	-12.88	1.63
Sandstone core with rough fracture surfaces	200	50	150	36.94	-20.2	2.95
Sandstone core with rough fracture surfaces	250	100	150	36.73	-19.85	3.1

6.2 BOREHOLE BALLOONING EXPERIMENTS PERFORMED WITH AQUEOUS – POLYMER SOLUTIONS

In order to study the effect of non-Newtonian fluid rheology on the magnitude of the borehole ballooning, aqueous – Xanthan Gum solutions with 1 lb/bbl and 3 lb/bbl Xanthan Gum concentrations were used. Description and rheological characterization of aqueous – Xanthan Gum solutions were given in the Section 5.1.2. Experimental procedure is exactly the same as the one used for Newtonian fluid case and is explained in the Section 5.3.

The confining pressure, which was used to simulate the initial pressure within the fracture, was kept at 100 psi in all of the experiments. Initially both confining pressure and injection pressure were set at 100 psi, simulating the bottomhole pressure under no circulation condition. To mimic the intersection of a single horizontal fracture while drilling with bottomhole pressure higher than the formation pressure, fluid injection pressure was increased up to 200 psi. At the final stage of the experiment, fluid injection pressure was reduced again to its initial value of 100 psi to simulate the no circulation condition.

By increasing or decreasing the injection pressure while keeping the confinement pressure constant, a flow from the pump into the coreholder (mud loss) and reverse flow from the coreholder into the pump (mud gain) were induced. The test fluid was pumped into the core fracture by increasing the injection pressure to 200 psi and gained back by lowering the pressure back to the level of 100 psi confining pressure.

Figures 6-19, 6-21 and 6-23 demonstrate the effect of drilling mud rheology on the rate of mud loss/gain in fractured sandstone, granite and limestone core samples with smooth and rough surfaces, respectively. The results of these experiments suggest that increasing mud viscosity has a diminishing effect on the magnitude of borehole ballooning. No matter what lithology and surface characteristic the core sample has, thick fluid (i.e., high viscosity fluid) resulted least mud loss and gain flow rates. Thin fluid yield slightly

higher values of fluid loss/gain rates than thick fluid. The peak mud loss/gain values were observed when experiments performed with the thin Non-Newtonian fluid.

Figures 6-20, 6-22 and 6-24 show cumulative loss/gain volume of thick and thin fluid into fractured sandstone, granite and limestone core samples, respectively. Results are given both for rocks with smooth and rough surfaces. Cumulative mud loss is the highest in sandstone core sample with smooth surfaces in case of a thin Non-Newtonian type of drilling fluid. The lowest cumulative mud loss is observed with thick fluids flowing into the rocks with rough surfaces. Comparison of the cumulative loss results between the Figures 6-20, 6-22 and 6-24, shows that the magnitude of borehole ballooning phenomenon is very sensitive to drilling mud rheology.

Fracture surface roughness has still a noteworthy effect on the results of experiments performed with Non-Newtonian type of test fluid. As in the case of Newtonian fluid experiments, rough fractures had less cumulative mud loss rates by simply reducing the area open for flow of non-Newtonian fluids.

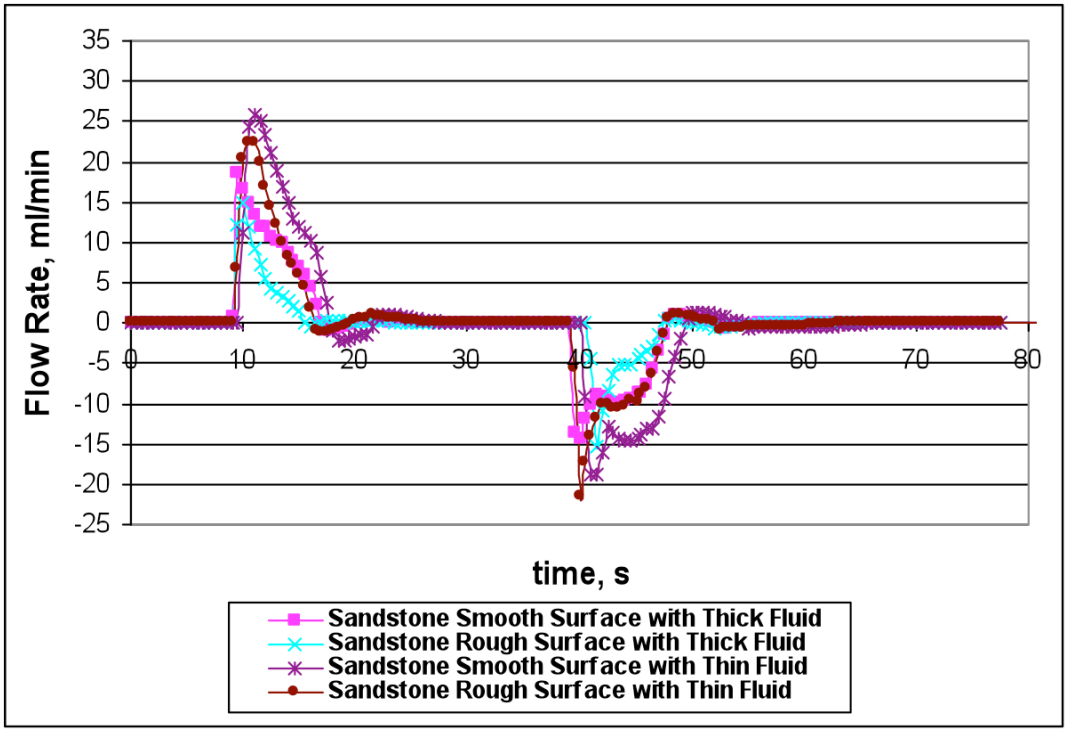

Figure 6-19: Effect of drilling fluid rheology on the mud loss/gain rate in sandstone cores with smooth and rough fracture surfaces

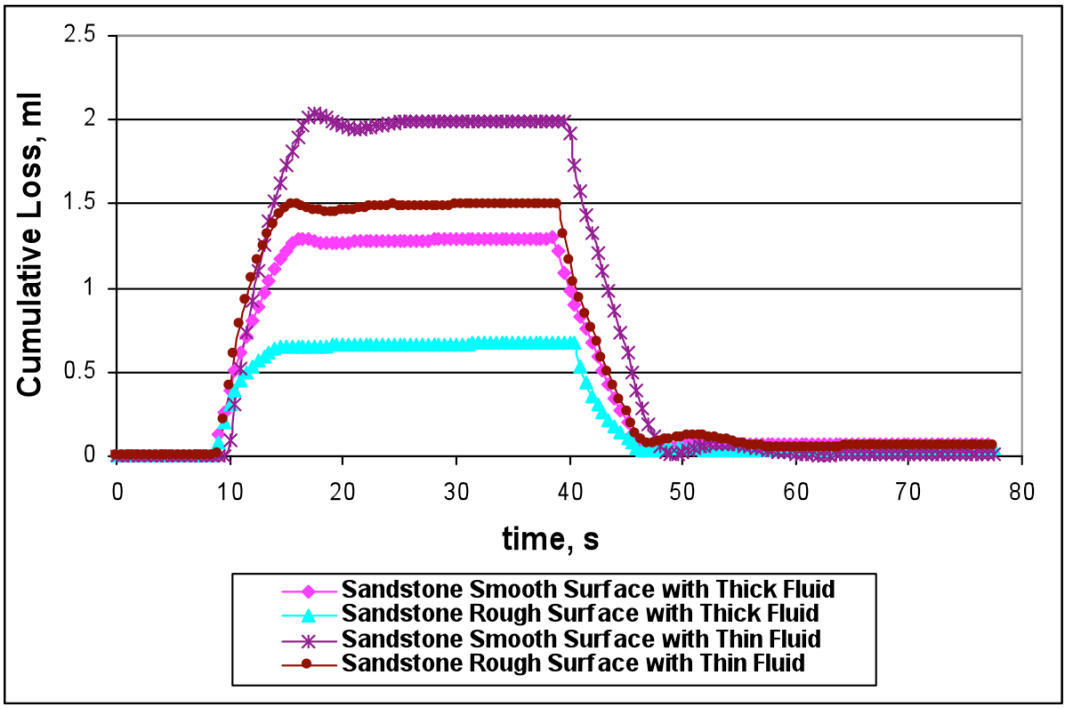

Figure 6-20: Effect of drilling fluid rheology on the cumulative loss in sandstone cores with smooth and rough fracture surfaces

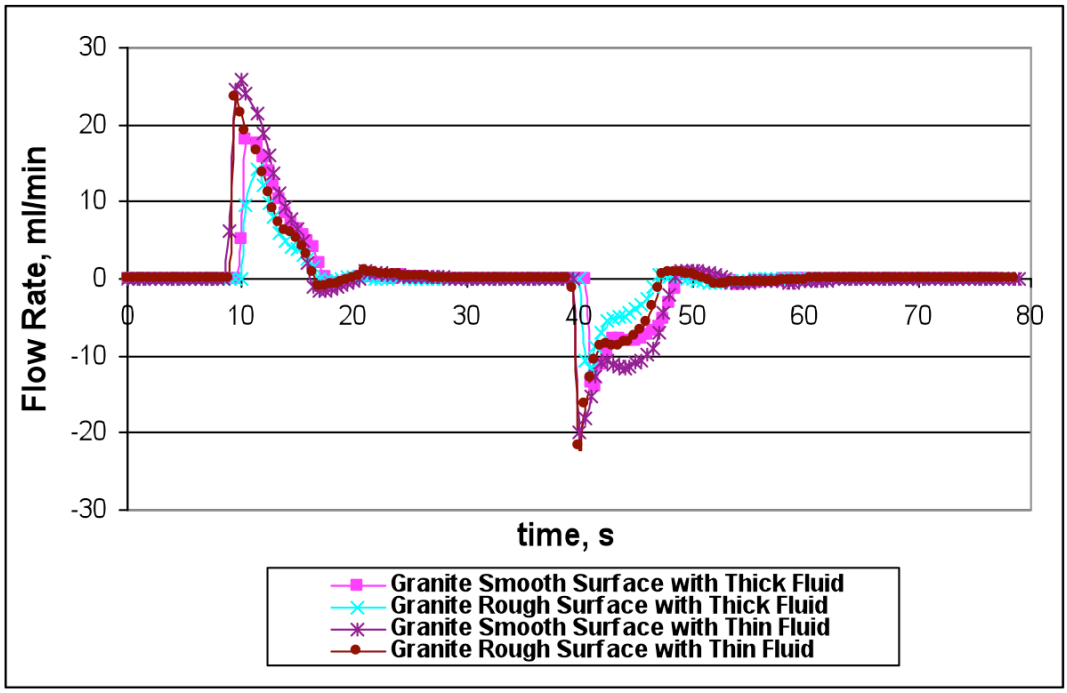

Figure 6-21: Effect of drilling fluid rheology on the mud loss/gain rate in granite cores with smooth and rough fracture surfaces

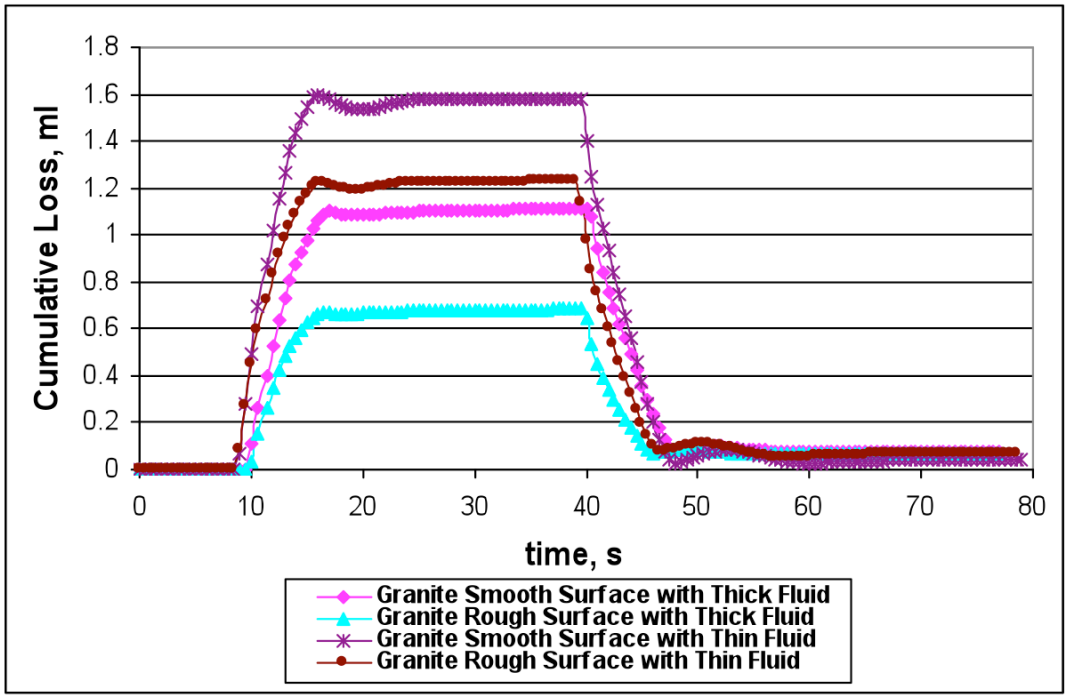

Figure 6-22: Effect of drilling fluid rheology on the cumulative loss in granite cores with smooth and rough fracture surfaces

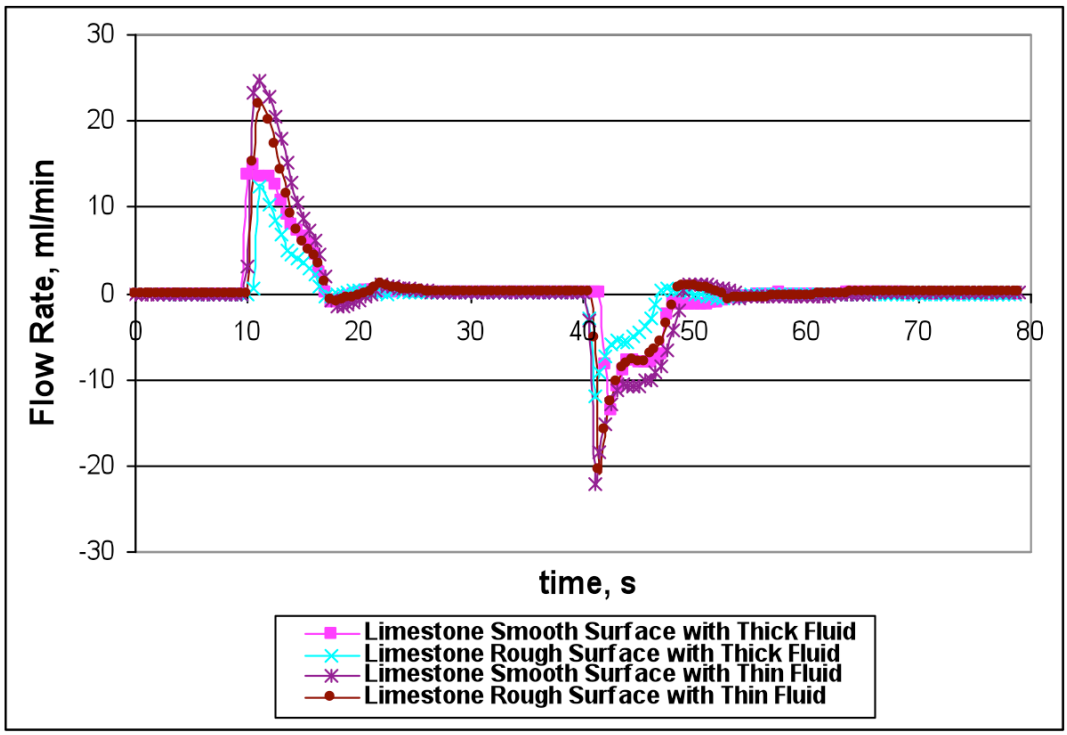

Figure 6-23: Effect of drilling fluid rheology on the mud loss/gain rate in limestone cores with smooth and rough fracture surfaces

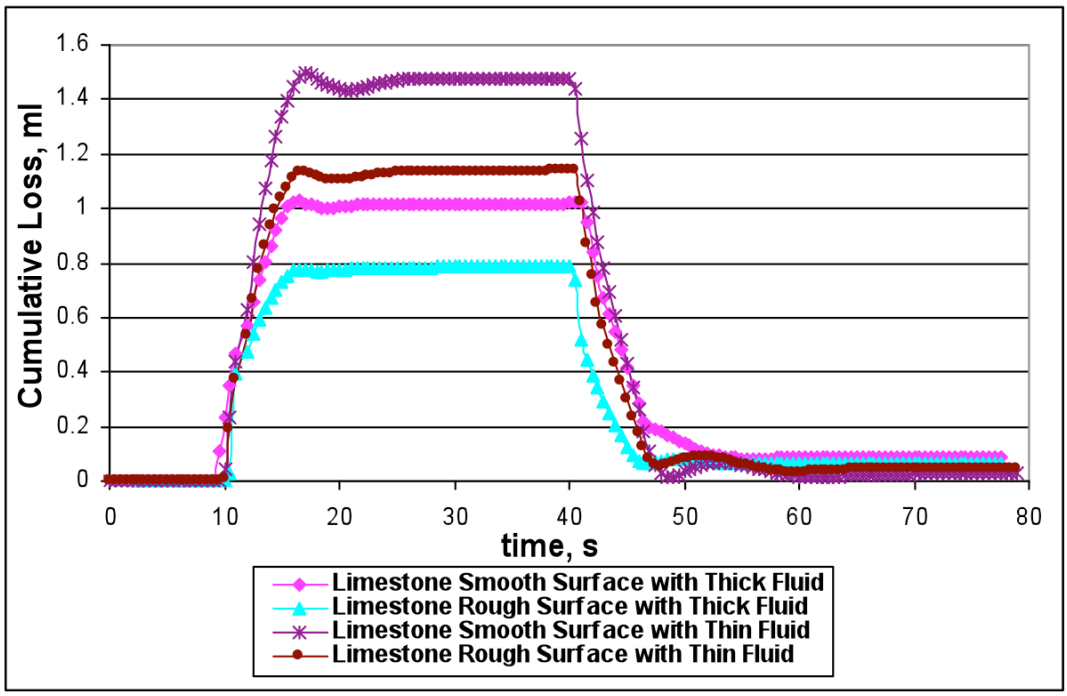

Figure 6-24: Effect of drilling fluid rheology on the cumulative loss in limestone cores with smooth and rough fracture surfaces

6.3 COMPARISON OF NUMERICAL MODEL RESULTS WITH EXPERIMENTAL OBSERVATIONS

The goal of this section is to compare the laboratory scale experimental observations with the numerical model results. Therefore, numerical simulations were run with laboratory scale data represented in Table 6.2 while incorporating the rheology data of each fluid into the model individually.

Table 6-2: Base data used for simulations run for comparison of numerical model results with experimental observations

Parameter	Value
x-discretization step	0.0125 m
y-discretization step	0.0125 m
Time discretization step	0.01 s
Fracture length, L_x	0.075 m
Fracture length, L_y	0.025 m
Fracture's normal stiffness, K_n	50000 MPa/m
Fracture's inclination, $\acute{\alpha}$	0
Initial fluid pressure in the fracture, P_0	100 psi
Well Pressure, P_W	200 psi
Duration of pressure increase and decrease, t_s	1 s
Total duration of the simulations, t	70 s
Fracture's normal compressibility, β	10^{-7} Pa^{-1}
Rock density, ρ_r	2500 kg/m^3

6.3.1 Water

Since the dynamics of flow is strongly controlled by fracture apertures, determining the initial aperture of each core has also been a point of interest. Each core sample was fully saturated with the test fluid and placed into the coreholder. A confinement pressure of 100 psi was used for all experiments and several injection rates were used with the second pump while preserving the confinement pressure constant at 100 psi. Flow rate versus pressure difference charts were drawn for each specific core and the average fracture aperture for each fracture core was calculated by using the Equation 28.

$$Q_x = L_y \frac{\Delta P}{L_x} \frac{w^3}{12\mu} \quad \text{.....(28)}$$

where Q_x is the flow rate into fracture (ml/sec), w is the aperture of the fracture (cm), μ is the dynamic viscosity of the fluid (Pa.sec), L_y is the lateral extend of the fracture (cm), L_x is the sample length (cm) and ΔP is the pressure drop across the core (Pa).

Figure 6-25 shows typical data for flow rate vs. pressure drop along the fracture obtained from an experimental run with the sandstone core sample with smooth fracture surfaces. Table 6-3 presents the average fracture aperture estimations for all investigated core samples.

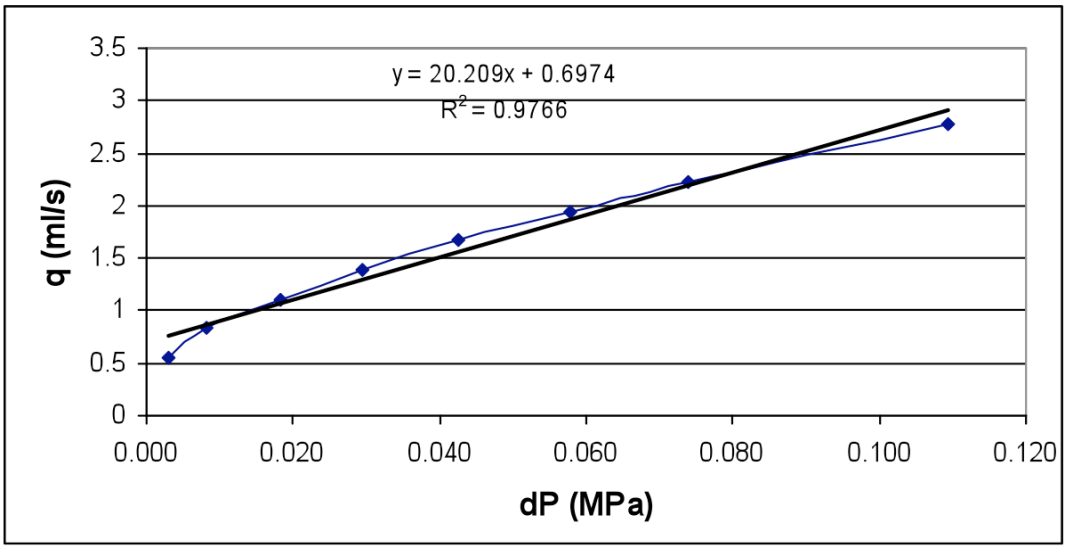

Figure 6-25: Flow rate vs. differential pressure drop along the fracture within the smooth sandstone core sample

Table 6-3: Experimentally observed aperture values of core samples under a confining pressure of 100 psi

Sample	Width, cm
Sandstone Rough	0.00104
Sandstone Smooth	0.00202
Limestone Rough	0.00115
Limestone Smooth	0.00146
Granite Rough	0.00098
Granite Smooth	0.00178

In order to compare experimental results with the ones from numerical model a rectangular shaped model with 60x20 grid size and very small time discretization steps were used. The simulation was run by assuming initial pressure in the fracture is 100 psi and the borehole pressure is 200 psi; same as the values considered for the experimental investigations. The smooth fracture aperture values shown in Table 6-3 were used for the numerical model calculations. In numerical simulations, the fracture normal stiffness (K_n) is assumed to be equal to $5x10^4$ MPa/m. This value is very close to the values measured in laboratory tests on rock specimens containing fractures (Bandis et al., 1983).

Comparisons of the results of numerical and experimental investigations are shown in Figures 6-26, 6-27 and 6-28. It was seen that model predictions of peak mud loss/gain rates show a similar trend as the ones from experiments. However, experimental values of peak mud loss/gain rates are generally higher than the predictions of the numerical model.

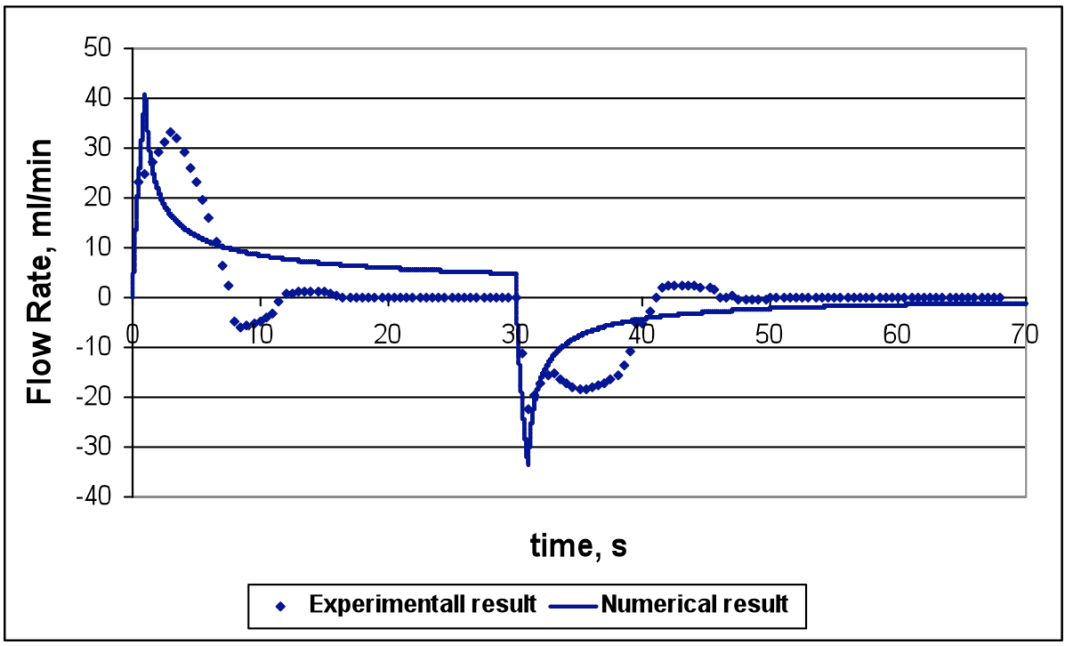

Figure 6-26: Comparison of numerical and experimental water loss/gain rates in sandstone cores with smooth fracture surfaces

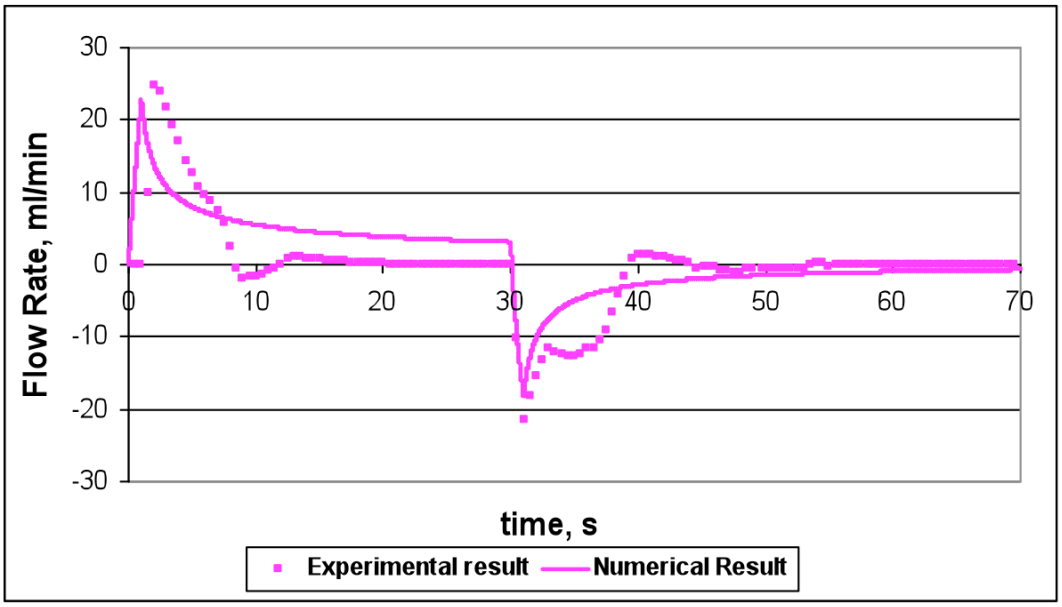

Figure 6-27: Comparison of numerical and experimental water loss/gain rates in limestone cores with smooth fracture surfaces

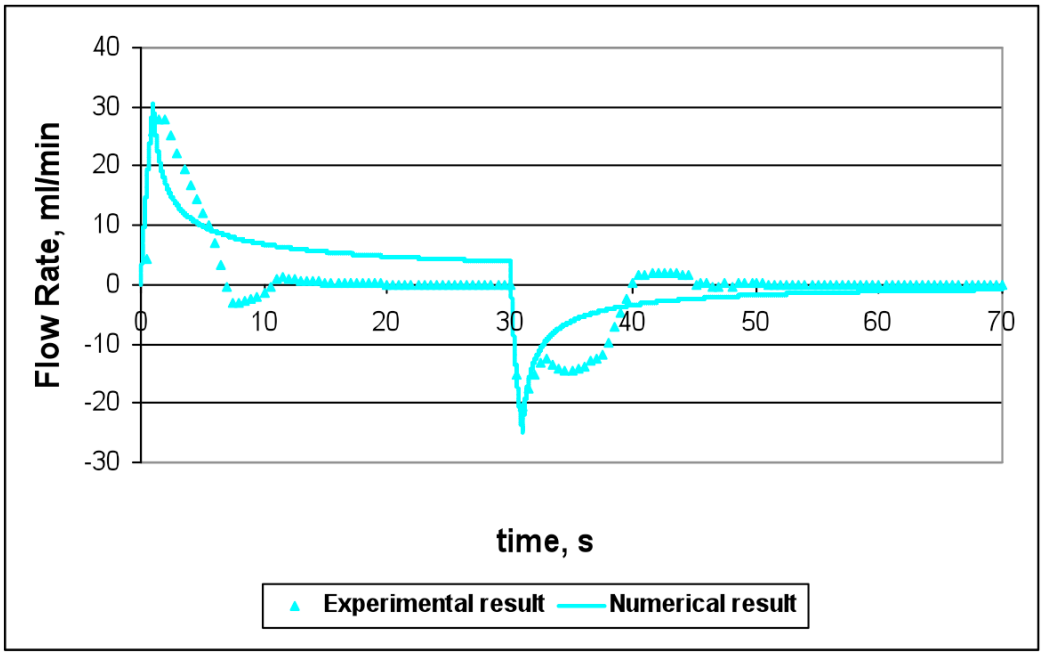

Figure 6-28: Comparison of numerical and experimental water loss/gain rates in granite cores with smooth fracture surfaces

6.3.2 Aqueous – Polymer Solutions

To compare experimental results obtained during experiments performed with aqueous – polymer solutions, a numerical model is constructed with a rectangular shape having 60x20 grid sizes. Rheological characterization of polymer solutions shown in Table 5-1 were incorporated into the model and simulations were run using very small time discretization steps. Initial pressure in the fracture is assumed 100 psi and the borehole pressure is assumed 200 psi; same as the values considered for the experimental investigations.

Comparisons of the results of numerical and experimental investigations for thin and thick polymer solutions are shown in Figures 6-29 to 6-34. It was observed that model predictions of peak mud loss/gain rates show a similar trend as the ones from experiments. Experimental values of peak mud loss/gain rates are generally identical to the predictions of the numerical model. However, mud loss/gain flow rates decrease at the faster rate on numerical results. It should be noted that for rough fracture surface numerical calculations, the surface roughness measurement of the actual core samples is needed.

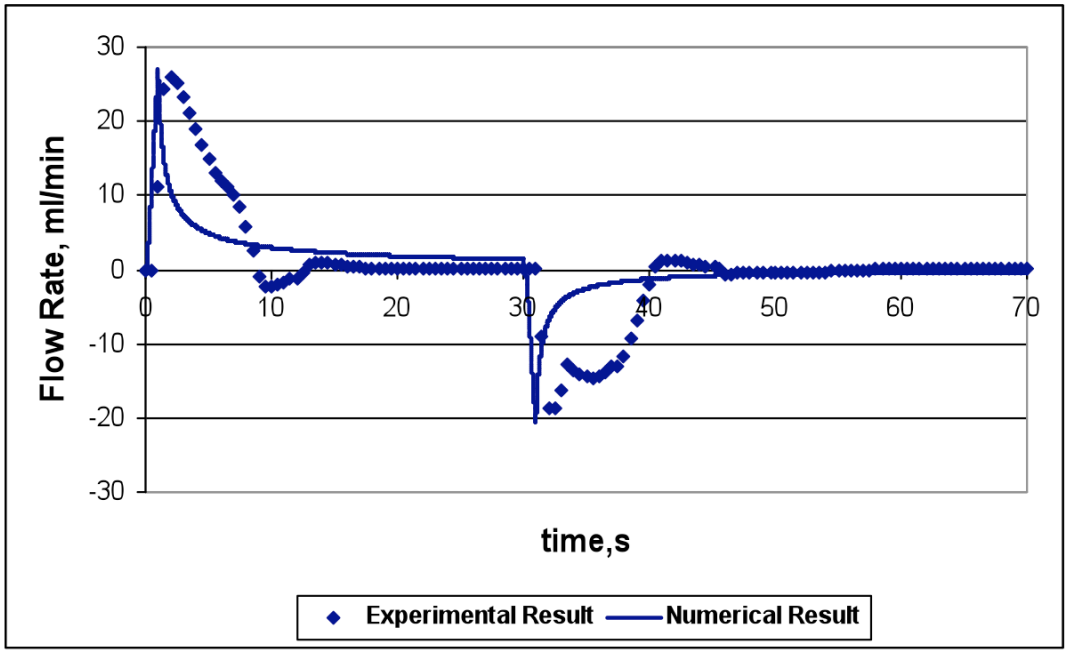

Figure 6-29: Comparison of numerical and experimental thin fluid loss/gain flow rates in sandstone cores with smooth fracture surfaces

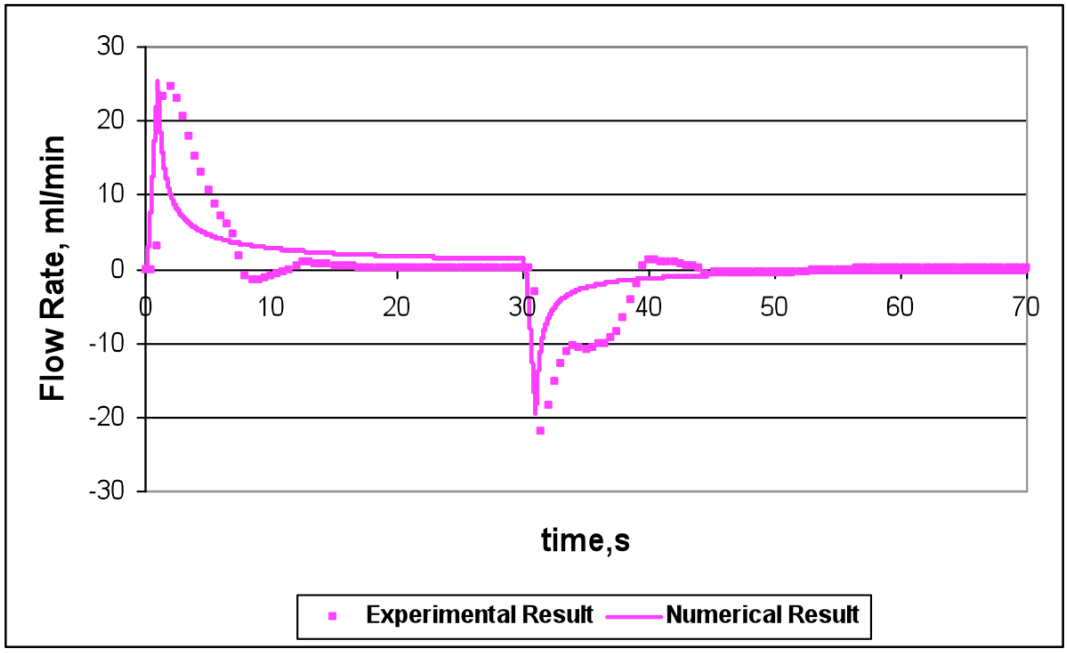

Figure 6-30: Comparison of numerical and experimental thin fluid loss/gain flow rates in limestone cores with smooth fracture surfaces

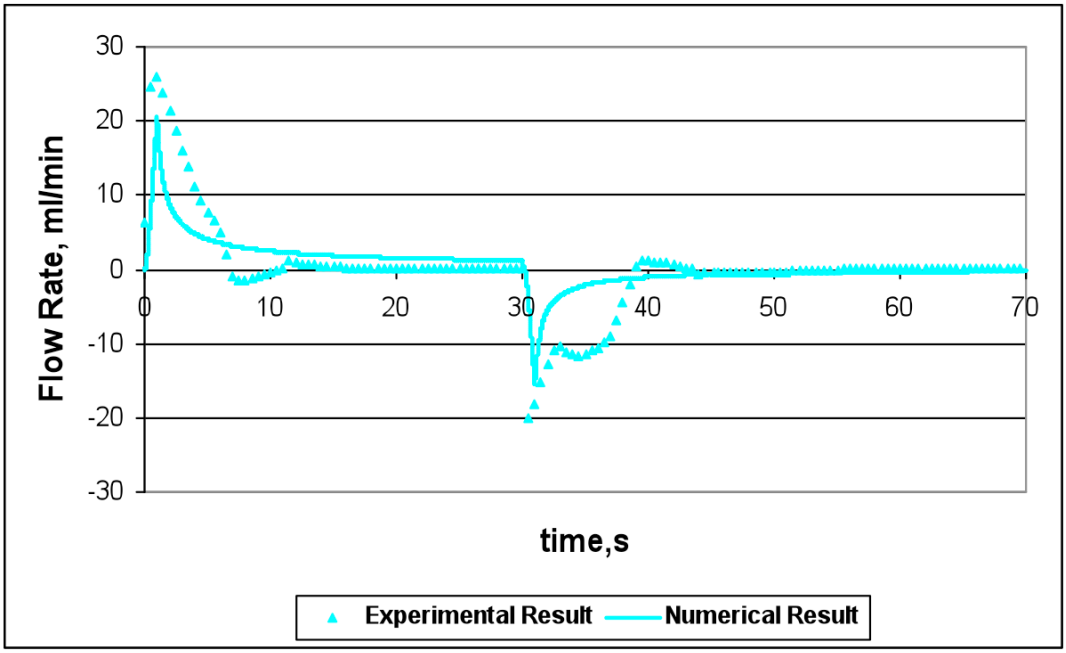

Figure 6-31: Comparison of numerical and experimental thin fluid loss/gain flow rates in granite cores with smooth fracture surfaces

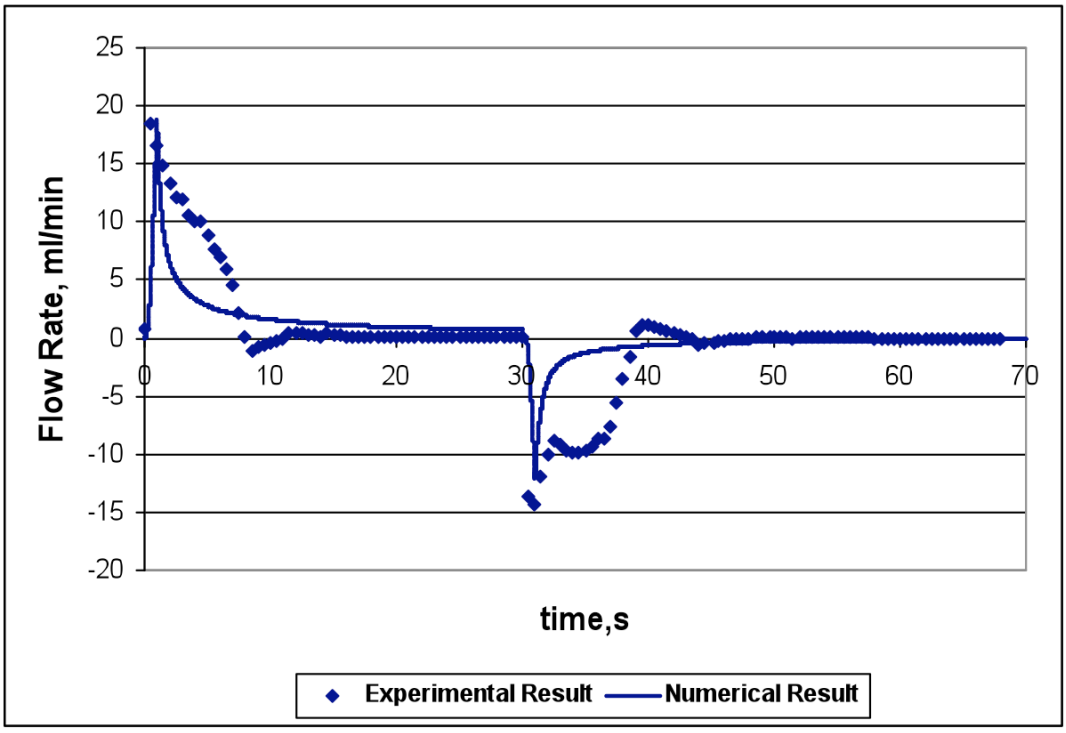

Figure 6-32: Comparison of numerical and experimental thick fluid loss/gain flow rates in sandstone cores with smooth fracture surfaces

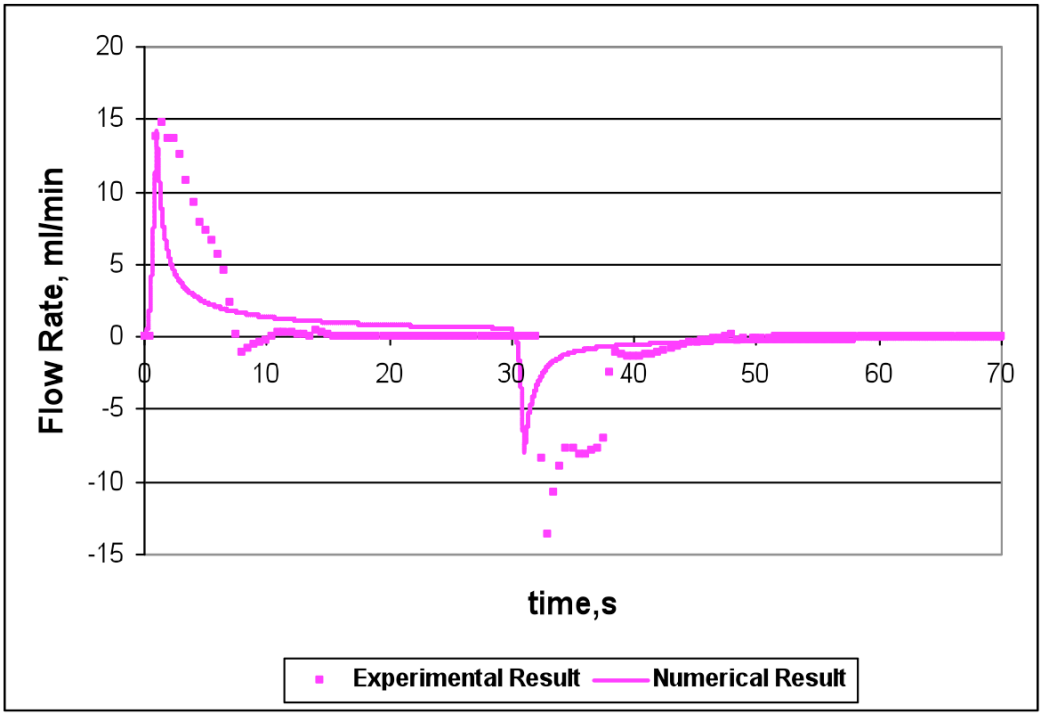

Figure 6-33: Comparison of numerical and experimental thick fluid loss/gain flow rates in limestone cores with smooth fracture surfaces

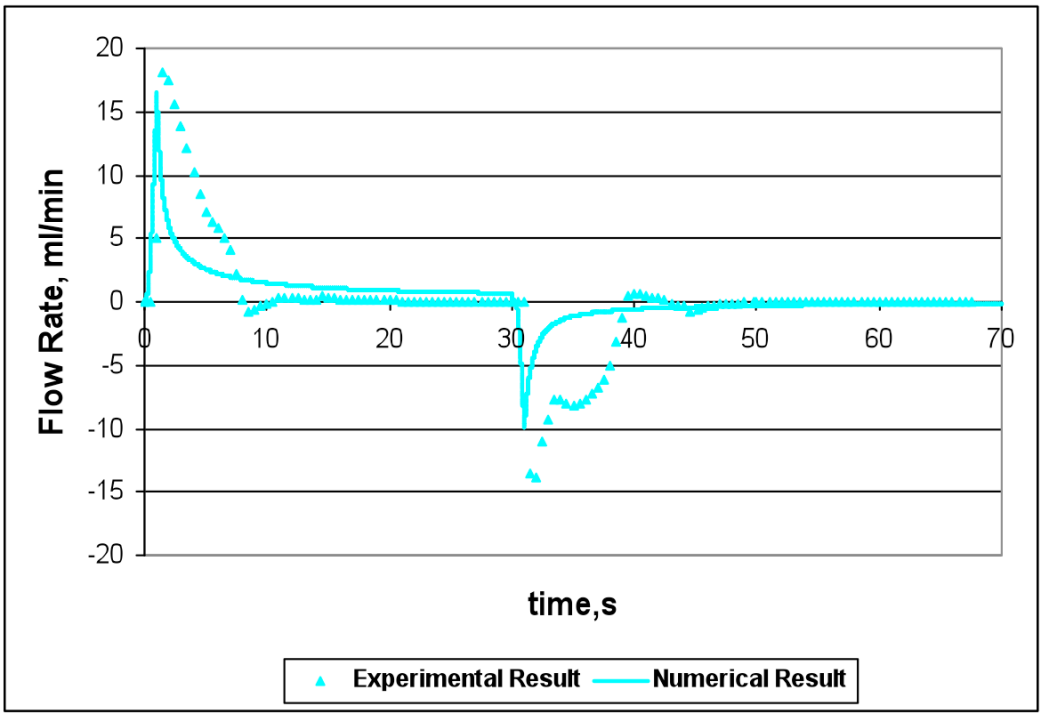

Figure 6-34: Comparison of numerical and experimental thick fluid loss/gain flow rates in granite cores with smooth fracture surfaces

CHAPTER 7 : CONCLUSIONS

In numerical simulation study, it was seen that as the over balance pressure increases both initial and mid-simulation peaks and accompanying tails increase. Experiments also showed that the mud loss/gain values did not change when different combinations of borehole and confinement pressures were used as long as the overbalance pressure (i.e., the difference between borehole pressure and formation pore pressure) stayed the same. Therefore, it was concluded that the difference between the initial formation fluid pressure and the borehole pressure (i.e. overbalance pressure) governs the fluid flow dynamics between the borehole and the fracture. Borehole ballooning magnitude is found to be very sensitive to the wellbore location within the fracture. Highest mud loss/gain flow rates have been observed in a fracture hit by a vertical wellbore from the center. Moving the well to the edge and to the corner of fracture consecutively reduces the initial and mid simulation peaks and increases the duration of the peak tails. The flow rate decreases at the faster rate when the borehole is located in the center of the fracture and decreases at the slower rate when the borehole is located at the periphery.

The fracture length has a slight effect on the initial simulation flow rates. The fluid flow is not affected by the far end of the fracture at the beginning. For a longer fracture, the charge and discharge of the drilling fluid last longer since it takes greater time for the pressure to come equilibrium along the fracture. The fluid loss and gain is expected to be higher in a longer fracture.

Varying initial aperture changes the initial and mid simulation mud gain/loss peaks, but does not affect the decay rate. Mud flow dynamics are very sensitive to the initial aperture of the fractures encountered during drilling.

Both experimental and numerical model results suggest that fracture surface roughness has a noticeable effect on the magnitude of borehole ballooning event. Rough fractures yield slightly lower values of fluid loss loss/gain rate than smooth fractures. Fluid loss/gain values are controlled by the effective area open to flow, which is directly related to the degree of roughness. Increasing fracture surface roughness reduces the effective fracture surface area open for flow and thereby decreases the mud gain and loss flow rates.

If the fracture aperture values vary significantly (i.e.,standard deviation of the fracture aperture values is high) the magnitude of the borehole ballooning in partially contacting fractures is reduced. Hurst exponent or fractal dimension variation has relatively smaller effect on borehole ballooning. However, the difference between the mud loss/gain flow rates achieved by simulating surface data using Hurst numbers H = 0.4 and H= 0.9 cannot be assumed negligible.

In numerical model simulations, decreasing the fracture grid size number did not affect the initial and mid-simulation peaks but it had a dramatic effect on the tail of the mud loss and mud gain flow rate versus time.

The results of the simulations carried out with 64x64 data have remarkably lower mud loss decay rate. This can be interpreted as an increasing accuracy of the input surface roughness data. It also implies that the selection of the scale used for data collection and fracture surface roughness generation is highly crucial in the modeling studies.

There is a critical value of fracture aperture value above which the fracture can be modeled as a smooth-walled fracture. The average fracture aperture range assumed in this study (1-2 mm) is below the critical value to assume that the roughness effect is negligible.

The results of the experiments suggest that fracture surface roughness has a noticable effect on the magnitude of borehole ballooning event. Rough fractures yield slightly lower values of fluid loss loss/gain rate than smooth fractures. Fluid loss/gain values observed in the experiments are controlled by the effective area open to flow, which is directly related to the degree of roughness.

The highest cumulative mud loss/gain value was obtained in the sandstone sample. Limestone and granite core samples showed very similar flow rate and cumulative loss results. The higher mud loss/gain values obtained in sandstone sample can be attributed to the fact that sandstone could have lower surface roughness.

Experimental results also showed that increasing the borehole (injection) pressure considerably increased the mud loss/gain rates and the cumulative loss. Mud loss/gain dynamics were found to be very sensitive to well pressure variations. For a given borehole (injection) pressure, higher initial pressure in the fracture leads to lower mud loss/gain volume. The same loss/gain values have been obtained for the same differential pressure (i.e., borehole pressure – confinement pressure). This result indicates that mud loss/gain is effectively controlled by the differential pressure.

Comparison of the results shows that the magnitude of borehole ballooning phenomenon is very sensitive to drilling mud rheology. Fracture surface roughness has a noteworthy effect on the volume of fluid coming in and out of the rock when Non-Newtonian type of test fluid was used.

The results of the experiments suggest that increasing mud viscosity has a diminishing effect on the magnitude of borehole ballooning. Independent from lithology and surface characteristic the core sample, the thick Power Law fluid (i.e., fluid with highest viscosity) resulted least mud loss and gain rates. Thin Power Law fluid yield slightly higher values of fluid loss/gain rates than thick Power Law fluid. Maximum mud loss/gain values observed in experiments performed with the Newtonian fluid.

REFERENCES

BABADAGLI, T. and DEVELI, K., Fractal Analysis of Natural and Synthetic Fracture Surfaces of Geothermal Reservoir Rocks; Proceedings of 2000 World Geothermal Congress, Kyushu-Tohoku, Japan, pp. 2515-2520, May 28-June 10, 2000.

BABADAGLI, T. and DEVELI, K., On the Application of Methods Used to Calculate the Fractal Dimension of Fracture Surfaces; Fractals, Vol. 09, No. 1, pp. 105-128, 2001.

BABADAGLI, T. and DEVELI, K.: Fractal Characteristics of Rocks Fractured Under Tension, Theoretical and Applied Frac. Mech., vol.39, no.1, 73-88,2003.

BABADAGLI, T., Analysis of the Displacement in Fractal Lattices with Different Number of Grids; Fractals, Vol. 13, No. 3, pp. 207-213, 2005.

BANDIS, S. C., LUMSDEN, A. C., BARTON, N. R., Fundamentals of Rock Joint Deformation; International Journal of Rock Mechanics Mining Science and Geomechanics Abstracts, Vol. 20, pp. 249, 1983.

BECK, F.E., POWEL, J.W. and ZAMORA, M.: "A Clarified Xanthan Drill-in Fluid for Prudhoe Bay Horizontal Wells," SPE 25767, SPE/IADC Drilling Conference, Amsterdam, The Netherlands, Feb 23-25, 1993.

BLESSING, G. V. and EITZE, D. G., Surface Roughness Sensed by Ultrasound; Surface Topography, Vol. 1, pp.143-158, 1988.

BRINKSMEIER, E. and RIEMER, O., Measurement of Optical Surfaces Generated by Diamond turning; International Journal of machine Tools and Manufacture, Vol. 38 (5-6), pp. 699-705, 1998.

BROWN, S. R., A note on the description of surface roughness using fractal dimension. Geophys. Res. Lett., 14(11): 1095-1098, 1987a

BROWN, S. R., Fluid flow through rock joints: The effect of surface roughness. Jour. Geophys. Res., 92 (B2): 1337-1347, 1987b

BROWN, S. R, and SCHOLZ, S. H., Broad Bandwidth Study of the Topography of Natural Rock Surfaces; Journal of Geophyscial Research, Vol. 90 (14), pp. 12575-12582, 1985.

BRUEL, D. et al., Modelling Storage Behaviour in a Fractured Rock Mass; Journal of Hydrology, Vol. 162, pp. 267-278, 1994.

BRUSH, D.J. and THOMSON, N. R., Fluid Flow in Synthetic Rough-Walled Fractures: Navier-Stokes, Stokes and Local Cubic Law Simulation; Water Resources Research, Vol. 39 (4), pp.1085, 2002.

CAMERON, C., Drilling Fluid Design and Management for Extended Reach Wells, SPE 72290, presented at the IADC Middle East Drilling Technology of SPE, Bahrain, 22-24 October 2001.

DEN OUTER, A., KAASHOEK, J. F., HACK, H. R. G. K., Difficulties with Using Continuous Fractal Theory for Discontinuity Surfaces; International Journal of Rock Mechanics and Mining Sciences and Geomechanics Abstracts, Vol. 32 (1), pp. 3-9, 1995.

DEVELI, K. and BABADAGLI, T., Quantification of Natural Fracture Surfaces Using Fractal Geometry, Mathematical Geology, vol. 30, no.8, pp. 971-998, 1998.

DEVELI, K., BABADAGLI, T., COMLEKCI, C., A New Computer-Controlled Surface-Scanning device for Measurement of Fracture Surface Roughness; Computers and Geosciences, Vol. 27, pp. 265-277, 2001.

EMANUEL, A. S., ALAMEDA, G. K., BEHRENS, R. A., HEWETT, T. A., Reservoir Performance Prediction Methods Based on Fractal Geostatistics; SPE Reservoir Engineering, pp. 311-318, August 1989.

FECKER, E. and RENGERS, N., Measurement of Large Scale Roughness of Rock Planes by Means of Profilograph and Geological Compass; Proc. Symposium Rock Fracture, Nancy, pp. 1-18, 1971.

FERRARO, A. M. and GIANI, G. P., Geostatistical Description of the Joint Surface Roughness, Proceedings of the 31st U.S. Symposium on Rock Mechanics, Golden, Colorado, Rock Mechanics Contributions and Challenges, Balkema, Rotterdam, pp. 463-470, 1990.

FISHER C.C., CONSTIEN, V.G., AASADI, M.: "Novel Application of Synergistic Guar/Non-Acetylated Xanthan Gum Mixtures in Hydraulic Fracturing," paper SPE 65037 presented at the 2001 SPE International Symposium on Oilfield Chemistry, Houston, Texas, Feb. 13-16.

FOURNIER, A., FUSSEL, D., CARPENTER, L., Computer Rendering of Stochastic Models; Commun. ACM, Vol. 25, pp. 371-384, 1982.

GILL, J.A., How Borehole Ballooning Alters Drilling Responses; Oil & Gas Journal , Vol. 87, No. 11, pp. 43-50, March 1989.

GLEYZES, P., LORIETTE, V., SAINT-JALMES, H., BOCCARA, A. C., Roughness Measurement in the Picometric Range Using a Polarization Interferometer and a Multichannel Lockin Detection Technique; International Journal of Machine Tools and Manufacture, Vol. 38 (5-6), pp. 715-717, 1998.

GRIGORIEV, A. Y., CHIZHIK, S. A., MYSHKIN, N. K., Texture Classification of Engineering Surfaces with Nanoscale Roughness; International Journal of Machine Tools and Manufacture, Vol. 38 (5-6), pp. 719-724, 1998.

HAKAMI, E. and LARSSON, E., Aperture Measurements and Flow Experiments on a Single Natural Fracture, International Journal of Rock Mechanics and Mining Sciences and Geomechanics Abstracts, Vol. 33, No. 4, pp. 395-404, 1996.

HEWETT, T. A., Fractal Distributions of Reservoir Heterogeneity and Their Influence on Fluid Transport; In SPE 15386, Society of Petroleum Engineers, 58th Annual Technical Conference and Exhibition, New Orleans, 5-8 October 1986.

HUANG, S. L., OELFKE, S. M., SPECK, R. C., Applicability of Fractal Characterization and Modeling to Rock Joint Profiles; International Journal of Rock Mechanics and Mining Sciences and Geomechanics Abstracts, Vol. 29 (2), pp. 89-98, 1992.

IWAI, K., Fundamental Studies of fluid flow through a single fracture, Ph.D. Thesis, University of California Berkeley, California, USA, 1976

JAKOBS, S., DUPARRE, A., TRUCKENBRODT, H., AFM and Light Scattering Measurements of Optical Thin Films for Applications in the UV Spectral Region; International Journal of Machine Tools and Manufacture, Vol. 38 (5-6), pp. 733-739, 1998.

JESSELL, M. W., COX, S. J. D., SCHAWARZE, P., POWER, W., The Anisotropy of Surface Roughness Measured Using a Digital Photogrammetric Technique; In Fractography: Fracture Topography as a Tool in Fracture Mechanics and Stress Analysis, Geological Society (London) Special Publication, Vol. 92, pp. 27-37, 1995.

KIRAN, M. B., RAMAMOORTHY, B., RADHAKRISHAN, V., Evaluation of Surface Roughness by Vision System; International Journal of Machine Tools and Manufacture, Vol. 38 (5-6), pp. 685-690, 1998.

KROHN, C. E. and THOMPSON, A. H., Fractal Sandstone Pores: Automated Measurements Using Scanning-Electron-Microscope Images; Physical Review B, Vol. 33 (9), pp. 6366-6374, 1986.

KULATILAKE, P. H. S.W., SHOU, G., HUANG, T. H., MORGAN, R. M., New Peak Shear Strength Criteria for Anisotropic Rock Joints; International Journal of Rock Mechanics and Mining Sciences and Geomechanics Abstracts, Vol. 32 (7), pp. 673-697, 1995.

KULATILAKE, P. H. S.W. and UM, J., Requirements for Accurate Quantification of Self-Affine Roughness Using the Roughness-Length Method; International Journal of Rock Mechanics and Mining Sciences and Geomechanics Abstracts, Vol. 36, pp. 5-18, 1999.

LAVROV, A. and TRONVOLL, J., Mud Loss into a Single Fracture during Drilling of Petroleum Wells; Proceedings of 6th International Conference on Analysis of Discontinuous Deformation, Trondheim, Norway, pp. 189-198, 2003

LAVROV, A. and TRONVOLL, J., Modeling Mud Loss in Fractured Formations, SPE 88700 presented at the 11th Abu Dhabi International Petroleum Exhibition and Conference of SPE, Abu Dhabi, UAE, 10-13 October 2004.

LAVROV, A. and TRONVOLL, J., Mechanics of Borehole Ballooning in Naturally-Fractured Formations; SPE 93747-MS presented at Middle East Oil and Gas Show and Conference of SPE, Kingdom of Bahrain, 12-15 March 2005.

LAVROV, A. and TRONVOLL, J., Numerical Analysis of Radial Flow in a Natural Fracture, SPE 103564 presented at the 13th Abu Dhabi International Petroleum Exhibition and Conference of SPE, Abu Dhabi, UAE, 5-8 October 2006

LIETARD, O., KIRVELIS, R. and GUILLOT, D., The Radial Flow Model of Mud Loss into Natural Fractures, SPE 88661 received by the SPE office in Richardson, Texas, 17 April 2004.

LI, W.D., TIAN, J. and LIU, Y.Z.: "Pilot Test of Xanthan Gum Flooding in Shengli Oilfield," Paper SPE 57294, SPE Asia Pacific Improved Oil recovery Conference, Kuala Lumpur, Malaysia, Oct. 25-26, 1999.

LIN, T. Y. and PENG, G. S., Nanometrology of Surface Topography: Application to the Research in Development of a New Mass Standard; International Journal of Machine Tools and Manufacture, Vol. 38 (5-6), pp. 707-713, 1998.

LOMIZE, G. M., Water Flow through Jointed Rock (in Russian), Gosudastvennoe Energetitcheskoe Izdatelstvo, Moscow, Russia, 1951

MANDELBROT, B. B., The Fractal Geometry of Nature; W. H. Freeman, NewYork, 1982.

MANDELBROT, B. B., PASSOJA, D. E., PAULLAY, A. J., Fractal Character of Fracture Surfaces of Metals; Nature, Vol. 308, pp. 721-722, 1984.

MARK, D. M. and ARONSON, P. B., Scale-Dependent Fractal Dimension of Topographic Surfaces: An Empirical Investigation with Applications in Geomorphology and Computer Mapping; Mathematical Geology, Vol. 16 (7), pp. 671-683, 1984.

NAVIER, C. L., Memoire Sur Les Lois Du Mouvement des Fluides (in French), Mem. Acad. Sci. Inst., Vol. 6, pp. 389, 1822

NEUZIL, C. E. and TRACY, J. V., Flow through Fractures, Water Resources Research, Vol. 17, pp. 191-199, 1981

NOWICKI, B. and JARKIEWICZ, A., The In-Process Surface Roughness Measurement Using Fringe Field Capacitive (FFC) Method; International Journal of Machine Tools and Manufacture, Vol. 38 (5-6), pp. 725-732, 1998.

ORON, A. P. and BERKOWITZ, B., Flow in Rock Fractures: The Local Cubic Law Assumption Reexamined; Water Resources Research, Vol. 34 (11), pp 2811-2825, 1998.

PANDE, C. S., RICHARDS, L. R., SMITH, S., Fractal Characteristics of Fractured Surfaces; Journal of Materials Science Letters, Vol. 6, pp. 295-297, 1987.

PINKUS, O. and STERNLICHT, B., Theory of Hydrodynamic Lubrication; McGraw-Hill Book Company Inc., 1961.

POWER, W. L., TULLIS, T. E., BROWN, S. R., BIORNOTT, G. N., SCHOLZ, C. H., Roughness of Natural Fault Surfaces; Geophysical Research Letters, Vol. 14 (1), pp. 29-32, 1987.

POWER, D., CATALIN, I. and BROOKS, S., The Top 10 Lost Circulation Concerns in Deepwater Drilling, SPE 81133, presented at the Latin American and Caribbean Petroleum Engineering Conference of SPE, Port of Spain, Trinidad, West Indies, 27-30 April 2003.

RAM BABU, D., Effect of P-ρ-T Behavior of Muds on Loss/Gain During High Temperature Deep Well Drilling; Journal of Petroleum Science and Engineering , Vol. 20, No. 1, pp. 49-62, April 1998.

RENGERS, N., Influence of Surface Roughness on the Friction Properties of Rock Planes; Proceedings of the Second Congress of International Society of Rock Mechanics, Belgrade, Vol. 1, pp. 229-234, 1970.

REYNOLDS, O., On the Theory of Lubrication and its Application to Mr. Beauchamp Tower's Experiments, Phil. Trans. Roy. Soc., London, vol. 177, 1886.

SALAMONE, J.C., Clough, S.B., SALAMONE, A. Beal, Reid, K.I.G., JAMISON, D.E.:"Xanthan Gum- A Lyotropic Crystalline Polymer and its Properties as a Suspending Agent," SPE 9097 SPEJ Forum Article,1982.

SANFILIPPO, F. et al., Characterization of Conductive Fractures while Drilling, SPE 38177 presented at European Formation Damage Conference of SPE, The Hauge, Netherlands, 2-3 June 1997.

SAUPE, D., Algorithms for Random Fractals; In the Science of Fractal Images, Springer-Verlag, New York, pp. 71-113, 1988.

SCHMITTBUHL, J., GENTIER,S., ROUX, S., Field Measurements of the Roughness of Fault Surfaces, Geophyscial Research Letters, Vol. 20 (8), pp. 639-641, 1993.

SCHMITTBUHL, J., SCHMITT, F., SCHOLZ, C., Scaling Invariance of Crack Surfaces, Journal of Geophyscial Research, Vol. 100 (B4), pp. 5953-5973, 1995.

SHIRONO, T. and KULATILAKE, P. H. S. W., Accuracy of the Spectral method in Estimation Fractal/Spectral Parameters for Self-Affine Roughness Profiles; International Journal of Rock Mechanics and Mining Sciences and Geomechanics Abstracts, Vol. 34 (5), pp 789-904, 1997.

SNOW, D.T., Anisotropic Permeability of Fractured Media, Water Resources Research, Vol. 5, No. 6, pp. 1173-1189, 1969.

TARE, U.A., WHITFILL, L.D. and MODY, F.K., Drilling Fluid Losses and Gains: Case Histories and Practical Solutions; SPE 71368-MS presented at Annual Technical Conference and Exhibition of SPE, New Orleans, Louisiana, USA, 30 September-3 October 2001.

TSANG, Y.W. and TSANG, C.F., Flow Channeling in a Single Fracture, Water Resources Research, Vol. 25, No. 9, pp. 2076-2080, 1989

TURK, N., GREIG M. J., DEARMAN, W. R., AMIN, F. F., Characterization of Rock Joint Surfaces by Fractal Dimension; Proceedings of 28th U.S. Rock Mechanics Symposium, Balkema, Boston, pp. 1223-1236, 1987.

VERGA, F. et al., Detection and Characterization of Fractures in Naturally Fractured Reservoirs, SPE 63266 presented at ATCE of SPE, Dallas, Texas, 1-4 October 2000.

VOSS, R.F., Random Fractal Forgeries; NATO ASI Series, Springer-Verlag., Berlin, pp.805-835, 1985.

WANG, J. S. Y., NARASIMHAN, T. N., SCHOLZ, C. H., Aperture Correlation of a Fractal Fracture; Journal of Geophysical Research, Vol. 93 (B3), pp. 2216-2224, 1988.

WARD, C. and CLARK, R., Anatomy of Borehole Ballooning using PWD tool, presented at the Overpressures in Petroleum Exploration workshop, Pau, France, 7-8 April 1998.

WITHERSPOON, P. A. et al., Validity of Cubic Law for Fluid Flow in a Deformable Rock Fracture, Water Resources Research, Vol. 16, No. 6, pp. 1016-1024, 1980

WONG, P., HOWARD, J., LIN, J., Surface Roughening and the Fractal Nature of Rocks; Physical Review Letters, Vol. 57, pp. 637-640, 1986.

WOOLEY, R. W., Pneumatic Method for Making Fast, High Resolution Non-Contacting Measurement of Surface Topography; Proceedings of SPIE 1573, pp. 205-215, 1991.

WYANT, J. C. and SCHMIT, J., Large Field of View, High Spatial Resolution, Surface Measurements; Journal of Machine Tools, Vol. 38 (5-6), pp. 691-698, 1998.

YOKOYA, N., YAMAMATO, K., FUNAKUBO, N., Fractal Based Analysis and Interpolation of 3D Natural Surface Shapes and Their Application to Terrain Modelling; Computer Vision, Graphics and Image Processing, Vol. 46, pp. 284-302, 1989.

ZIMMERMANN, R.W., KUMAR, S. and BODVARSSON, G.S., Lubrication Theory Analysis of the Permeability of Rough-walled Fractures; Journal of Rock Mechanics and Mining Sciences and Geomechanics Abstracts, Vol. 28, No. 4, pp. 325-331, 1991.

APPENDIX A: DERIVATION OF CONTINUITY EQUATION

Mass Balance over a stationary volume element ΔxΔyΔz:

Rate of Mass Accumulation	=	Rate of Mass In	-	Rate of Mass Out

$$\Delta x\Delta y\Delta z\frac{\partial \rho}{\partial t} = \Delta y\Delta z\left[\rho v_x\big|_x - \rho v_x\big|_{x+\Delta x}\right] + \Delta x\Delta z\left[\rho v_y\big|_y - \rho v_y\big|_{y+\Delta y}\right] + \Delta x\Delta y\left[\rho v_z\big|_z - \rho v_z\big|_{z+\Delta z}\right] \quad \text{..... (A-1)}$$

By dividing Equation A-1 by ΔxΔyΔz and taking the limit as these dimensions approach zero, we reach the equation of continuity.

$$\frac{\partial \rho}{\partial t} = -\left[\frac{\partial}{\partial x}\rho v_x + \frac{\partial}{\partial y}\rho v_y + \frac{\partial}{\partial z}\rho v_z\right] \quad \text{..... (A-2)}$$

Equation of Continuity (Eqn. A-2) describes the rate of change of density at a fixed point. The equation is modified by performing the indicated differentiation and collecting all derivatives of ρ on the left hand side:

$$\frac{\partial \rho}{\partial t} + v_x\frac{\partial \rho}{\partial x} + v_y\frac{\partial \rho}{\partial y} + v_z\frac{\partial \rho}{\partial z} = -\rho\left(\frac{\partial v_x}{\partial x} + \frac{\partial v_y}{\partial y} + \frac{\partial v_z}{\partial z}\right) \quad \text{..... (A-3)}$$

The left side of Equation A-3 is the substantial derivative of density. Hence, it may be abbreviated thus:

$$\frac{D\rho}{Dt} = -\rho(\nabla \cdot v) \quad \text{..... (A-4)}$$

APPENDIX B: DERIVATION OF MOMENTUM EQUATION

The momentum balance for a volume element of $\Delta x \Delta y \Delta z$ can be written as follows:

Rate of Momentum Accumulation	=	Rate of Momentum in	-	Rate of Momentum out	+	Sum of forces acting on the system

The rates of the flow the x component of momentum into and out of the volume element is considered first. Momentum flows into and out of the volume element by two mechanics: by convection (bulk fluid flow) and by molecular transfer (velocity gradients).

The rate at which the x component of momentum enters the face at x by convection is $\rho v_x v_x|_x \Delta y \Delta z$ and the rate at which it leaves at $x+\Delta x$ is $\rho v_x v_x|_{x+\Delta x} \Delta y \Delta z$. If similar expressions are written for the other faces of the volume, we get the net convective momentum flow into the volume element as:

$$\Delta y \Delta z \left[\rho v_x v_x \big|_x - \rho v_x v_x \big|_{x+\Delta x} \right] + \Delta x \Delta z \left[\rho v_y v_x \big|_y - \rho v_y v_x \big|_{y+\Delta y} \right] + \Delta x \Delta y \left[\rho v_z v_x \big|_z - \rho v_z v_x \big|_{z+\Delta z} \right] \quad \text{(B-1)}$$

Likewise, the rate at which x component of momentum enters the face at x by molecular transport is $\tau_{xx}|_x \Delta y \Delta z$ and the rate at which it leaves at $x+\Delta x$ is $\tau_{xx}|_{x+\Delta x} \Delta y \Delta z$. When contributions from six faces are summed up, we get:

$$\Delta y \Delta z \left[\tau_{xx} \big|_x - \tau_{xx} \big|_{x+\Delta x} \right] + \Delta x \Delta z \left[\tau_{yx} \big|_y - \tau_{yx} \big|_{y+\Delta y} \right] + \Delta x \Delta y \left[\tau_{zx} \big|_z - \tau_{yz} \big|_{z+\Delta z} \right] \quad \text{(B-2)}$$

The important forces occur in many cases from fluid pressure p and the gravitational force per unit mass g. The result of these of forces in the x direction can be written as:

$$\Delta y \Delta z \left(P \big|_x - P \big|_{x+\Delta x} \right) + \rho g_x \Delta x \Delta y \Delta z \quad \text{(B-3)}$$

The rate of accumulation of x momentum within the element is:

$$\Delta x\Delta y\Delta z\left(\partial\rho v_x/\partial t\right) \quad \text{.....(B-4)}$$

We can achieve the total convective flow of x-momentum across 6 faces by substituting the Equations B-1, B-2, B-3 and B-4 into momentum balance equation.

$$\begin{aligned}\Delta x\Delta y\Delta z\left(\frac{\partial\rho v_x}{\partial t}\right) = &\left[\Delta y\Delta z\left[\rho v_x v_x\big|_x - \rho v_x v_x\big|_{x+\Delta x}\right] + \Delta x\Delta z\left[\rho v_y v_x\big|_y - \rho v_y v_x\big|_{y+\Delta y}\right] + \Delta x\Delta y\left[\rho v_z v_x\big|_z - \rho v_z v_x\big|_{z+\Delta z}\right]\right] + \\ &\left[\Delta y\Delta z\left[\tau_{xx}\big|_x - \tau_{xx}\big|_{x+\Delta x}\right] + \Delta x\Delta z\left[\tau_{yx}\big|_y - \tau_{yx}\big|_{y+\Delta y}\right] + \Delta x\Delta y\left[\tau_{zx}\big|_z - \tau_{yz}\big|_{z+\Delta z}\right]\right] + \\ &\left[\Delta y\Delta z\left(P\big|_x - P\big|_{x+\Delta x}\right) + \rho g_x\Delta x\Delta y\Delta z\right]\end{aligned}$$

.....(B-5)

By dividing the Equation B-5 by ΔxΔyΔz:

$$\begin{aligned}\frac{\left(\partial\rho v_x\right)}{\partial t} &= \frac{\partial\rho v_x v_x}{\Delta x}\bigg|_x - \frac{\partial\rho v_x v_x}{\Delta x}\bigg|_{x+\Delta x} + \frac{\partial\rho v_y v_x}{\Delta y}\bigg|_y - \frac{\partial\rho v_y v_x}{\Delta y}\bigg|_{y+\Delta y} + \frac{\partial\rho v_z v_x}{\Delta z}\bigg|_z - \frac{\partial\rho v_z v_x}{\Delta z}\bigg|_{z+\Delta z} - \\ &= \frac{\tau_{xx}}{\Delta x}\bigg|_x - \frac{\tau_{xx}}{\Delta x}\bigg|_{x+\Delta x} + \frac{\tau_{yx}}{\Delta y}\bigg|_y - \frac{\tau_{yx}}{\Delta y}\bigg|_{y+\Delta y} + \frac{\tau_{zx}}{\Delta z}\bigg|_z - \frac{\tau_{zx}}{\Delta z}\bigg|_{z+\Delta z} + \frac{\left(P\big|_x - P\big|_{x+\Delta x}\right)}{\Delta x} + \rho g_x \\ &= -\left(\frac{\partial}{\partial x}\rho v_x v_x + \frac{\partial}{\partial y}\rho v_y v_x + \frac{\partial}{\partial z}\rho v_z v_x\right) - \left(\frac{\partial}{\partial x}\tau_{xx} + \frac{\partial}{\partial y}\tau_{yx} + \frac{\partial}{\partial z}\tau_{zx}\right) - \frac{\partial P}{\partial x} + \rho g_x\end{aligned}$$

.....(B-6)

By taking the limit as Δx,Δy and Δz approach zero, we obtain the x component of the equation of motion. The y and z components are obtained similarly. Since these equations take up so much space, they are combined to the Equation B-10. For the reader's convenience the x, y and z components of the equation of motion are shown as follows:

x – component:

$$\frac{(\partial \rho v_x)}{\partial t} = -\left(\frac{\partial}{\partial x} \rho v_x v_x + \frac{\partial}{\partial y} \rho v_y v_x + \frac{\partial}{\partial z} \rho v_z v_x \right) - \left(\frac{\partial}{\partial x} \tau_{xx} + \frac{\partial}{\partial y} \tau_{yx} + \frac{\partial}{\partial z} \tau_{zx} \right) - \frac{\partial P}{\partial x} + \rho g_x$$

.....(B-7)

y – component:

$$\frac{(\partial \rho v_y)}{\partial t} = -\left(\frac{\partial}{\partial x} \rho v_x v_y + \frac{\partial}{\partial y} \rho v_y v_y + \frac{\partial}{\partial z} \rho v_z v_y \right) - \left(\frac{\partial}{\partial x} \tau_{xy} + \frac{\partial}{\partial y} \tau_{yy} + \frac{\partial}{\partial z} \tau_{zy} \right) - \frac{\partial P}{\partial y} + \rho g_y$$

.....(B-8)

z – component:

$$\frac{(\partial \rho v_z)}{\partial t} = -\left(\frac{\partial}{\partial x} \rho v_x v_z + \frac{\partial}{\partial y} \rho v_y v_z + \frac{\partial}{\partial z} \rho v_z v_z \right) - \left(\frac{\partial}{\partial x} \tau_{xz} + \frac{\partial}{\partial y} \tau_{yz} + \frac{\partial}{\partial z} \tau_{zz} \right) - \frac{\partial P}{\partial z} + \rho g_z$$

..... (B-9)

$$\frac{\partial}{\partial t} \rho v = -[\nabla \cdot \rho v v] - \nabla p - \nabla \tau + \rho g$$ .....(B-10)

Equation B-11 is arranged with help of Equation A-2 (The Equation of Continuity) into:

$$\rho \frac{Dv_x}{Dt} = -\frac{\partial P}{\partial x} - \left(\frac{\partial \tau_{xx}}{\partial x} + \frac{\partial \tau_{yx}}{\partial y} + \frac{\partial \tau_{zx}}{\partial z} \right) + \rho g_x$$ .....(B-11)

Or more generally:

$$\rho \frac{Dv}{Dt} = -\nabla p - [\nabla \cdot \tau] + \rho g$$ .....(B-12)

This is a statement of Newton's second law in the form of mass times acceleration is equal to the sum of forces. It should be noted that the momentum balance is completely equivalent to Newton's second law of motion. In order to use these equations to determine the velocity distributions, we must insert expressions for the various stresses in terms of velocity gradients and fluid properties. For the Newtonian fluids, these expressions are as follows:

$$\tau_{xx} = -2\mu \frac{dv_x}{dx} + \frac{2}{3}\mu(\nabla \cdot v) \quad \text{.....(B-13)}$$

$$\tau_{yy} = -2\mu \frac{dv_y}{dy} + \frac{2}{3}\mu(\nabla \cdot v) \quad \text{.....(B-14)}$$

$$\tau_{zz} = -2\mu \frac{dv_z}{dz} + \frac{2}{3}\mu(\nabla \cdot v) \quad \text{.....(B-15)}$$

$$\tau_{xy} = \tau_{yx} = -\mu\left(\frac{dv_x}{dy} + \frac{dv_y}{dx}\right) \quad \text{.....(B-16)}$$

$$\tau_{yz} = \tau_{zy} = -\mu\left(\frac{dv_y}{dz} + \frac{dv_z}{dy}\right) \quad \text{.....(B-17)}$$

$$\tau_{zx} = \tau_{xz} = -\mu\left(\frac{dv_z}{dx} + \frac{dv_x}{dz}\right) \quad \text{.....(B-18)}$$

For constant ρ and constant μ, the velocity and fluid gradient incorporated form of Equation B-12 may be simplified by means of the equation of continuity $\left[\nabla \cdot v = 0\right]$ into:

$$\rho \frac{Dv}{Dt} = -\nabla P + \mu \nabla^2 v + \rho g \quad \text{.....(B-19)}$$

APPENDIX C: DERIVATION OF REYNOLDS EQUATION

Assumptions 1 to 7 stated in Section 3.1.2 will lead the Equations B-7, B-8 and B-9 in Appendix B to:

$$\frac{1}{\mu}\frac{\partial p}{\partial x} = \frac{\partial^2 v_x}{\partial z^2} \quad \text{.....(C-1)}$$

$$\frac{1}{\mu}\frac{\partial p}{\partial y} = \frac{\partial^2 v_y}{\partial z^2} \quad \text{.....(C-2)}$$

By integrating Equations C-1 and C-2 twice with the boundary conditions:
$v_x = 0$ and $v_y=0$ at z=0 and z=w
we have:

$$v_x = \frac{1}{2\mu}\frac{\partial p}{\partial x} z\left(z - w\right) \quad \text{.....(C-3)}$$

$$v_y = \frac{1}{2\mu}\frac{\partial p}{\partial y} z\left(z - w\right) \quad \text{.....(C-4)}$$

Equations C-3 and C-4 give the velocity profile in the fluid film as affected by the viscosity, fluid height and the pressure gradients. The Continuity equation can now be rewritten by substituting the equations C-3 and C-4.

$$\frac{\partial\left(v_z \rho\right)}{\partial z} = -\frac{1}{2}\left\{\left[\frac{\partial}{\partial x}\left(\frac{\rho}{\mu}\frac{\partial p}{\partial x} z\left(z - w\right)\right)\right] + \left[\frac{\partial}{\partial y}\left(\frac{\rho}{\mu}\frac{\partial p}{\partial y} z\left(z - w\right)\right)\right]\right\} \quad \text{.....(C-5)}$$

By integrating with respect to y with the conditions v = V at z = 0 and v = 0 at z = h, we have:

$$\frac{\partial}{\partial x}\left(\frac{\rho w^3}{\mu}\frac{\partial p}{\partial x}\right)+\frac{\partial}{\partial y}\left(\frac{\rho w^3}{\mu}\frac{\partial p}{\partial y}\right)=12\rho V \quad \text{.....(C-6)}$$

If the density is assumed constant, Equation C-6 yields to:

$$\frac{\partial}{\partial x}\left(\frac{w^3}{\mu}\frac{\partial p}{\partial x}\right)+\frac{\partial}{\partial y}\left(\frac{w^3}{\mu}\frac{\partial p}{\partial y}\right)=12\frac{\partial w}{\partial t} \quad \text{.....(C-7)}$$

Equation C-7 is the Reynolds equation for an incompressible flow.

APPENDIX D: DERIVATION OF VELOCITY AND FLOW RATE DISTRIBUTION EQUATIONS FOR NEWTONIAN FLUIDS BETWEEN TWO PARALLEL PLATES

$$v_y = v_z = 0 \Rightarrow v_x = v(y,z,t))$$

From Navier Stokes equations for x and y directions can be figured out that ∂P/∂y and ∂P/∂z are equal to zero. The pressure depends only on x. In the Navier Stokes equation for x direction all convective terms disappear.

$$\frac{(\partial \rho v_x)}{\partial t} = -\cancel{\left(\frac{\partial}{\partial x}\rho v_x v_x + \frac{\partial}{\partial y}\rho v_y v_x + \frac{\partial}{\partial z}\rho v_z v_x\right)} - \left(\frac{\partial}{\partial x}\tau_{xx} + \frac{\partial}{\partial y}\tau_{yx} + \frac{\partial}{\partial z}\tau_{zx}\right) - \cancel{\frac{\partial P}{\partial x}} + \rho g \quad \text{..... (D-1)}$$

When the fluid flows in the x direction between two parallel plates perpendicular to z direction, then the stress equations give:

$$\tau_{xx} = \tau_{yy} = \tau_{zz} = \tau_{yz} = \tau_{xz} = 0 \quad \text{..... (D-2)}$$

$$\frac{(\partial \rho v_x)}{\partial t} = -\frac{\partial P}{\partial x} - \left(\frac{\partial}{\partial y}\tau_{yx}\right) \quad \text{..... (D-3)}$$

$$\rho \frac{\partial v_x}{\partial t} = -\frac{dP}{dx} + \left(\frac{\partial}{\partial y}\tau_{yx}\right) \quad \text{..... (D-4)}$$

General equation for Newtonian and non-Newtonian fluids is as follows:

$$\frac{\Delta P}{L} = \left(\frac{\partial}{\partial y}\tau_{yx}\right) \quad \text{..... (D-5)}$$

$$\tau_{yx} = -\mu \frac{\partial v_x}{\partial y} \quad \text{(D-6)}$$

$$\frac{\partial}{\partial y}\tau_{yx} = \frac{\Delta P}{L} \quad \text{(D-7)}$$

$$\tau_{yx} = \frac{\Delta P}{L} y \quad \text{(D-8)}$$

$$\tau_{yx} = -\mu \frac{\partial v_x}{\partial y} = \frac{\Delta P}{L} y \quad \text{(D-9)}$$

$$-\frac{\partial v_x}{\partial y} = \frac{\Delta P}{L}\frac{y}{\mu} \quad \text{(D-10)}$$

$$-dv_x = \frac{\Delta P}{L}\frac{y}{\mu} dy \quad \text{(D-11)}$$

$$-v_x = \frac{\Delta P}{L}\frac{y^2}{2\mu} + c_2 \quad \text{(D-12)}$$

$$v_x = -\frac{\Delta P}{L}\frac{y^2}{2\mu} - c_2 \quad \text{(D-13)}$$

If $v_x = 0$ at $y = \pm H/2$

$$c_2 = -\frac{\Delta P}{L}\frac{H^2}{8\mu} \quad \text{(D-14)}$$

$$v_x = \frac{\Delta P}{L}\frac{H^2}{8\mu} - \frac{\Delta P}{\Delta x}\frac{y^2}{2\mu}$$
$$= \frac{\Delta P}{L}\frac{1}{2\mu}\left(\left(\frac{H}{2}\right)^2 - y^2\right) \quad \text{(D-15)}$$

$$v_x = \frac{\Delta P}{L}\frac{1}{2\mu}\left(\left(\frac{H}{2}\right)^2 - y^2\right) \quad \text{(D-16)}$$

Equation D-16 shows the velocity distribution of a Newtonian fluid in laminar flow conditions between two parallel plates. The same procedure is followed for Power-Law, Bingham Plastic and Yield Power Law fluids and their velocity profiles between two parallel plates are derived and shown in Appendix E, respectively.

The velocity profile shown in Equation D-16 can be integrated across the fracture to find the overall flow rate:

$$Q_x = \int_0^w \int_{-H/2}^{H/2} v_x \, dy \, dz \quad \text{(D-17)}$$

$$Q_x = w \int_{-H/2}^{H/2} \frac{\Delta P}{L}\frac{1}{2\mu}\left(\left(\frac{H}{2}\right)^2 - y^2\right) dy \quad \text{(D-18)}$$

$$Q_x = w\frac{\Delta P}{L}\frac{1}{2\mu}\left(\left(\frac{H}{2}\right)^2 y - \frac{y^3}{3}\right)\Bigg|_{-H/2}^{H/2} \quad \text{(D-19)}$$

$$Q_x = w\frac{\Delta P}{L}\frac{1}{2\mu}\left(\frac{H^3}{8} - \frac{H^3}{24}\right) - w\frac{\Delta P}{L}\frac{1}{2\mu}\left(\frac{H^3}{24} - \frac{H^3}{8}\right) \quad \text{(D-20)}$$

$$Q_x = w\frac{\Delta P}{L}\frac{1}{2\mu}\left(\frac{H^3}{4} - \frac{H^3}{12}\right) = w\frac{\Delta P}{L}\frac{H^3}{12\mu} \quad \text{(D-21)}$$

APPENDIX E: DERIVATION OF VELOCITY AND FLOW RATE DISTRIBUTION EQUATIONS FOR NON-NEWTONIAN FLUIDS BETWEEN TWO PARALLEL PLATES

Derivation of Velocity Distribution Equation of Power Law Fluids:

$$\tau_{yx} = -m\left|\frac{\partial v_x}{\partial y}\right|^{n-1}\frac{\partial v_x}{\partial y} \quad \text{.....(E-1)}$$

$$\tau_{yx} = \frac{\Delta P}{L}y \quad \text{.....(E-2)}$$

$$\frac{\Delta P}{L}y = -m\left|\frac{\partial v_x}{\partial y}\right|^{n-1}\frac{\partial v_x}{\partial y} \quad \text{.....(E-3)}$$

$$-\frac{\partial v_x}{\partial y} = \left(\frac{\Delta P}{L}\frac{y}{m}\right)^{1/n} \quad \text{.....(E-4)}$$

$$v_x = -\left(\frac{\Delta P}{L\cdot m}\right)^{1/n}\left(\frac{1}{n}+1\right)^{-1}y^{\left(\frac{1}{n}+1\right)} - c_2 \quad \text{.....(E-5)}$$

If $v_x=0$ at $y= \pm H/2$

$$c_2 = -\left(\frac{\Delta P}{L\cdot m}\right)^{1/n}\left(\frac{1}{n}+1\right)^{-1}\left(\frac{H}{2}\right)^{\left(\frac{1}{n}+1\right)} \quad \text{.....(E-6)}$$

$$v_x = \left(\frac{\Delta P}{L\cdot m}\right)^{1/n}\left(\frac{1}{n}+1\right)^{-1}\left(\frac{H}{2}\right)^{\left(\frac{1}{n}+1\right)} - \left(\frac{\Delta P}{L\cdot m}\right)^{1/n}\left(\frac{1}{n}+1\right)^{-1}y^{\left(\frac{1}{n}+1\right)} \quad \text{.....(E-7)}$$

$$v_x = \left(\frac{\Delta P}{L\cdot m}\right)^{1/n}\left(\frac{n}{n+1}\right)\left[\left(\frac{H}{2}\right)^{(n+1)/n} - (y)^{(n+1)/n}\right] \quad \text{.....(E-8)}$$

Derivation of Velocity Distribution Equation of Bingham Plastic Fluids:

$$\tau_{yx} = \tau_y - \mu_p \frac{\partial v_x}{\partial y} \quad \text{.....(E-9)}$$

$$\tau_{yx} = \frac{\Delta P}{L} y \quad \text{.....(E-10)}$$

$$\frac{\Delta P}{L} y = \tau_y - \mu_p \frac{\partial v_x}{\partial y} \quad \text{.....(E-11)}$$

$$-\frac{\partial v_x}{\partial y} = \frac{\Delta P}{L} \frac{y}{\mu_p} - \frac{\tau_y}{\mu_p} \quad \text{.....(E-12)}$$

$$v_x = -\frac{\Delta P}{L} \frac{y^2}{2\mu} + \frac{\tau_y y}{\mu_p} - c_2 \quad \text{.....(E-13)}$$

If $v_x=0$ at $y= \pm H/2$

$$c_2 = \left(-\frac{\Delta P}{L} \frac{H^2}{8\mu} + \frac{\tau_Y H}{2\mu} \right) \quad \text{.....(E-14)}$$

$$v_x = -\frac{\Delta P}{L} \frac{y^2}{2\mu_P} + \frac{\tau_y y}{\mu_P} + \frac{\Delta P}{L} \frac{H^2}{8\mu_P} - \frac{\tau_y H}{2\mu_P} \quad \text{.....(E-15)}$$

$$v_x = \frac{1}{\mu_p} \left[\frac{\Delta P}{2L} \left(\left(\frac{H}{2} \right)^2 - y^2 \right) - \tau_y \left(\frac{H}{2} - y \right) \right] \quad \text{.....(E-16)}$$

or

$$\frac{\tau_w}{\tau_y} = \frac{H/2}{y_b} \quad \text{.....(E-17)}$$

$$\tau_w = \frac{H}{2} \frac{\Delta P}{L} \quad \text{.....(E-18)}$$

$$\tau_y = \frac{\Delta P}{L} y_b \quad \text{(E-20)}$$

$$v_x = \left[\frac{\Delta P}{2L} \frac{1}{\mu_p} \left(\left(\frac{H}{2} \right)^2 - y^2 \right) - \frac{\Delta P}{2L} \frac{y_b}{\mu_p} (H - 2y) \right] \quad \text{(E-21)}$$

$$v_x = \frac{\Delta P}{2L} \frac{1}{\mu_p} \left(\frac{H^2}{4} - y^2 + 2y_b y - H y_b \right) \quad \text{(E-22)}$$

v_{xplug} is obtained by substituting $y=y_b$

$$v_{xp} = \frac{\Delta P}{2L} \frac{1}{\mu_p} \left(\frac{H^2}{4} - y_b^2 + 2y_b^2 - H y_b \right) \quad \text{(E-23)}$$

$$v_{xp} = \frac{\Delta P}{2L} \frac{1}{\mu_p} \left(\frac{H^2}{4} - H y_b + y_b^2 \right) \quad \text{(E-24)}$$

Derivation of Velocity Distribution Equation of Yield Power Law Fluids:

$$\tau_{yx} = \tau_y - K\left(\frac{\partial v_x}{\partial y}\right)^n \quad \text{.....(E-25)}$$

$$\tau_{yx} = \frac{\Delta P}{L} y \quad \text{.....(E-26)}$$

$$\frac{\Delta P}{L} y = \tau_Y - K\left(\frac{\partial v_x}{\partial y}\right)^n \quad \text{.....(E-27)}$$

$$-\frac{\partial v_x}{\partial y} = \left(\frac{\Delta P}{L}\frac{y}{K} - \frac{\tau_y}{K}\right)^{1/n} \quad \text{.....(E-28)}$$

$$-dv_x = \left(\frac{\Delta P}{L}\frac{y}{K} - \frac{\tau_y}{K}\right)^{1/n} dy \quad \text{.....(E-29)}$$

$$-v_x = \int\left(\frac{\Delta P}{L}\frac{y}{K} - \frac{\tau_y}{K}\right)^{1/n} \quad \text{.....(E-30)}$$

$$\int (a+by)^n dy = \frac{1}{b}\int \mathrm{X}^n dy = \frac{\mathrm{X}^{n+1}}{b(n+1)} \qquad \text{if X = a + by} \quad \text{.....(E-31)}$$

$$a = -\frac{\tau_y}{K} \quad b = \frac{\Delta P}{L}\frac{1}{K} \quad \text{.....(E-32)}$$

$$-v_x = \frac{K}{\frac{\Delta P}{L}}\int\left(-\frac{\tau_y}{K} + \frac{\Delta P}{L}\frac{y}{K}\right)^{1/n} dy \quad \text{.....(E-33)}$$

$$v_x = -\frac{\left(-\frac{\tau_y}{K} + \frac{\Delta P}{L}\frac{y}{K}\right)^{\frac{1}{n}+1}}{\left(\frac{\Delta P}{LK}\right)\left(1+\frac{1}{n}\right)} - c_2 \quad \text{.....(E-34)}$$

If $v_x=0$ at $y= \pm H/2$

$$c_2 = -\frac{\left(-\frac{\tau_y}{K}+\frac{\Delta P}{L}\frac{H}{2K}\right)^{\frac{n+1}{n}}}{\frac{\Delta P}{LK}\left(\frac{n+1}{n}\right)} \quad \text{.....(E-35)}$$

$$v_x = -\frac{\left(-\frac{\tau_y}{K}+\frac{\Delta P}{L}\frac{H}{2K}\right)^{\frac{n+1}{n}}-\left(-\frac{\tau_y}{K}+\frac{\Delta P}{L}\frac{y}{K}\right)^{\frac{n+1}{n}}}{\left(\frac{\Delta P}{LK}\right)\left(1+\frac{1}{n}\right)} \quad \text{.....(E-36)}$$

$$v_x = -\frac{\left(-\frac{\tau_y}{K}+\frac{\tau_w}{K}\right)^{\frac{n+1}{n}}-\left(-\frac{\tau_y}{K}+\frac{\Delta P}{L}\frac{y}{K}\right)^{\frac{n+1}{n}}}{\left(\frac{\Delta P}{LK}\right)\left(1+\frac{1}{n}\right)} \quad \text{.....(E-37)}$$

$$v_x = -\frac{\left[\left(\frac{1}{K}\right)^{\frac{n+1}{n}}\left(\left(\tau_w-\tau_y\right)^{\frac{n+1}{n}}-\left(\frac{\Delta P}{L}\frac{y}{1}-\tau_y\right)^{\frac{n+1}{n}}\right)\right]}{\left(\frac{\Delta P}{LK}\right)\left(1+\frac{1}{n}\right)} \quad \text{.....(E-38)}$$

$$v_x = \left[\left(\frac{L}{\Delta P}\right)\left(\frac{n}{n+1}\right)\left(\frac{1}{K}\right)^{\frac{1}{n}}\left(\left(\frac{\Delta P}{L}\frac{y}{1}-\tau_y\right)^{\frac{n+1}{n}}-\left(\tau_w-\tau_y\right)^{\frac{n+1}{n}}\right)\right] \quad \text{.....(E-39)}$$

For $0 \le y \le y_b$ $y = y_b$

$$v_{xp} = \left[\left(\frac{L}{\Delta P}\right)\left(\frac{n}{n+1}\right)\left(\frac{1}{K}\right)^{\frac{1}{n}}\left(\cancel{\left(\frac{\Delta P}{L}\frac{y}{1}-\tau_y\right)^{\frac{n+1}{n}}}-\left(\tau_w-\tau_y\right)^{\frac{n+1}{n}}\right)\right] \quad \text{.....(E-40)}$$

$$v_{xp} = \left[\left(\frac{L}{\Delta P}\right)\left(\frac{n}{n+1}\right)\left(\frac{1}{K}\right)^{\frac{1}{n}}\left(-\left(\tau_w-\frac{\Delta P}{L}y_b\right)^{\frac{n+1}{n}}\right)\right] \quad \text{.....(E-41)}$$

Derivation of Flow Rate Distribution Equation of Power Law Fluids:

$$v_x = \left(\frac{\Delta P}{L \cdot m}\right)^{1/n} \left(\frac{n}{n+1}\right)\left[\left(\frac{H}{2}\right)^{(n+1)/n} - (y)^{(n+1)/n}\right] \quad \text{.....(E-41)}$$

$$Q_x = \int_0^w \int_{-H/2}^{H/2} v_x \, dy \, dz \quad \text{.....(E-42)}$$

$$Q_x = w \int_{-H/2}^{H/2} \left(\frac{\Delta P}{L \cdot m}\right)^{1/n} \left(\frac{n}{n+1}\right)\left[\left(\frac{H}{2}\right)^{(n+1)/n} - (y)^{(n+1)/n}\right] dy \quad \text{.....(E-43)}$$

$$Q_x = w\left(\frac{\Delta P}{L \cdot m}\right)^{1/n} \left(\frac{n}{n+1}\right)\left[\left(\frac{H}{2}\right)^{(n+1)/n} y - \left(\frac{n}{2n+1}\right)(y)^{(2n+1)/n}\right]_{-H/2}^{H/2} \quad \text{.....(E-44)}$$

$$Q_x = w\left(\frac{\Delta P}{L \cdot m}\right)^{1/n} \left(\frac{n}{n+1}\right)\left(\frac{H}{2}\right)^{(2n+1)/n} \left[1 - \frac{n}{2n+1} + 1 - \frac{n}{2n+1}\right] \quad \text{.....(E-45)}$$

$$Q_x = w\left(\frac{\Delta P}{L \cdot m}\right)^{1/n} \left(\frac{n}{n+1}\right)\left(\frac{H}{2}\right)^{(2n+1)/n} \left[\frac{2n+2}{2n+1}\right] \quad \text{.....(E-46)}$$

$$Q_x = w\left(\frac{\Delta P}{L \cdot m}\right)^{1/n} \left(\frac{n}{1}\right)\left(\frac{H}{2}\right)^{2} \left(\frac{H}{2}\right)^{1/n} \left[\frac{2}{2n+1}\right] \quad \text{.....(E-47)}$$

$$Q_x = \left[\frac{2n}{2n+1}\right]\left(\frac{H}{2}\right)^{\frac{2n+1}{n}} \left(\frac{\Delta P}{L}\right)^{1/n} \left(\frac{1}{m}\right)^{1/n} w \quad \text{.....(E-48)}$$

$$Q_x = \left[\frac{2n}{2n+1}\right]\left(\frac{1}{2}\right)^{\frac{2n+1}{n}} (H)^{\frac{2n+1}{n}} \left(\frac{\Delta P}{L}\right)^{1/n} \left(\frac{1}{m}\right)^{1/n} w \quad \text{.....(E-49)}$$

$$Q_x = \left[\frac{n}{2n+1}\right]\left(\frac{1}{2}\right)^{\frac{n+1}{n}} (H)^{\frac{2n+1}{n}} \left(\frac{\Delta P}{L}\right)^{1/n} \left(\frac{1}{m}\right)^{1/n} w \quad \text{.....(E-50)}$$

Derivation of Flow Rate Distribution Equation of Bingham Plastic Fluids:

$$v_{xp} = \frac{\Delta P}{2L}\frac{1}{\mu_p}\left(\frac{H^2}{4} - Hy_b + y_b^2\right) \quad \text{.....(E-51)}$$

$$v_x = \frac{\Delta P}{2L}\frac{1}{\mu_p}\left(\frac{H^2}{4} - y^2 + 2y_b y - Hy_b\right) \quad \text{.....(E-52)}$$

$$\sum Q = 2\left(Q_X + Q_{XP}\right) = 2w\left(\int_{y_b}^{H/2} v_x dy + v_{xp}\int_0^{y_b} dy\right) \quad \text{.....(E-53)}$$

Second Integral => $Q_{XP} = v_{xp}y_b = \frac{\Delta P}{2L}\frac{1}{\mu_p}\left(\frac{H^2}{4}y_b - Hy_b^2 + y_b^3\right)$ .....(E-54)

First Integral => $Q_X = \frac{\Delta P}{2L}\frac{1}{\mu_p}\left(\frac{H^2}{4}y - \frac{y^3}{3} + y_b y^2 - yHy_b\right)_{y_b}^{H/2}$ .....(E-55)

$$Q_X = \frac{\Delta P}{2L}\frac{1}{\mu_p}\left(\frac{H^3}{12} - \frac{H^2}{2}y_b - \frac{2}{3}y_b^3 + Hy_b^2\right) \quad \text{.....(E-56)}$$

$$\sum Q = 2\left(Q_X + Q_{XP}\right) = 2w\frac{\Delta P}{2L}\frac{1}{\mu_p}\left(\frac{H^3}{12} - \frac{H^2}{2}y_b - \frac{2}{3}y_b^3 + Hy_b^2 + \frac{H^2}{4}y_b - Hy_b^2 + y_b^3\right) \quad \text{....(E-57)}$$

$$\sum Q = 2\left(Q_X + Q_{XP}\right) = w\frac{\Delta P}{L}\frac{1}{\mu_p}\left(\frac{H^3}{12} - \frac{H^2}{4}y_b + \frac{1}{3}y_b^3\right) \quad \text{.....(E-58)}$$

$$\sum Q = 2\left(Q_X + Q_{XP}\right) = \frac{w\Delta P}{L}\frac{H^3}{\mu_p}\left(\frac{1}{12} - \frac{y_b}{4H} + \frac{1}{3}\frac{y_b^3}{H^3}\right) \quad \text{.....(E-59)}$$

$$\sum Q = 2\left(Q_X + Q_{XP}\right) = \frac{w\Delta P}{L}\frac{H^3}{\mu_p}\left(\frac{1}{12} - \frac{y_b}{8\frac{H}{2}} + \frac{1}{3}\frac{1}{8}\frac{y_b^3}{\frac{H^3}{8}}\right) \quad \text{(E-60)}$$

$$\frac{\tau_y}{\tau_w} = \frac{y_b}{H/2} = \phi \quad \text{(E-61)}$$

$$\sum Q = 2\left(Q_X + Q_{XP}\right) = \frac{w\Delta P}{L}\frac{H^3}{\mu_p}\left(\frac{1}{12} - \frac{\phi}{8} + \frac{\phi^3}{24}\right) \quad \text{(E-62)}$$

$$\sum Q = 2\left(Q_X + Q_{XP}\right) = \frac{w\Delta P}{L}\frac{H^3}{\mu_p 12}\left(1 - \frac{3\phi}{2} + \frac{\phi^3}{2}\right) \quad \text{(E-63)}$$

or

$$\sum Q = \frac{w\tau_w H^2}{\mu_p 6}\left(1 - \frac{3\phi}{2} + \frac{\phi^3}{2}\right) \quad \text{(E-64)}$$

Derivation of Flow Rate Distribution Equation of Yield Power Law Fluids (Herschel Bulkley Fluids):

$$v_x = \left[\left(\frac{L}{\Delta P}\right)\left(\frac{n}{n+1}\right)\left(\frac{1}{K}\right)^{\frac{1}{n}}\left(\left(\frac{\Delta P}{L}\frac{y}{1}-\tau_y\right)^{\frac{n+1}{n}}-\left(\tau_w-\tau_y\right)^{\frac{n+1}{n}}\right)\right] \quad \text{.....(E-65)}$$

$$v_{xp} = \left[\left(\frac{L}{\Delta P}\right)\left(\frac{n}{n+1}\right)\left(\frac{1}{K}\right)^{\frac{1}{n}}\left(-\left(\tau_w-\frac{\Delta P}{L}y_b\right)^{\frac{n+1}{n}}\right)\right] \quad \text{.....(E-66)}$$

$$\sum Q = 2\left(Q_X + Q_{XP}\right) = 2w\left(\int_{y_b}^{H/2} v_x dy + v_{xp}\int_0^{y_b} dy\right) \quad \text{.....(E-67)}$$

Integrating by parts gives:

$$\sum Q = 2w\int_0^{H/2} v_x dy = 2w\left[vy\Big|_0^{H/2} - \int_0^{H/2} y\frac{dv}{dy}dy\right] = 0 - 2w\int_0^{H/2} y\frac{dv}{dy}dy \quad \text{.....(E-68)}$$

$$\frac{dv_x}{dy} = \left[\left(\frac{L}{\Delta P}\right)\left(\frac{n}{n+1}\right)\left(\frac{1}{K}\right)^{\frac{1}{n}}\left(\left(\frac{\Delta P}{L}\frac{y}{1}-\tau_y\right)^{\frac{1}{n}}\right)\left(\frac{n+1}{n}\right)\left(\frac{\Delta P}{L}\right)\right] \quad \text{.....(E-69)}$$

$$y\frac{dv_x}{dy} = y\left[\left(\frac{1}{K}\right)^{\frac{1}{n}}\left(\left(\frac{\Delta P}{L}\frac{y}{1}-\tau_y\right)^{\frac{1}{n}}\right)\right] \quad \text{.....(E-70)}$$

$$\sum Q = 0 - 2w\int_0^{H/2} y\frac{dv}{dy}dy = -2w\int_0^{H/2} y\left[\left(\frac{1}{K}\right)^{\frac{1}{n}}\left(\left(\frac{\Delta P}{L}\frac{y}{1}-\tau_y\right)^{\frac{1}{n}}\right)\right]dy \quad \text{.....(E-71)}$$

$$\int_a^b f_x g_x' dx = f_x g_x\Big|_0^{H/2} - \int_0^{H/2} f_x' g_x dx \quad \text{.....(E-72)}$$

$$f_x = y$$

$$g_x^{/} = \left[\left(\frac{1}{K}\right)^{\frac{1}{n}}\left(\left(\frac{\Delta P}{L}\frac{y}{1}-\tau_y\right)^{\frac{1}{n}}\right)\right] \quad \text{.....(E-73)}$$

$$\sum Q = -2w\left[y\int_0^{H/2}\left[\left(\frac{1}{K}\right)^{\frac{1}{n}}\left(\left(\frac{\Delta P}{L}\frac{y}{1}-\tau_y\right)^{\frac{1}{n}}\right)\right]dy - \int_0^{H/2}1\int_0^{H/2}\left[\left(\frac{1}{K}\right)^{\frac{1}{n}}\left(\left(\frac{\Delta P}{L}\frac{y}{1}-\tau_y\right)^{\frac{1}{n}}\right)\right]dy\right] \text{.....(E-74)}$$

$$\sum Q = -2w\left[y\left(\frac{1}{K}\right)^{\frac{1}{n}}\left(\left(\frac{\Delta P}{L}\frac{y}{1}-\tau_y\right)^{\frac{1}{n}+1}\left(\frac{n}{n+1}\right)\left(\frac{L}{\Delta P}\right)\right)\right|_0^{H/2} - \int_0^{H/2}1\left(\frac{1}{K}\right)^{\frac{1}{n}}\left(\left(\frac{\Delta P}{L}\frac{y}{1}-\tau_y\right)^{\frac{1}{n}+1}\left(\frac{n}{n+1}\right)\left(\frac{L}{\Delta P}\right)\right)dy\Bigg] \text{..}$$

.....(E-75)

$$\sum Q = -2w\left[\frac{H}{2}\left(\frac{1}{K}\right)^{\frac{1}{n}}\left(\left(\frac{\Delta P}{L}\frac{H}{2}-\tau_y\right)^{\frac{1}{n}+1}\left(\frac{n}{n+1}\right)\left(\frac{L}{\Delta P}\right)\right) - \left(\frac{1}{K}\right)^{\frac{1}{n}}\left(\left(\frac{\Delta P}{L}\frac{y}{1}-\tau_y\right)^{\frac{1}{n}+2}\left(\frac{n}{n+1}\right)\left(\frac{n}{2n+1}\right)\left(\frac{L}{\Delta P}\right)^2\right)\right|_0^{H/2}\Bigg] \text{...}$$

.....(E-76)

$$\frac{\sum Q}{wH^2} = \left[2\left(\frac{1}{K}\right)^{\frac{1}{n}}\left(\left(\tau_W-\tau_y\right)^{\frac{1}{n}+2}\left(\frac{n}{n+1}\right)\left(\frac{n}{2n+1}\right)\left(\frac{1}{2\tau_W}\right)^2\right) - \left(\frac{1}{K}\right)^{\frac{1}{n}}\left(\left(\tau_W-\tau_y\right)^{\frac{1}{n}+1}\left(\frac{n}{n+1}\right)\left(\frac{1}{2\tau_W}\right)\right)\right] \text{..}$$

.....(E-77)

$$\frac{\sum Q}{wH^2} = \left(\frac{n}{n+1}\right)\left(\frac{1}{K}\right)^{\frac{1}{n}}\left(\tau_W-\tau_y\right)^{\frac{1}{n}+1}\left(\frac{1}{2\tau_W}\right)\left[\left(\left(\frac{\tau_W-\tau_y}{\tau_W}\right)\left(\frac{n}{2n+1}\right)\right)-1\right] \quad \text{.....(E-78)}$$

APPENDIX F: DISCRETIZATION OF REYNOLDS EQUATION

The explicit finite difference scheme for Newtonian fluids under exponential deformation law assumption is constructed as follows:

$$P_{k,l}^{j+1} = P_{k,l}^{j} + \left(\begin{array}{l} \left((\Delta t)\left({}^{1}\!/\!_{(12\cdot\mu)} \right) \left(\left({}^{1}\!/\!_{\left(w_0(k,l)(\beta/3)\exp\left(\beta\left(P_{k,l}^{j}-\sigma_n\right)/3\right)\right)} \right) \right) \right) \cdot \\ \left(\left(\frac{\partial}{\partial x}\left(\left(\left(w_0(k,l)\exp\left(-\beta\left(\sigma_n - P\right)/3\right)\right)^3 \cdot \left(\left(\frac{\partial P}{\partial x} \right) \right) \right) \right) + \right. \\ \left. \left(\frac{\partial}{\partial y}\left(\left(\left(w_0(k,l)\exp\left(-\beta\left(\sigma_n - P\right)/3\right)\right)^3 \cdot \left(\left(\frac{\partial P}{\partial y} \right) \right) \right) \right) \right) \end{array} \right) \quad \ldots (F\text{-}1)$$

$$P_{k,l}^{j+1} = P_{k,l}^{j} + \left(\begin{array}{l} \left((\Delta t)\left({}^{1}\!/\!_{(12\cdot\mu)} \right) \left(\left({}^{1}\!/\!_{\left(w_0(k,l)(\beta/3)\exp\left(\beta\left(P_{k,l}^{j}-\sigma_n\right)/3\right)\right)} \right) \right) \right) \cdot \\ \left(\begin{array}{l} \left(\begin{array}{l} \left(\left(w_0 \exp\left((\beta)\left(\left(\left(P_{k+1,l}^{j} + P_{k,l}^{j} \right)/2 \right) - \sigma_n \right)/3 \right) \right)^3 \right) - \\ \left(\left(\left(\left(P_{k+1,l}^{j} - P_{k,l}^{j} \right)/\Delta x \right) \right) \right)/(\Delta x) \end{array} \right) + \\ \left(\begin{array}{l} \left(\left(w_0(k,l)\exp\left((\beta)\left(\left(\left(P_{k,l}^{j} + P_{k-1,l}^{j} \right)/2 \right) - \sigma_n \right)/3 \right) \right)^{(3)} \right) \\ \left(\left(\left(\left(P_{k,l}^{j} - P_{k-1,l}^{j} \right)/\Delta x \right) \right) \right)/(\Delta x) \end{array} \right) + \\ \left(\begin{array}{l} \left(\left(w_0(k,l)\exp\left((\beta)\left(\left(\left(P_{k,l+1}^{j} + P_{k,l}^{j} \right)/2 \right) - \sigma_n \right)/3 \right) \right)^{(3)} \right) - \\ \left(\left(\left(\left(P_{k,l+1}^{j} - P_{k,l}^{j} \right)/\Delta y \right) \right) \right)/(\Delta y) \end{array} \right) \\ \left(\begin{array}{l} \left(\left(w_0(k,l)\exp\left((\beta)\left(\left(\left(P_{k,l}^{j} + P_{k,l-1}^{j} \right)/2 \right) - \sigma_n \right)/3 \right) \right)^{(3)} \right) \\ \left(\left(\left(\left(P_{k,l}^{j} - P_{k,l-1}^{j} \right)/\Delta y \right) \right) \right)/(\Delta y) \end{array} \right) \end{array} \right) \quad \ldots (F\text{-}2)$$

The explicit finite difference scheme for Power Law fluids under exponential deformation law assumption is constructed as follows:

$$P_{k,l}^{j+1} = P_{k,l}^{j} + \left(\begin{array}{l} \left((\Delta t)\left(1/K\right)^{\frac{1}{n}} \left(n/(2n+1) \right) \left(1/2\right)^{\frac{n+1}{n}} \left(\left(1/\left(w_0(k,l)(\beta/3)\exp\left(\beta\left(P_{k,l}^{j}-\sigma_n\right)/3\right)\right)\right)\right)\right) \cdot \\ \left(\frac{\partial}{\partial x}\left(\left(\left(w_0(k,l)\exp\left(-\beta\left(\sigma_n - P\right)/3\right)\right)\right)^3 \cdot \left(\left(\frac{\partial P}{\partial x}\right)\right)\right)\right) + \\ \left(\frac{\partial}{\partial y}\left(\left(\left(w_0(k,l)\exp\left(-\beta\left(\sigma_n - P\right)/3\right)\right)\right)^3 \cdot \left(\left(\frac{\partial P}{\partial y}\right)\right)\right)\right) \end{array} \right) \ldots$$

.....(F-3)

$$P_{k,l}^{j+1}=P_{k,l}^{j}+\left(\begin{array}{l}
\left(\begin{array}{l}
\left((\Delta t)\left(1/K\right)^{\frac{1}{n}}\left(n/(2n+1)\right)\left(1/2\right)^{\frac{n+1}{n}}\right)\cdot\\
\left(\left(1/\left(w_0(k,l)(\beta/3)\exp\left(\beta\left(P_{k,l}^{j}-\sigma_n\right)/3\right)\right)\right)\right)
\end{array}\right)\cdot\\
\left(\begin{array}{l}
\left(\begin{array}{l}
\left(\begin{array}{l}
\left(\left(w_0\exp\left((\beta)\left(\left(\left(P_{k+1,l}^{j}+P_{k,l}^{j}\right)/2\right)-\sigma_n\right)/3\right)\right)^{\left((2n+1)/n\right)}\right)\\
\left(\left(\left(\left(P_{k+1,l}^{j}-P_{k,l}^{j}\right)/\Delta x\right)\left(\left(abs\left(P_{k+1,l}^{j}-P_{k,l}^{j}\right)\right)/\Delta x\right)^{\left(1-n/n\right)}\right)\right)/(\Delta x)
\end{array}\right)-\\
\left(\begin{array}{l}
\left(\left(w_0(k,l)\exp\left((\beta)\left(\left(\left(P_{k,l}^{j}+P_{k-1,l}^{j}\right)/2\right)-\sigma_n\right)/3\right)\right)^{\left((2n+1)/n\right)}\right)\\
\left(\left(\left(\left(P_{k,l}^{j}-P_{k-1,l}^{j}\right)/\Delta x\right)\left(\left(abs\left(P_{k,l}^{j}-P_{k-1,l}^{j}\right)\right)/\Delta x\right)^{\left(1-n/n\right)}\right)\right)/(\Delta x)
\end{array}\right)
\end{array}\right)+\\
\left(\begin{array}{l}
\left(\begin{array}{l}
\left(\left(w_0(k,l)\exp\left((\beta)\left(\left(\left(P_{k,l+1}^{j}+P_{k,l}^{j}\right)/2\right)-\sigma_n\right)/3\right)\right)^{\left((2n+1)/n\right)}\right)\\
\left(\left(\left(\left(P_{k,l+1}^{j}-P_{k,l}^{j}\right)/\Delta y\right)\left(\left(abs\left(P_{k,l+1}^{j}-P_{k,l}^{j}\right)\right)/\Delta y\right)^{\left(1-n/n\right)}\right)\right)/(\Delta y)
\end{array}\right)-\\
\left(\begin{array}{l}
\left(\left(w_0(k,l)\exp\left((\beta)\left(\left(\left(P_{k,l}^{j}+P_{k,l-1}^{j}\right)/2\right)-\sigma_n\right)/3\right)\right)^{\left((2n+1)/n\right)}\right)\\
\left(\left(\left(\left(P_{k,l}^{j}-P_{k,l-1}^{j}\right)/\Delta y\right)\left(\left(abs\left(P_{k,l}^{j}-P_{k,l-1}^{j}\right)\right)/\Delta y\right)^{\left(1-n/n\right)}\right)\right)/(\Delta y)
\end{array}\right)
\end{array}\right)
\end{array}\right)
\end{array}\right)$$

....(F-4)